DEFORMATION AND FAILURE ANALYSIS OF LAMINATED COMPOSITES BY ISOGEOMETRIC ELEMENTS FORMULATION

A THESIS SUBMITTED TO
THE GRADUATE SCHOOL OF NATURAL AND APPLIED SCIENCES
OF
MIDDLE EAST TECHNICAL UNIVERSITY

BY

CANSIN BADE AYDIN

IN PARTIAL FULFILLMENT OF THE REQUIREMENTS
FOR
THE DEGREE OF MASTER OF SCIENCE
IN
MECHANICAL ENGINEERING

JANUARY 2020

Approval of the thesis:

DEFORMATION AND FAILURE ANALYSIS OF LAMINATED COMPOSITES BY ISOGEOMETRIC ELEMENTS FORMULATION

submitted by **CANSIN BADE AYDIN** in partial fulfillment of the requirements for the degree of **Master of Science in Mechanical Engineering Department, Middle East Technical University** by,

Prof. Dr. Halil Kalıpçılar
Dean, Graduate School of **Natural and Applied Sciences** _____

Prof. Dr. M. A. Sahir Arıkan
Head of Department, **Mechanical Engineering** _____

Prof. Dr. Haluk Darendeliler
Supervisor, **Mechanical Engineering, METU** _____

Examining Committee Members:

Prof. Dr. F. Suat Kadıoğlu
Mechanical Engineering, METU _____

Prof. Dr. Haluk Darendeliler
Mechanical Engineering, METU _____

Assoc. Prof. Dr. Merve Erdal Erdoğmuş
Mechanical Engineering, METU _____

Assoc. Prof. Dr. Ulaş Yaman
Mechanical Engineering, METU _____

Prof. Dr. Kemal Levend Parnas
Mechanical Engineering, TED University _____

Date:

I hereby declare that all information in this document has been obtained and presented in accordance with academic rules and ethical conduct. I also declare that, as required by these rules and conduct, I have fully cited and referenced all material and results that are not original to this work.

Name, Surname: Cansın Bade Aydın

Signature :

ABSTRACT

DEFORMATION AND FAILURE ANALYSIS OF LAMINATED COMPOSITES BY ISOGEOMETRIC ELEMENTS FORMULATION

Aydın, Cansın Bade
Master of Science, Mechanical Engineering
Supervisor: Prof. Dr. Haluk Darendeliler

January 2020, 120 pages

The finite element method (FEM) is the most widely used technique for solution of engineering problems. In classical finite element analysis (FEA) procedure, the exact geometry generated in computer aided design software is regenerated to have an analysis suitable model, then this model is used for solution. Isogeometric analysis (IGA) is a computational approach which eliminates the modification phase of the actual geometry in FEA. Instead, IGA employs the same mathematical model which defines the geometry in the computer graphics software for defining the solution field. One of the most general basis functions used for representing the geometry mathematically is Non-Uniform Rational B-Splines (NURBS). NURBS are more comprehensive form of B-spline functions which are parametric piecewise polynomials. They allow flexible and accurate design, control of continuity with ease, and with its rational form enabling representation of conic sections which is not possible by using B-splines. The main advantage of isogeometric approach is to analyze the complex shaped parts by eliminating the error due to inaccurate representation of geometry in the finite element method. In addition, since spline-based functions with higher continuity are used, better accuracy is acquired.

The aim of this thesis is, through the use of isogeometric plate elements, to analyze the deformation, to determine the strain and stress distribution and to predict the first ply failure by using different failure criteria of laminated composite materials, and to present the applicability of IGA for anisotropic materials. For this purpose, an open source code written for isotropic materials is modified to analyze laminated composites and various failure criteria are embedded to the code. A number of cases with various ply orientations and thicknesses, under different loading and boundary conditions are analyzed and their results are compared with the results obtained by the solutions of FEM.

Keywords: Laminated Composite, Isogeometric Analysis, IGA, First Order Shear Deformation Theory, Failure Theories

ÖZ

KOMPOZİT LEVHALARIN DEFORMASYON VE KIRILMA ANALİZİNİN İZOGEOMETRİK ELEMANLARLA FORMULASYONU

Aydın, Cansın Bade
Yüksek Lisans, Makina Mühendisliği
Tez Yöneticisi: Prof. Dr. Haluk Darendeliler

Ocak 2020 , 120 sayfa

Mühendislik problemlerinin çözümü için en sık kullanılan teknik, sonlu elemanlar yöntemidir. Klasik sonlu elemanlar analizi (SEA) yönteminde, bilgisayar destekli tasarım yazılımları ile oluşturulan kesin geometri, analize uygun bir modele sahip olacak şekilde yeniden oluşturulur ve bu model analiz için kullanılır. İzogeometrik analiz (IGA), SEA'daki asıl geometrinin sadeleştirildiği fazı ortadan kaldıran sayısal bir yöntemdir. IGA, bunun yerine çözüm alanını tanımlamak için bilgisayar grafikleri yazılımlarında geometriyi tanımlamak amacıyla matematiksel modeli kullanır. Geometrinin matematiksel tanımlanması için kullanılan en genel taban fonksiyonlarından biri düzenli olmayan rasyonel tabanlı eğrilerdir (NURBS). NURBS, parametrik parçalı polinomlardan oluşan taban eğrilerinin (B-spline) daha kapsamlı halidir. NURBS, esnek ve doğru tasarıma, yüksek mertebeden sürekliliğe kolay ulaşılmasına olanak sağlar, ve rasyonel yapısı sayesinde, B-spline ile ifade edilemeyen konik kesitlerin gösterimine imkan tanır. İzogeometrik yaklaşımın temel avantajı; karmaşık şekilli parçaların, sonlu elemanlar metodunda, geometrilerinin yeterli düzeyde betimlenememesinden meydana gelen hataların ortadan kaldırılarak analiz edilebilmesidir. Ayrıca, yüksek mertebeden sürekliliğe sahip eğri tabanlı fonksiyonların kullanımı ile

daha doğru sonuçlar elde edilir.

Bu tezin amacı, izogeometrik plaka elemanlarının kullanımıyla, tabakalı kompozit malzemelerin deformasyonunun analiz edilmesi, gerinim ve gerilme dağılımlarının belirlenmesi, farklı hasar kriterleri ile ilk tabaka hasarının öngörülmesi ve IGA yönteminin yön bağımlı elemanlara uygulanabilirliğinin gösterilmesidir. Bu amaçla, çeşitli fiber yönlerine sahip tabakalardan oluşan farklı kalınlıklardaki plaka örnekleri değişik yük ve sınır koşulları altında incelenmiş, sonuçlar SEA yöntemi ile elde edilen sonuçlar ile karşılaştırılmıştır.

Anahtar Kelimeler: Levhalı Kompozitler, İsogeometrik Analiz, IGA, Birinci Dereceden Kesme Deformasyon Teorisi, Hasar Teorileri

to my dear family

ACKNOWLEDGMENTS

I am grateful to have the opportunity to have the experience of this thesis study and I want to thank all those people who made this possible.

First and foremost, I would like to thank and express my candid indebtedness to my thesis supervisor Prof. Dr. Haluk Darendeliler. He guided and supported me with great patience like no one else can do. It is an honor to study with him and learn from him.

Additionally, I would like to thank the examining committee members Prof. Dr. Suat Kadıoğlu, Assoc. Prof. Dr. Merve Erdal Erdoğmuş, Assoc. Prof. Dr. Ulaş Yaman and Prof. Dr. Levend Parnas for their kind attention to my study and their wise commends.

I also want to thank my company Turkish Aerospace, my chief İbrahim Cengiz and all my co-workers, especially Selen Temel Yiğitbaşı and Kazım Tekkanat, for their understanding and intellectual support.

I would like to thank my friends who never give up believing in me. They were always beside me to increase my motivation. I would like to mention Talha Öz, who is by my side for more than half of my life; Ceren Özcan, Ziya Can and Anıl Güven Yüksel, who became a part of my life thanks to my dear husband and offer more than friendship.

I would like to thank my parents Sibel and Murat Güneş as well as Kudret, Osman and Aysu Aydın for their incredible indulgence and support.

The last but not the least I would like to thank my beloved spouse, my best friend and the supreme supporter Sertaç for taking care of me, calming my worries and all the things that he does. His importance and effect on my life is beyond this study and words are not enough to explain the meaning of him to me. I could not achieve this study or anything else without him. Thank you.

TABLE OF CONTENTS

LIST OF TABLES

TABLES

LIST OF FIGURES

FIGURES

LIST OF ABBREVIATIONS

ABBREVIATOINS

1-D \2-D \3-D	One \Two \Three Dimensional
B-Splines	Basis Splines
CAD	Computer Aided Design
CLPT	Classical Laminated Plate Theory
DOF	Degrees of Freedom
ESL	Equivalent Single Layer
FEA	Finite Element Analysis
FEM	Finite Element Method
FPF	First Ply Failure
FSDT	First Order Shear Deformation Theory
HSDT	Higher Order Shear Deformation Theory
IGA	Isogeometric Analysis
LTR	Length to Thickness Ratio
LW	Layerwise
NURBS	Non-Uniform Rational B-Splines
R-M	Reissner-Mindlin
SCF	Shear Correction Factor
SR	Strength Ratio
UD	Unidirectional

CHAPTER 1

INTRODUCTION

1.1 Background and Motivation

Humankind are trying to improve the materials since the beginning of the human history. From the stone age to present many materials and processing techniques are developed to meet the certain needs. Nowadays, in the technology based society, one of the main objectives is having lighter designs in many fields such as energy, automobile and aerospace. To fulfill this purpose, material technologies and analysis methods plays major roles in design. Fiber reinforced composite materials are one of the best result in engineering materials studies on enhancing the strength to weight ratio.

1.1.1 Composites; Properties, Advantages and Drawbacks

Composite materials are composed of several materials, which are not soluble in each other, combined in the macroscopic level to obtain a material which gathers the properties of its constituents [10]. Even in ancient history, humankind made early examples of the composite materials by mixing mud and straw and obtaining one of the most commonly used construction materials, adobe. As technology developed, needs are increased simultaneously, and constituents get sophisticated.

Depending on the constituents, composite materials can have high specific strength and specific modulus, long fatigue life, wear resistance, endurance to high temperature gradients, better health characteristics, etc. [11]. There are numerous applications of composites in the industry due to these favorable properties of the material. Some

of the application areas are; aerospace structures, nuclear plants, automotive, marine and underwater structures, buildings, and sports industry.

The constituent with higher strength is called reinforcement, and the other material covering the reinforcement is called the matrix. The reinforcement increases the mechanical properties of the material and the matrix connects the reinforcements, distributes the force, and by covering them, guard the reinforcements from the environment [10]. There can also be a porous core material in some applications to increase bending stiffness. Since composite materials have several ingredients, they have an endless variety, and some of them can require design and analysis procedures different from each other according to the used type. Composite materials can be classified according to their texture, or according to their constituents. According to texture, some of the most common types are; fiber reinforced, particulate reinforced and flake reinforced composites. In the case of fiber reinforced composites, the texture may still vary according to arrangements of the fibers. There are woven fabrics in which fibers are combined in textile-like forms, and there are unidirectional (UD) fibers that all the fibers of a layer oriented in the same direction. In respect of constituents, different reinforcement and matrix materials are in use. The frequently used fiber materials are carbon, glass and aramid. There are various matrix materials like polymers (thermoplastic or thermoset), metals, ceramic or even carbon, but the most commercially used matrix materials are polymer resins, such as epoxy, phenolic and polyester [10].

Mechanical properties of the fiber reinforced composites are not isotropic due to their fibrous nature. Strength on the fiber direction is considerably higher than the strength on the other directions. This property allows a flexible design to enhance mechanical properties only in necessary directions. On the other hand, anisotropic nature requires unique analysis procedures.

The main challenges of the composites come from their constituents and heterogeneous nature. Since it is a combination of several materials, standardization of the material is harder. Allowables of the material require many tests. In this study, unidirectional (UD) fiber reinforced prepregs with thermoset resins are used. In the manufacturing process of the prepregs, fiber sheets are impregnated with the uniformly distributed resin. Prepregs are suitable for layup or molding operations. The thermoset

resin is affected by environmental conditions severely before it is cured. Therefore, prepregs are stored in refrigerators for a limited time then they are scrapped. Also, the layup is performed in environmentally conditioned, clean rooms, and they require vacuum bagging and curing in autoclave with pressure and heat. Manufacturing quality has severe effects on mechanical properties. Thus, composite materials subjected to relatively expensive non-destructive testing methods, such as ultrasonic testing. They also exhibit distinctive failure modes such as delamination, which is challenging to analyze and hard to discover in standard maintenance.

1.1.2 Development of Isogeometric Approach

Design process in industrial applications include many parameters such as manufacturability, assemblability, material selection, strength, weight, cost etc. To fulfill these requirements, both parts and final assembled product should be visible with all details to the designers. For this purpose, computer aided design (CAD) softwares are being widely used worldwide in design departments for several decades. Before computerization, designs were represented in 2-D blueprints. With developing technology, 2-D drawings relinquish its place to 3-D models. For computer representation of geometries with accuracy, math-based definition of the shapes were required. First, Casteljau used Bernstein polynomials for parametric expression of the curves and surfaces [12, 13], followed by Bézier with the curves named by himself [12, 14] and computer implementation of B-splines by Riesenfeld and Richard [12, 15] which allows local changes of the shape. Afterwards, a more comprehensive spline expressions called non-uniform rational B-splines making representation of conical sections possible [12]. At the present time, the NURBS are the mathematical method forming the basis of the geometrical representations of the CAD softwares. Since, the NURBS are parametric functions for geometrical modeling, the geometry generated by these softwares are exact.

While CAD softwares are used for design, finite element analysis (FEA) softwares are favored for analysis. These softwares usually use piecewise-linear or piecewise-quadratic geometric approximations for the solution instead of exact geometry. A new and approximate geometry, also known as analysis suitable geometry, is prepared for

analysis purposes by stress engineers based on the exact geometry. The quality of the analysis strongly depends on the quality of this approximation which is not unique. Creation of this analysis suitable geometry and meshing takes about 80% of the total time for analysis [7, 1] and involve many simplification of actual geometry. Deviations between exact CAD geometry and approximate geometry generated for analysis lead inaccurate results in analysis. In 2005, Hughes, Cottrell and Bazilevs proposed a method called isogeometric analysis (IGA) to close this time consuming gap between CAD and FEA environments [7]. The underlying concept of isogeometric analysis is using the functions representing the exact geometry for the solution domain of dependent variables [7].

1.2 Objective of the Thesis

The main objective of this thesis is carrying out a study to use the isogeometric approach for analyzing the deformation and strain-stress distribution of laminated composites under transverse loading. By the development of a solution procedure that allows using the exact geometry in the analysis model for composite laminates, refinements do not require any iterations between the CAD and the FEM softwares and it is possible to analyze laminated composites with good accuracy. Constructing the geometry by means of the NURBS basis functions and using the isogeometric analysis method, an easily adjustable analysis model especially for analysis of the design data in development phase is tried to be achieved. Moreover, integrating several failure criteria to the model enable the desired failure theory to be used and results of them to be compared.

1.3 Review of Previous Work

In this section, the previous studies in the literature are summarized starting with briefly mentioning the studies about laminated composite analysis, then moving to the development and applications of isogeometric analysis; lastly, covering the researches about isogeometric analysis for analyzing composite plates.

1.3.1 Analysis of Laminated Composites

Pagano [16] studied on the validity of the CLPT. He compared the results of the CLPT for cylindrical bending with elasticity solution by implementing both techniques to the solution of a unidirectional one layer plate, a bidirectional two-layered plate, and a bidirectional three-layered plate all under the same sinusoidal loading. He finds out that while the results of stresses converge to the linear elasticity solution rapidly as the ratio of the effective dimension to thickness increases. On the other hand, convergence of the displacement is slower. The results of this study play a significant role in further developments of composite plate analysis methods. Since linear elasticity solution does not have assumptions for simplification and considers shear deformations. Next year, Pagano [17] published another paper to deepen his study on limitations of the classical laminated plate theory (CLPT), providing 3-D elasticity solution for rectangular laminated and sandwich composites. This time, he studied on a simply supported plate under static bending. He presented the acceptable cases for using the CLPT, and the cases theory loses its accuracy. As his previous study, the role of this study is crucial in checking the validity of the new theories since the exact solution was supplied. In 1994, Reddy and Robbins [18] published an article covering the many theories for structural analysis of laminated plates in detail. They also explain a method which applies different modeling techniques for the regions requiring 3-D stress field and other regions. By doing so, a more optimal model is generated since high computational cost is reduced while preserving the accuracy. Castellazzi, Krysl and Bartoli [19] using nodally integrated plate elements (NIPE) focused on a solution for locking problem created by the curvature caused by shear that cannot be properly expressed in FEM model with increasing length to thickness ratio (LTR). They used the FSDT formulation for the analysis of composite laminates. Their approach includes formation of novel elements with monoclinic properties and composing the strain-displacement relations at nodes. During the validation phase, they found consistent results with analytical and the FEM solutions. Yu [20], advanced the Reissner-Mindlin (R-M) theory by starting with a 3-D formulation and converting to a more standard 2-D plate problem by means of variational asymptotic method. He come up with as accurate results as HSDT and LW theories. Adim, Daouadji and Rabahi [21] proposed a method for eliminating the SCF by hav-

ing a non-linear distribution of the shear stress in transverse direction. They assumed uncoupled shear and bending for displacement in thickness direction, and applied a refined HSDT. They affirm their solution by comparing with 3-D elasticity solution. They also claimed that, their theory is more convenient than other HSDTs since it is a refined theory with less unknowns and they even made the refined HSDT simpler. Analysis is an important and difficult issue since the introduction of the composite materials. Many researches were conducted and numerous theories are proposed for modeling their layered structure. In addition to the ones, mentioned in this chapter, the main theories will be explained in Chapter 2.

1.3.2 Development of Isogeometric Analysis

The finite element method began to developed around the 1950's to decrease the need for experiment and testing and has been widely used for solving engineering problems since then. While the finite element method has been used for several decades when computer aided design entered the life of the engineers. The different origins of these two technologies cause distinctions in their logic; therefore, models. The parametric mathematical models of CAD programs are improved together with the visualization they created. Nowadays, NURBS functions are being widely used for generation of geometries in these softwares. Piegl and Tiller [5] explained the formation, properties and applications of B-spline and NURBS functions in detail in their book. Even after introducing of the isoparametric method, the FEM uses linear shape functions; whereas, geometry is represented by precision using NURBS functions in design. In 2005, Hughes, Cotrell and Bazilevs [7] introduced a new analysis method representing the geometry exactly by using NURBS basis functions as CAD softwares. Beside eliminating the geometry assumption, isogeometric concept also expedite the cumbersome meshing process which requires iterations between CAD and FEM geometries. Even in the first published paper, they present various application areas of the method promoting by numerical examples, from structural mechanics to electromagnetics. To authenticate the newly introduced method, they showed the consistency between the previous studies and exact analytical solutions whenever available. Since than the IGA method is applied to wide variety of problems. A few years later, Cotrell et. al. [1] explained the methodology and implementation of the IGA comprehensively

in their published book. They extend the application fields mentioned in the previous paper [7] to include nonlinear problems, dynamic problems such as vibration, wave propagation and turbulence.

Even though the IGA attracted many researchers, many were distant to the subject because of the onerous computer implementation of an unfamiliar concept. Falco, Reali and Vázquez [22] developed free software called GeoPDEs to provide a convenient way for the ones who want to implement IGA to their studies and develop new methods. They explained the design, architecture, and features of the software. They also provide examples for linear elasticity, Strokes and Maxwell problems. Then, Nguyen, Anitescu, Bordas and Rabczuk [8], further developed the GeoPDEs, covering h-, p-, k- refinements, widening the scope to cover multidimensional cracks and material interfaces and they made the program compatible with also T-splines. They verify their code by presenting several example problems and comparing their results with exact solutions and academic studies.

Although IGA defines the geometry in the same way as CAD programs, the description may not always suitable for analysis, such as trimmed geometries. In the early days of the IGA, trimmed geometries were one of the major problems. Marussig [23] focused on solving the robustness and inaccuracy problem of the objects after trimming operation. He proposed a procedure called extended B-splines with local refinement to solve the problem of applying the IGA method in trimmed geometries.

Other than studies on B-splines and NURBS, other spline based functions like T-splines [24, 25, 26], PHT splines [27] and RHT splines [28] are conducted by the IGA concept.

1.3.3 Applications of Isogeometric Analysis

Besides the papers about the method itself, there are many applications of the IGA in many fields, such as structural analysis [1, 29, 30, 31, 32, 33], fluid mechanics and fluid-solid interactions [34, 24], electromagnetics [35] and contact mechanics [36]. Since the scope of this thesis is application of the IGA to the structural analysis, the content of the researches on this subject is covered.

Zhang, Alberdi and Khandelwal [37] are worked on the three dimensional curved beams. They deal with the shear locking phenomena by using functions with higher orders. Especially with the fourth order functions, they resolve the problem. Tsiptsis and Sapountzakis [38] are analyzed closed and open section curved beams under combined loading. They concluded that using the IGA more accurate results can be obtained with less computational cost. Because of the effect of the exact geometry is particularly greater for curved beams, Rafenkovic and Borkovic [39] also used the IGA for their studies on curved beams. Espath, Braun, Awruch and Maghous [33], aimed on analyzing structured with nonlinearities by uniting the IGA and corotational method. This method approaches 3-D state by separating problem into two parts, one is only associated with deformation and other with translation. They both conduct studies on linear and nonlinear cases. They observed reduce in computational expense by using higher order polynomials with sufficient but lower continuity. They summarize the minimum required orders for procedures both linear and with nonlinearities.

Considering the researches combining the IGA and composite analysis, there are many studies ranging from beam analysis to nonlinear post-bucking analysis. Hasim [40] applied the IGA method for composite beams. He used a refined zigzag theory. He specifies the advantages of this theory as independence from the number of layers, is not exposed to shear locking, and does not include geometric errors; however, it cannot provide shear stress continuity. To cope with this problem, he proposed calculating transverse component after the axial components of the stress field using the Cauchy's equilibrium equation. To test the proposed procedure, he performed analysis on beams with different aspect ratios and sandwich beam. He compared the results with literature and results from commercial software and observed good agreement. Faroughi, Shafei and Eriksson also worked on IGA solution of laminated beams [41]. They proposed "displacement-only" model, which does not take rotational DOFs into account. Their approach is also adequate to model relations between layers and delamination.

Fan, Zeng, Huang and Liu [42] intended to improve computational effort of laminated plate analysis according to FSDT using the IGA. They also suggest a new method called "Fast Plate Analysis based on Tensor-decomposition", which includes express-

ing the matrices of structural analysis as tensor product by means of IGA. They gain time in computation by decreasing the complexity of algorithms. They present several examples covering constant and varying stiffness cases and both more standard shapes and slightly complicated shapes whose Jacobian is not diagonal. They claimed to have excellent improvement in computational complexity and their approach is very suitable for optimization studies. Another study of laminated composite plates is conducted by Thai, Nguyen-Xuan, Nguyen-Thanh, Nguyen-Thoi and Rabczuk [43]. They also used the R-M plate model with an improvement on shear terms proposed by [44]. They applied the method to static, free vibration, and buckling problems with elements of many orders to show the performance and observe perfect agreement with the other methods in the literature. Thai, Nguyen-Xuan, Bordas, Nguyen-Thanh and Rabczuk also used the HSDT of order three for analysis of composite plates [45]. Because of higher order approximation they eliminate the SCF while achieving essential continuity with ease under favor of NURBS functions. They repeated the same analysis in their previous paper [43] with this method. They asserted results of their method competes with many other methods and even achieve better accuracy for interlaminar stresses. In another paper, Thai, Ferreira, Bordas, Rabczuk and Nguyen-Xuan proposed a new method called "Inverse Tangent Shear Deformation Theory" [46]. In this theory, a tangential displacement field assumed so that variation of shear stress does not require a SCF. They investigate the effects of LTR, core to lamina ratio for sandwich plates, different geometries and boundary conditions in several testing examples for the same analysis as previous papers [43, 45]. When results are compared to other published work including other trigonometric theories, they observed satisfying accuracy. The HSDT of order five is implemented to the IGA for composite plate analysis by Nguyen-Xuan, Thai and Nguyen-Thoi [47]. Due to high order of displacement assumption traction-free surfaces are achieved on the model. They conducted analysis in the previous works [43, 45, 46] for both laminated and sandwich plates for symmetric and antisymmetric lamination schemes. Similar to the previous work C^1 continuity is achieved without any difficulty by means of the basis of IGA method. As cited from their study, the proposed method is a rival to semi-analytical, FEM and meshless methods achieving good agreement with exact 3-D elasticity solutions, especially for interlaminar stress distribution. Thai, Ferreira, Carrere and Nguyen-Xuan [48], implement LW theory to the IGA for the

same analysis mentioned in previous papers [43, 45, 46, 47]. Using a LW theory, they aimed to get more accurate results for transverse shear and does not need any SCF since theory models each layer by the FSDT and relating layers by a condition on displacement. The obtained result are highly promising for plates independent of thickness, and theory calculates the transverse components more accurately than the FSDT and HSDT. Li, Zhang and Zheng [49] applied HSDT of order three to laminated plates in 2014. They mainly focused on analysis of comparatively complex geometries. They performed free vibration and static analysis. They get admissible results for thick plates which cannot be modeled by lower order theories properly besides very thin plates which suffer from locking is solved by refining the mesh with drawback of increasing computational expense. In the same year, the HSDT of order three is used by other researchers for thick composite plate analysis. Pekovic, Stupar, Simonovic, Svorcan and Komarow used basis functions of order 2,3 and 4 for analysis of sandwich and laminated plates, compared their results with FSDT, other third order HSDT and exact solutions, and observe accuracy of their study. In 2017, Gupta and Ghosh [50] present their research about bending analysis of R-M plates by IGA. They analyzed plates with different boundary conditions and with second, third and fourth order basis functions. They also mentioned the validity of the method.

One of the most comprehensive studies is performed by Tran, Lee, Nguyen-Van, Nguyen-Xuan and Wahab [51]. They applied IGA to laminated composite plates using the HSDT. They performed both linear and non-linear bending and transient analysis. They used the developed by Reddy. They eliminate the need for the SCF in lower order theories and satisfy zero-traction conditions at the surfaces of the plate while achieving the required continuity of the HSDT effortlessly thanks to the NURBS basis functions. For nonlinearity, they used Lagrange approach with small strain and moderate rotation assumptions. They analyze a clamped plate subjected to uniform load, circular plate under uniform pressure, and several symmetric and anti-symmetric laminated plates. They observe the effect of fiber orientation for anti-symmetric laminates. They also performed nonlinear transient analysis for dynamic systems. They compared their results with solutions in literature, and they achieved a general agreement and even more accurate results in some cases compared to the most used solution techniques. Kapoor and Kapania [52] obtained FSDT formula-

tions for Von-Karman geometrical nonlinearities applying variational approach to analyze composite plates using the IGA. They also provide a solution for the plates with high LTR. They suggested using second order NURBS with k-refinement to eliminate the artificial stiffer behavior of the laminate. As cited in their paper, they constitute their nonlinear model by Newton-Raphson procedure, involving large displacement in thickness direction with small strains and moderate rotations. According to their results they obtained good accuracy with less DOF than FEM. Le-Manh, Luu-Anh and Lee [53] are also studied on the same subject. Similar to the previous work of Kapoor et. al [52], they used FSDT formulation with iterative process of Newton-Raphson to derive relations for nonlinear model to be implemented to the IGA for bending analysis. Their model account for large deformation and in-plane strains and small rotations. They validate their method by comparing several numerical examples covering different geometries, orientations and thicknesses with previously published studies.

Delamination is one of the most limiting parameters of the composite design. Nguyen, Kerfriden and Bordas [54] duplicate the control points using knot insertion to model the delamination surfaces by isogeometric cohesive elements. After comparing the results with the published papers, they concluded their method is highly favorable to study delamination. Kapoor, Kapania and Soni [55], applied several degrees of NURBS based IGA to find interlaminar normal and shear stresses in laminated composite plates. They used the FSDT, and also 3-D elasticity equations in the transverse direction. They verified their results in various numerical examples and compared results with 3-D elasticity solution.

The numerical integration technique implemented is Gauss quadrature in most of the published papers. Even though it is the most widely used numerical integration rule for the IGA method and seems adequate at first [1], researchers find out that the convenience of the Gauss quadrature in terms of efficiency is very low for IGA method. Auricchio, Calabro, Hughes, Reali and Sangalli [56] proposed a more suitable quadrature technique for IGA. Even though Galerkin technique is widely used method with isogeometric analysis, there are also studies with other numerical methods. Pavan and Rao [57] using the isogeometric collocation method to perform bending analysis, they are able to use strong form of the governing equations. The

collocation method, has less computational cost due to less number of integration points. They applied the isogeometric collocation method with three different formulations to several problems, and accuracy and computational expense are evaluated. Especially the results of the two of the formulations seem promising.

1.4 Scope of the Thesis

In this thesis study, analysis of composite plates are carried out for square and rectangular laminates under various loading, unidirectional fiber reinforced laminated composites with polymer resins are examined. To see the affect of the ply orientations, cross-ply and angle-ply symmetric laminated composites are investigated. To observe the effect of the boundary conditions on the displacement, one of the orientation schemes is chosen and analyzed for one-end clamped and two-ends clamped boundary conditions. For the first-ply-failure estimation, five different failure criteria, namely maximum stress, Tsai-Hill, Hoffman, Tsai-Wu and Hashin, are implemented and their results are compared for each test case. All of the analyses are conducted by isogeometric element formulation with NURBS basis functions using first order shear deformation theory by development of the open source code MIGFEM [8]. The numerical results are compared with the 2-D orthotropic laminated shell analysis performed in MSC Nastran.

1.5 Outline of the Thesis

The layout of this thesis is as follows:

In Chapter 1, a brief background information is provided and the motivation to start working on the subject is explained, followed by the objective of the thesis study. Then, previous studies in literature is reviewed and the scope and the outline of the thesis are stated. In Chapter 2, plate theories used for laminated composite analysis and several composite failure theories are examined. Isogemetric analysis (IGA) method is introduced in Chapter 3. Basic concepts of the IGA, its application procedure and differences from the classical finite element analysis method are explained

in detail. Formulations used hroughout the analysis is derived in Chapter 4. Afterwards, to verify the validity of the procedure, results obtained by the formulation is compared with the exact solution and the several numerical examples are presented and they compared with the finite element analysis solutions performed on a commercial software, MSC Nastran in Chapter 5. In Chapter 6, the results are summarized and conclusions are drawn. Lastly, suggestions for future studies are given.

CHAPTER 2

PLATE AND FAILURE THEORIES USED FOR COMPOSITES

The fiber reinforced laminated composites are strong in the fiber direction and weak in the other directions compared to isotropic counterparts. Because of that, in most applications, their thickness is small with respect to its planar dimensions. Therefore, making plate and shell assumptions while modeling fiber reinforced composite laminates is a reasonable approach [9, 20].

2.1 Plate Theories used for Composites

There are several theories for the analysis of composite plates. The leading theory behind most of these theories is the 3-D elasticity theory for anisotropic materials. Other methods are derived by making certain simplifications to the 3-D elasticity theory. Theories for analyzing laminated composite plates can be classified into three main groups by their approach to the material. These are equivalent single-layer theories, three-dimensional elasticity theories, and multiple model methods [9].

The equivalent single layer (ESL) theories are the most commonly used theories because of their advantages, such as ease of modeling the problem, constructing the constitutive relations, and low computational cost [43]. In these theories, an assumption is made for variation of the displacement field, and the laminated plate is handled as an equivalent single layer with anisotropic properties. Under this assumption, the 3-D continuum problem reduces to a 2-D problem [18]. The ESL theories give accurate results for thin and moderately thick plates. However, because of the low transverse shear stiffness of composites, thick plates tend to deform considerably under transverse shear stress; therefore, the results of the ESL theories lose their accuracy

as the plate gets thicker [9, 18]. The ESL theories are also yielding poor results in the calculation of interlaminar stresses and not sufficient to predict ply level stresses near geometric and material discontinuities and in highly loaded areas. In addition, they cannot be used for delamination analysis [9, 43, 18].

The most common ESL theories are; classical laminated plate theory (CLPT), the first order shear deformation theory, and higher order shear deformation theories. Each of them will be explained in detail in the following sections.

The three-dimensional theories are the tools to calculate the results close to the exact solution. In these theories, layers are modeled separately as homogeneous anisotropic mediums [58]. As the number of layers increased, the model becomes complicated and has a high computational cost. Even though 3-D theories are capable of solving geometric complexities, arbitrary boundary conditions, lamination schemes, and nonlinearities; however, solution procedure may be very troublesome and even impossible.

There are also layerwise theories, instead of modeling laminate as an equivalent single layer, they model continuous displacement field with not necessarily continuous derivatives in the thickness direction. Therefore, it is like combination of many equivalent layers. Especially, for moderately thick or thick laminates this theory ensures better kinematic representation [18].

2.1.1 Classical Laminated Plate Theory (CLPT)

The Classical Laminated Plate Theory (CLPT) is also known as Kirchhoff Theory for composite plates since it is an adaptation of Kirchhoff's plate theory. Like its origin, the CLPT is not a suitable theory for thick plates and only covers small deflections. Assumptions of the CLPT are listed below [9]:

i. Normals of the mid-plane (transverse normals) before deformation, remain straight and normal to the mid-plane after deformation.

ii. Normals of the mid-plane are inextensible.

iii. Both transverse shear and transverse normal effects are neglected. Therefore,

plate deforms only under bending and in-plane stretching.

The CLPT is constituted by assuming a displacement field. Strain and stress fields derived from this displacement field. The displacement field of the CLPT is given below:

$$\begin{aligned} u(x,y,z) &= u_0(x,y) - z\frac{\partial w_0}{\partial x} \\ v(x,y,z) &= v_0(x,y) - z\frac{\partial w_0}{\partial y} \\ w(x,y,z) &= w_0(x,y) \end{aligned} \tag{2.1}$$

As the field indicates, in the CLPT, deformations are solely due to bending and in-plane stretching; that is to say, it does not take transverse shear and transverse normal effects into account. Resulting from the high ratios of the effective elastic modulus and effective shear modulus in fiber direction and transverse direction of laminated composite plates, encountered error in CLPT is high. The CLPT method results in lower deflections values than the actual and grater natural frequencies and buckling loads [58]. Therefore, the CLPT is applicable only to thin plates, i.e., thickness to span ratio less than 1/10 [11]. Exceedingly poor results are obtained as the plate gets thicker [20]. In addition, the classical laminated plate theory loses its accuracy as there exists a sudden increase or localization of the forces. The CLPT results in errors, particularly around the boundaries of the plate and support reactions, since it relies on the Kirchoff plate theory [59]. Lastly, the CLPT the required continuity of the theory is C^1 for transverse displacement; in other words, derivatives of the function should be continuous beside the function. This obligation complicates the finite element model [18].

2.1.2 First Order Shear Deformation Theory (FSDT)

The first order shear deformation theory (FSDT) is an improved version of the CLPT. The FSDT for composite plates is widening the scope of the FSDT for anisotropic plates by Pegano and Whitney [60, 55]. Different from the CLPT, takes into account transverse displacements by eliminating the assumption of the transverse normals

of the mid-plane will remain normal after the deformation. The FSDT is applicable to moderately thick plates beside thin plates [49]. This theory assumes constant displacement in the thickness direction. Due to this non-physical assumption, the FSDT requires shear correction factor (SCF) stands for the nonlinear distribution of the shear stress and satisfy traction-free boundary condition at the top and bottom plate surfaces [50, 51]. The SCF is an dimensionless quantity depending on material coefficients, alignment of the plies, geometry of the plate, loading and boundary conditions [43, 49]. Consequently, it is not an easy to find impeccable SCF. While researches are trying to improve SCF [61], more common approach is using constant SCF, most commonly 5/6.

Assumptions of the FSDT are listed below [9]:

i. Normals of the midplane (transverse normals) are inextensible.

ii. Out of plane stress, σ_{33}, is set to zero. Therefore, transverse displacement, w, is independent of the coordinate in thickness direction.

iii. Transverse shear strain is constant throughout the thickness

By considering the second assumption, degrees of freedom reduces to 5 which includes 3 translations: u,v,w, and 2 rotations: ϕ_{x}, ϕ_{y}, rotations about x and y axes, respectively.

Displacement field of the FSDT is as follows:

$$\begin{aligned} u(x,y,z) &= u_0(x,y) + z\phi_x(x,y) \\ v(x,y,z) &= v_0(x,y) + z\phi_y(x,y) \\ w(x,y,z) &= w_0(x,y) \end{aligned} \tag{2.2}$$

Including transverse shear strains, results of the FSDT is more accurate than the CLPT. It is also require less effort to implement since it does contain any derivative terms. However, the FSDT also has limitations. Known parabolic distribution of the shear strain along z-direction cannot be procured; thus, aforementioned SCF is needed in the theory to ensure that there is an agreement between results of the FSDT and the theory of elasticity [59]. As the LTR increases for a plate, the FSDT

may generate factitious transverse shear stiffness in numerical solution, which is also known as shear locking [18]. To obviate this issue, many researches have been conducted, such as higher order elements are used [18], selective integration scheme is applied [62, 63, 64] or k-refined quadratic NURBS elements are used [55]. Moreover, the traction-free boundary condition cannot be fulfilled at plate surfaces. The interlaminar stress analysis cannot be performed properly since obtained interlaminar stresses at the interfaces are discontinuous according to the FSDT [55]. Additionally, the FSDT is suitable for 2-D problems. It does not give accurate results for 3-D problems [59]. Lastly, the FSDT requires C^0 continuity of variables, which makes the theory more favourable than the CLPT considering complexity of conforming FEM elements [18].

2.1.3 Higher Order Shear Deformation Theories (HSDT)

The higher order shear deformation theories (HSDT) are using second or higher order polynomials while assuming displacement field. These theories also assert some additional unknowns, which have not an obvious physical meaning, to displacement field expressions for each additional power to get accurate results [9, 58]. The HSDT are better for modeling plates with high thickness, where transverse deformations plays an important role [65]. Certain drawbacks of the FSDT, like satisfying the traction-free boundary conditions on plate surfaces and need of SCF is still valid for some of the HSDT, but some of them overcome these difficulties. One of the most popular HSDT for laminated plates that assure the traction-free boundary conditions on plate surfaces and eliminate the requirement of SCF is the third order theory developed by Reddy [58]. The transverse components change quadratically in this theory [18].

The field of displacement of this theory is given below [58]:

$$\begin{aligned} u(x,y,z) &= u_0(x,y) + z\psi_x(x,y) + z^2\xi_x(x,y) + z^3\zeta_x(x,y) \\ v(x,y,z) &= v_0(x,y) + z\psi_y(x,y) + z^2\xi_y(x,y) + z^3\zeta_y(x,y) \\ w(x,y,z) &= w_0(x,y) \end{aligned} \tag{2.3}$$

Accuracy of the results of the HSDT models are slightly outperforming the FSDT models. The HSDT also better for solutions of interlaminar stresses and displace-

ments [51, 49]. Moreover, the HSDT provide more stable results [11]. Nevertheless, the HSDT require C^1 continuity of displacement field, causing difficulties in FEM elements [51]. In addition, effort for computing is greater than the FSDT [9]. For high order theories as the order of the theory increase accuracy gained is unmentionable with substantial rise in computational cost; thus, higher order theories are not common [18].

2.1.4 3-D Elasticity Theories

The three dimensional elasticity theory for composite plates and sandwiches is primarily studied by Pagano [16, 17, 51]. By using 3-D elasticity method, exact solutions of the problems can be obtained [18, 33]. The continuum elements are fully nonlinear and can solve shell problems as well as plate problems since they do not have plate simplification assumptions [18]. In the solution of interlaminar stresses and problems like warping, 3-D elasticity method gives more precise results [43]. However, formulation of the 3-D elasticity solution is very complicated and sometimes even impossible for many problems having complex geometries, lamination schemes or arbitrary boundary conditions [51]. Even though adequate method to model thick composite laminates is 3-D elasticity method, increase in ply numbers results in dramatical rise in the computational effort because of 3-D elasticity theory models each ply of the composite plate as a 3-D solid [51]. There are attempts to reduce the complexity of the 3-D formulation without losing much of the accuracy of the solution. For example, for plates, using advantage of smallness of the thickness coordinate, 3-D problem is split into a 1-D and a 2-D problems [20].

2.1.5 Layerwise Theories

The layerwise (LW) theories are like a step between 3-D elasticity theories and ESL theories. There are full and partial LW theories. The full LW theories can calculate interlaminar stresses near discontinuities precisely [18]. However, in conjuction with increasing layer numbers to achieve the desired variation of the transverse displacement, computational effort reaches full 3-D analysis level [66]. To overcome this

problem, partial LW theories are constrained by assuming shear strain in transverse direction constant only sectionally and its normal counterpart is zero, with drawback of loosing this accuracy.

2.2 Failure Theories used for Composites

To investigate failure characteristic of the composite laminates the scale of modelling should be decided. Three different scales that for failure prediction are: the microscopic scale, the mesoscopic scale and the macroscopic scale [67]. The microscopic scale is the scale of lamina constituents. Fiber-matrix interactions are considered, and good for estimating crack initiation, but the microscopic failures do not always cause laminate failure. The mesoscopic scale is the scale of the layer. For failure prediction, stresses and strains of a single lamina is used. Lastly, the macroscopic scale is the scale of laminate. This scale make a homogenization to the laminate and does not consider positions or orientations of individual laminae, instead it uses stresses and strains of the laminate for failure estimation [67].

Even after deciding the scale, the failure estimation of composite laminates is not straight-forward as isotropic counterparts. The laminated composites do not yield, their failure modes are fiber fracture or buckling under tension or compression, respectively, crack formation in matrix, fibre debonding and delamination of the plies of the laminate. In most cases the failure modes are not catastrophic, but causes localized damage. After the localized failure, stresses on the lamina are redistributed [68]. Simultaneous and interactive development of the failure modes makes the failure prediction difficult for laminated composites [3].

The first-ply-failure (FPF), as the name indicates, means not necessarily the total failure but only the failure of the weakest lamina [68].

In this section, several failure theories for the FPF will be covered, which are, maximum stress failure criteria, Tsai-Hill failure criterion, Hoffman failure criterion, Tsai-Wu failure criterion and Hashin failure criteria. There are many other failure theories exist in literature, such as maximum strain, Puck, modified Puck and Yamada-Sun theories. However, maximum stress, Tsai-Hill, Hoffman, Tsai-Wu and Hashin crite-

ria are implemented and their results are compared in this thesis study.

The failure theories require the material properties given in Table 2.1.

Table 2.1: Abreviations of the material properties of a composite laminate.

$(\sigma_1^T)_{ult}$	Ultimate strength in tension in the first material direction
$(\sigma_1^C)_{ult}$	Ultimate strength in compression in the first material direction
$(\sigma_2^T)_{ult}$	Ultimate strength in tension in the second material direction
$(\sigma_2^C)_{ult}$	Ultimate strength in compression in the second material direction
$(\sigma_3^T)_{ult}$	Ultimate strength in tension in the third material direction
$(\sigma_3^C)_{ult}$	Ultimate strength in compression in the third material direction
$(\tau_{12})_{ult}$	Ultimate shear strength (in-plane)
$(\tau_{23})_{ult}$	Ultimate shear strength (out of plane, matrix-matrix shear)
$(\tau_{13})_{ult}$	Ultimate shear strength (out of plane, fiber-matrix shear)

The failure criteria classified by treatment to the interactions of the strains and stresses on different principle directions. They can be non-interactive, interactive or partially interactive.

A non-dimensional property named strength ratio (SR) is defined have a sense of the criticality of the quantity of the applied load [10]

$$SR = \frac{\text{Allowable Maximum Load Before Failure}}{\text{Applied Load}} \tag{2.4}$$

The strength ratio is always positive and means the structure can withstand SR times the load applied.The strength ratio can be defined for every failure theory and allows comparison of the different theories. The layer will be safe if $SR > 1$, and failure will be predicted if $SR < 1$.

2.2.1 Maximum Stress Criteria

The maximum stress criteria compares the stresses in material directions to the respective strengths without considering any interaction. If the stress is greater than the corresponding strength, lamina is said to be failed. In other words, the lamina is

considered to be safe if

$$
\begin{aligned}
-(\sigma_1^c)_{ult} < \sigma_1 < (\sigma_1^T)_{ult}, \text{ or} \\
-(\sigma_2^c)_{ult} < \sigma_2 < (\sigma_2^T)_{ult}, \text{ or} \\
-(\sigma_3^c)_{ult} < \sigma_3 < (\sigma_3^T)_{ult}, \text{ or} \\
|\tau_{12}| < (\tau_{12})_{ult}, \text{ or} \\
|\tau_{23}| < (\tau_{23})_{ult}, \text{ or} \\
|\tau_{13}| < (\tau_{13})_{ult}.
\end{aligned}
\tag{2.5}
$$

The graphical representation of the maximum stress criterion for stresses σ_1 and σ_2 is shown in Figure 2.1. The region outside the square is predicted unsafe. Strength ratio is found by using individual strength ratios of the criteria

$$
\begin{aligned}
&\text{if} \quad \sigma_1 > 0, && SR_1 = \frac{(\sigma_1^T)_{ult}}{\sigma_1} \\
&\text{if} \quad \sigma_1 < 0, && SR_1 = -\frac{(\sigma_1^C)_{ult}}{\sigma_1} \\
&\text{if} \quad \sigma_2 > 0, && SR_2 = \frac{(\sigma_2^T)_{ult}}{\sigma_2} \\
&\text{if} \quad \sigma_2 < 0, && SR_2 = -\frac{(\sigma_2^C)_{ult}}{\sigma_2} \\
&\text{if} \quad \tau_{12} > 0, && SR_3 = \frac{(\tau_{12})_{ult}}{\tau_{12}} \\
&\text{if} \quad \tau_{12} < 0, && SR_3 = -\frac{(\tau_{12})_{ult}}{\tau_{12}} \\
&\text{if} \quad \tau_{23} > 0, && SR_4 = \frac{(\tau_{23})_{ult}}{\tau_{23}} \\
&\text{if} \quad \tau_{23} < 0, && SR_4 = -\frac{(\tau_{23})_{ult}}{\tau_{23}} \\
&\text{if} \quad \tau_{13} > 0, && SR_5 = \frac{(\tau_{13})_{ult}}{\tau_{13}} \\
&\text{if} \quad \tau_{13} < 0, && SR_5 = -\frac{(\tau_{13})_{ult}}{\tau_{13}}
\end{aligned}
$$

Therefore, strength ratio of the maximum stress criteria is the minimum of the individual strength ratios

$$SR = min(SR_1, SR_2, SR_3, SR_4, SR_5) \tag{2.6}$$

The maximum stress criteria is a widely used theory since it only require uniaxial test data, specify the failure mode causing the failure and good for first approximation.

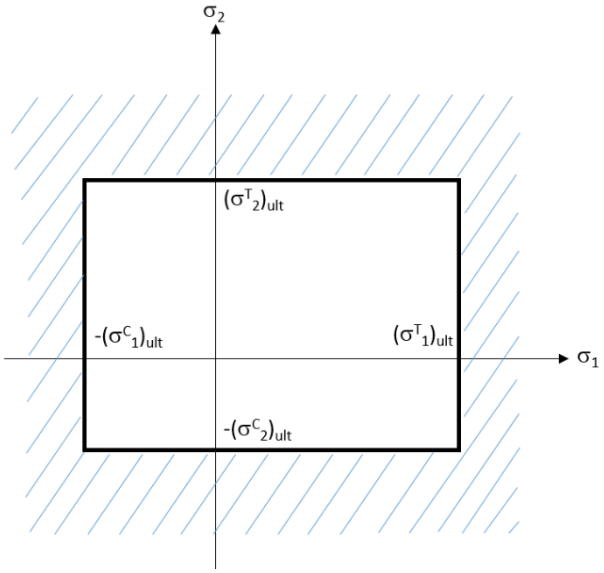

Figure 2.1: Safe and unsafe regions of the maximum stress criterion in two dimensions.

However, it overpredicts the strength, does not cover the interactions between the failure modes and does not fit well to the biaxial experimental data.

2.2.2 Tsai-Hill Criterion

Tsai-Hill criterion relates stress components in a single equation; thus it is an interactive criterion. For orthotropic materials, the criterion is as follows

$$\left(\frac{\sigma_1}{X_1}\right)^2 - \frac{\sigma_1\sigma_2}{X_2^2} + \left(\frac{\sigma_2}{Y}\right)^2 + \left(\frac{\tau_{12}}{(\tau_{12})_{ult}}\right)^2 + \left(\frac{\tau_{23}}{(\tau_{23})_{ult}}\right)^2 + \left(\frac{\tau_{13}}{(\tau_{13})_{ult}}\right)^2 < 1 \tag{2.7}$$

where

If $\sigma_1 > 0$, $\quad X_1 = (\sigma_1^T)_{ult}$

If $\sigma_1 < 0$, $\quad X_1 = (\sigma_1^C)_{ult}$

If $\sigma_2 > 0$, $\quad X_2 = (\sigma_1^T)_{ult}$, $\quad$ and $\quad Y = (\sigma_2^T)_{ult}$

If $\sigma_2 < 0$, $\quad X_2 = (\sigma_1^C)_{ult}$, $\quad$ and $\quad Y = (\sigma_2^C)_{ult}$

Strength ratio of the Tsai-Hill criterion is calculated by

$$SR = \frac{1}{\sqrt{\left(\frac{\sigma_1}{X_1}\right)^2 - \frac{\sigma_1\sigma_2}{X_2^2} + \left(\frac{\sigma_2}{Y}\right)^2 + \left(\frac{\tau_{12}}{(\tau_{12})_{ult}}\right)^2 + \left(\frac{\tau_{23}}{(\tau_{23})_{ult}}\right)^2 + \left(\frac{\tau_{13}}{(\tau_{13})_{ult}}\right)^2}} \tag{2.8}$$

The Tsai-Hill criterion is an conformation of the Von Mises' yield criterion to the composite laminates, proposed by Hill [69]. To have the form in Equation (2.7), the failure strength of Hill's theory is related to usual failure strengths by Tsai [70]. This criterion fits more accurately to the experimental results [4]. Due to its accuracy for all cases, its a broadly accepted. Nevertheless, since there is only one equation, Tsai-Hill criterion does not specify the mode of failure leading to the failure.

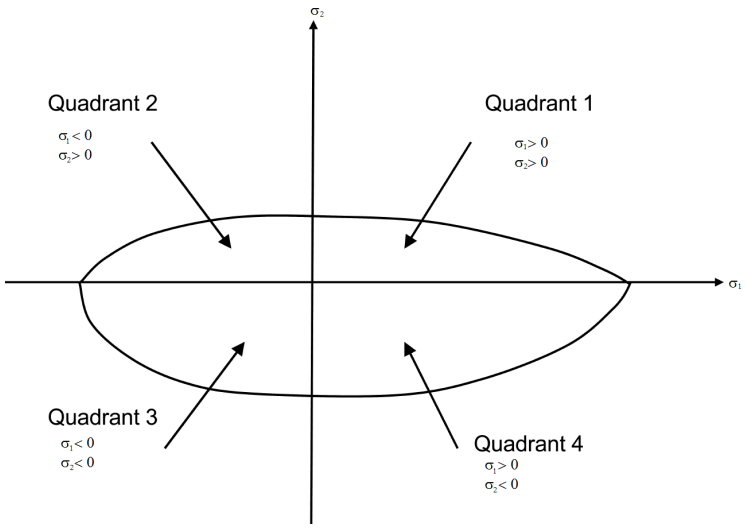

Figure 2.2: Failure envelope of Tsai-Hill Criterion [3].

2.2.3 Hoffman Criterion

Hoffman criterion is also modification of Hill's criterion [69], by adding linear terms [71]

$$\begin{aligned} &C_1(\sigma_2 - \sigma_3)^2 + C_2(\sigma_3 - \sigma_1)^2 + C_3(\sigma_1 - \sigma_2)^2 \\ &\qquad + C_4\sigma_1 + C_5\sigma_2 + C_6\sigma_3 + C_7\tau_{23}^2 + C_8\tau_{13}^2 + C_9\tau_{12}^2 < 1 \end{aligned} \tag{2.9}$$

where C_i, $i = 1,\ 2, ...,\ 9$ are experimentally determined strength parameters. Assuming $\sigma_3 = 0$, equation takes the form

$$\begin{aligned} C_1\sigma_2^2 + C_2\sigma_1^2 + C_3(\sigma_1 - \sigma_2)^2 \\ + C_4\sigma_1 + C_5\sigma_2 + C_7\tau_{23}^2 + C_8\tau_{13}^2 + C_9\tau_{12}^2 < 1 \end{aligned} \tag{2.10}$$

where coefficients are defined as

$$\begin{aligned} C_1 &= \frac{1}{2}\left(\frac{1}{(\sigma_2^T)_{ult}(\sigma_2^C)_{ult}} + \frac{1}{(\sigma_3^T)_{ult}(\sigma_3^C)_{ult}} - \frac{1}{(\sigma_1^T)_{ult}(\sigma_1^C)_{ult}}\right), \\ C_2 &= \frac{1}{2}\left(\frac{1}{(\sigma_1^T)_{ult}(\sigma_1^C)_{ult}} + \frac{1}{(\sigma_3^T)_{ult}(\sigma_3^C)_{ult}} - \frac{1}{(\sigma_2^T)_{ult}(\sigma_2^C)_{ult}}\right), \\ C_3 &= \frac{1}{2}\left(\frac{1}{(\sigma_1^T)_{ult}(\sigma_1^C)_{ult}} + \frac{1}{(\sigma_2^T)_{ult}(\sigma_2^C)_{ult}} - \frac{1}{(\sigma_3^T)_{ult}(\sigma_3^C)_{ult}}\right), \\ C_4 &= \frac{1}{(\sigma_1^T)_{ult}} - \frac{1}{(\sigma_1^C)_{ult}}, \\ C_5 &= \frac{1}{(\sigma_2^T)_{ult}} - \frac{1}{(\sigma_2^C)_{ult}}, \\ C_7 &= \frac{1}{(\tau_{23})_{ult}^2}, \\ C_8 &= \frac{1}{(\tau_{13})_{ult}^2}, \\ C_9 &= \frac{1}{(\tau_{12})_{ult}^2}. \end{aligned}$$

The strength ratio of the Hoffman criterion is found by quadratic equation. Which is equation of the form (2.11), has the solution as (2.12).

$$ax^2 + bx + c = 0 \tag{2.11}$$

$$x = \frac{-b \pm \sqrt{b^2 - 4ac}}{2a} \tag{2.12}$$

Thus, for the Hoffman theory, the coefficients are

$$a = C_1\sigma_2^2 + C_2\sigma_1^2 + C_3(\sigma_1 - \sigma_2)^2 + C_7\tau_{23} + C_8\tau_{13} + C_9\tau_{12} \tag{2.13}$$

$$b = C_4\sigma_1 + C_5\sigma_2 \tag{2.14}$$

$$c = -1 \tag{2.15}$$

The strength ratio of the Hoffman criterion is the positive result of 2.12 with coefficients 2.13.

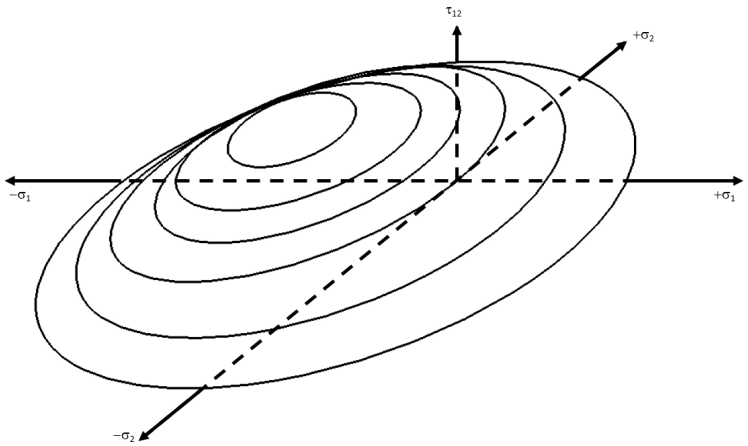

Figure 2.3: Failure envelope of Hoffman Criterion [4].

Hoffman's criterion indicates ellipsoids for plane stress in σ_1, σ_2 and τ_{12} space, symmetric about $\sigma_1 - \sigma_2$ plane [4], as shown in the Figure 2.3 Hoffman criterion also agrees with several experimental data [4, 70, 72]. Moreover, it allows using the same failure criteria for all quadrants of the ellipsoid, and does not take interactions of the different failure modes into account.

2.2.4 Tsai-Wu Criterion

Another interactive failure theory is Tsai-Wu criterion. The criterion developed by curve fitting to the experimental data by increasing the terms in the equation. This results also allows us eof strength tensors [73]. The most general form of the Tsai-Wu theory in six-dimensional stress space is

$$F_i\sigma_i + F_{ij}\sigma_{ij} = 1 \qquad i, j = 1, 2, ... 6. \tag{2.16}$$

where F_i and F_{ij} are strength tensors of the second and fourth rank [73]. An orthotropic lamina with $\sigma_3 = 0$ is considered not to be failed if

$$F_1\sigma_1 + F_2\sigma_2 + F_{11}\sigma_1^2 + F_{22}\sigma_2^2 + F_{66}\tau_{12}^2 + F_{44}\tau_{23}^2 + F_{55}\tau_{13}^2 + 2F_{12}\sigma_1\sigma_2 < 1 \tag{2.17}$$

where

$$F_1 = \frac{1}{(\sigma_1^T)_{ult}} - \frac{1}{(\sigma_1^C)_{ult}}, \qquad F_{11} = \frac{1}{(\sigma_1^T)_{ult}(\sigma_1^C)_{ult}},$$
$$F_2 = \frac{1}{(\sigma_2^T)_{ult}} - \frac{1}{(\sigma_2^C)_{ult}}, \qquad F_{22} = \frac{1}{(\sigma_2^T)_{ult}(\sigma_2^C)_{ult}},$$
$$F_{66} = \frac{1}{(\tau_{12})_{ult}^2}, \quad F_{44} = \frac{1}{(\tau_{23})_{ult}^2}, \quad F_{55} = \frac{1}{(\tau_{13})_{ult}^2},$$

F_{12} is interactive stress term, and require a biaxial tensile test [3]. Although obtaining F_{12} is difficult, empirical results can be used because its effect is minimal. For example [10],

$$F_{12} = -\frac{1}{(\sigma_1^T)_{ult}^2} \text{ from Tsai-Hill criterion [70] or,} \tag{2.18}$$

$$F_{12} = -\frac{1}{2(\sigma_1^T)_{ult}(\sigma_1^C)_{ult}} \text{ from Hoffman criterion [71] or,} \tag{2.19}$$

$$F_{12} = -\frac{1}{2}\sqrt{\frac{1}{(\sigma_1^T)_{ult}(\sigma_1^C)_{ult}(\sigma_2^T)_{ult}(\sigma_2^C)_{ult}}} \text{ from Mises-Hency criterion [74]} \tag{2.20}$$

To calculate the strength ratio of the criterion, again the Equation (2.12) should be solved with the corresponding coefficients

$$\begin{aligned} a &= F_{11}\sigma_1^2 + F_{22}\sigma_2^2 + F_{66}\tau_{12}^2 + F_{44}\tau_{23}^2 + F_{55}\tau_{13}^2 + 2F_{12}\sigma_1\sigma_2 \\ b &= F_1\sigma_1 + F_2\sigma_2 \\ c &= -1 \end{aligned} \tag{2.21}$$

The strength ratio of the Tsai-Wu criterion is the positive result of (2.12) with coefficients in (2.21).

Tsai-Wu criterion is generally the most compatible criterion with experimental results [3]. However, it does not give information about the failure mechanism leading to the failure [75].

2.2.5 Hashin Criteria

Hashin criteria is a partially interactive criteria, i.e., failure of fiber and matrix treated separately. Due to this feature, Hashin criteria distinguish among the various different

failure mode as well as detecting the failure [76]. This property makes the Hashin criteria more suitable for progressive failure analysis than the aforementioned criteria. The quadratic criteria for $\sigma_z = 0$ derived by Hashin is as follows [76]:

Tensile failure of fiber ($\sigma_1 > 0$)

$$\left(\frac{\sigma_1}{(\sigma_1^T)_{ult}}\right)^2 + \frac{\sigma_{12}^2 + \sigma_{13}^2}{(\tau_{12})_{ult}^2} < 1 \tag{2.22}$$

or

$$\sigma_1 = (\sigma_1^T)_{ult} \tag{2.23}$$

Compressive failure of fiber ($\sigma_1 < 0$)

$$\sigma_1 = -(\sigma_1^C)_{ult} \tag{2.24}$$

Tensile failure of matrix ($\sigma_2 > 0$)

$$\left(\frac{\sigma_2}{(\sigma_2^T)_{ult}}\right)^2 + \left(\frac{\sigma_{23}}{(\tau_{23})_{ult}}\right)^2 + \frac{\sigma_{12}^2 + \sigma_{13}^2}{(\tau_{12})_{ult}^2} < 1 \tag{2.25}$$

Compressive failure of fiber ($\sigma_2 < 0$)

$$\frac{\sigma_2}{(\sigma_2^C)_{ult}}\left[\left(\frac{(\sigma_2^C)_{ult}}{2(\tau_{23})_{ult}}\right)^2 - 1\right] + \left(\frac{\sigma_2}{2(\tau_{23})_{ult}}\right)^2 + \left(\frac{\tau_{23}}{(\tau_{23})_{ult}}\right)^2 + \frac{\tau_{12}^2 + \tau_{13}^2}{(\tau_{12})_{ult}^2} < 1 \tag{2.26}$$

The strength ratio of the Hashin criteria is calculated in a slightly difficult manner. It is composed of individual strength ratios of the criteria

$$\text{if} \quad \sigma_1 > 0, \quad SR_F = \frac{1}{\sqrt{A_1\sigma_1^2 + A_2(\tau_{12}^2 + \tau_{13}^2)}}$$

$$\text{if} \quad \sigma_1 < 0, \quad SR_F = -\frac{(\sigma_1^C)_{ult}}{\sigma_1}$$

$$\text{if} \quad \sigma_2 > 0, \quad SR_M = \frac{1}{\sqrt{A_3\sigma_2^2 + A_4\tau_{23}^2 + A_2(\tau_{12}^2 + \tau_{13}^2)}}$$

$$\text{if} \quad \sigma_2 < 0, \quad SR_M \text{ is the positive result of Equation (2.12) with coefficients}$$

$$a = \frac{A_4\sigma_2^2}{4} + A_4\tau_{23}^2 + A_2(\tau_{12}^2 + \tau_{13}^2) \tag{2.27}$$

$$b = A_5 \tag{2.28}$$

$$c = -1 \tag{2.29}$$

where,

$$A_1 = \frac{1}{(\sigma_1^T)_{ult}}, \quad A_2 = \frac{1}{(\tau_{12})_{ult}^2}$$
$$A_3 = \frac{1}{(\sigma_2^T)_{ult}}, \quad A_4 = \frac{1}{(\tau_{23})_{ult}^2}$$
$$A_5 = \frac{1}{(\sigma_2^C)_{ult}}\left[\left(\frac{(\sigma_1^T)_{ult}}{2(\tau_{23})_{ult}}\right)^2 - 1\right]$$

Lastly, the strength ratio is

$$SR = min(SR_F, SR_M) \tag{2.30}$$

CHAPTER 3

ISOGEOMETRIC ANALYSIS

The concept of isogeometric analysis (IGA) was first proposed by Hughes et al. in 2005 [7]. IGA is a relatively modern approach that uses NURBS (Non-Uniform Rational B-Splines) basis functions in analysis procedure. NURBS are also the splines used to represent the design model in CAD software. Therefore, using the same geometric data for design and analysis, IGA uses the exact geometry for analysis. Moreover, any refinement does not change the actual geometry and does not require dialogue with CAD [7]. Since than, the concept of IGA is implemented to many fields as explained in Section 1.2.

In this chapter, the fundamental concepts for isogeometric analysis, such as B-splines and NURBS, will be explained. Afterwards, usage of the NURBS as basis function for analysis will be discussed. Moreover, refinement techniques for the IGA will be covered. Lastly, the IGA will be compared with finite element analysis.

3.1 B-Splines

B-spline basis functions are piecewise polynomial functions defined on a set of parametric coordinates, namely knot vectors. The knot vector is represented as follows:

$$\Xi = \{\xi_1, \xi_2, \xi_3, ..., \xi_{n+p+1}\}, \tag{3.1}$$

where $\xi_i \in \mathbb{R}$ is i^{th} knot, $i = 1, .., n+p+1$ is the knot index, n is the number of basis functions to construct B-spline curve and p is the order of the polynomial. For the knot vector, $\xi_i \leq \xi_{i+1}$, meaning knots may be repetitive but cannot be in descending order. The knot vector splits the parameter space into intervals, as called knot spans.

These intervals have zero length for between repetitive knots. For the first and last knots with k times repetitions. The knot vector is called open if $k = p + 1$. The basis function built from open knot vectors are only interpolatory at the ends of the parameter space and at the corners of the multiple dimensions [1]. The knots can be aligned uniformly or non-uniformly in the knot vectors. The values of the knot vectors are usually normalized to [0,1].

For $p = 0$, B-spline basis function is defined piecewise as

$$N_{i,0}(\xi) = \begin{cases} 1 & \text{if } \xi_i \leq \xi < \xi_{i+1} \ , \\ 0 & \text{otherwise.} \end{cases} \tag{3.2}$$

and for $p > 0$ it is defined by

$$N_{i,\,p}(\xi) = \frac{\xi - \xi_i}{\xi_{i+p} - \xi_i} N_{i,\,p-1}(\xi) + \frac{\xi_{i+p+1} - \xi}{\xi_{i+p+1} - \xi_{i+1}} N_{i+1,\,p-1}(\xi) \tag{3.3}$$

As can be seen from Equation (3.3), the i^{th} B-spline function of degree p is defined recursively by the Cox-de Boor recursive formula [77, 78]. This formula applied with the convention of fraction with zero denominator equals to zero. The dependencies of basis functions of B-spline function with $p = 3$ in this recursive algorithm is illustrated for first 3 knots in Figure 3.1. Given a knot vector $\Xi = \{0, 0.25, 0.5, 0.75, 1\}$ basis functions of order 0, 1, 2 and 3 is shown in the Figure 3.2. The zeroth and first order basis functions are identical to the shape functions of isoparametric FEM of the same order. B-spline functions differ from FEM functions for 2 and higher orders [7].

3.1.1 Properties of B-Spline Basis Functions

Some properties of the B-spline basis functions are as follows:

- Basis functions constitute a partition of unity.

$$\sum_{i=1}^{n} N_{i,\,p}(\xi) = 1, \quad \forall \xi.$$

- Each basis function is non-negative over the entire domain.

$$N_{i,\,p}(\xi) \geq 0, \quad \forall \xi.$$

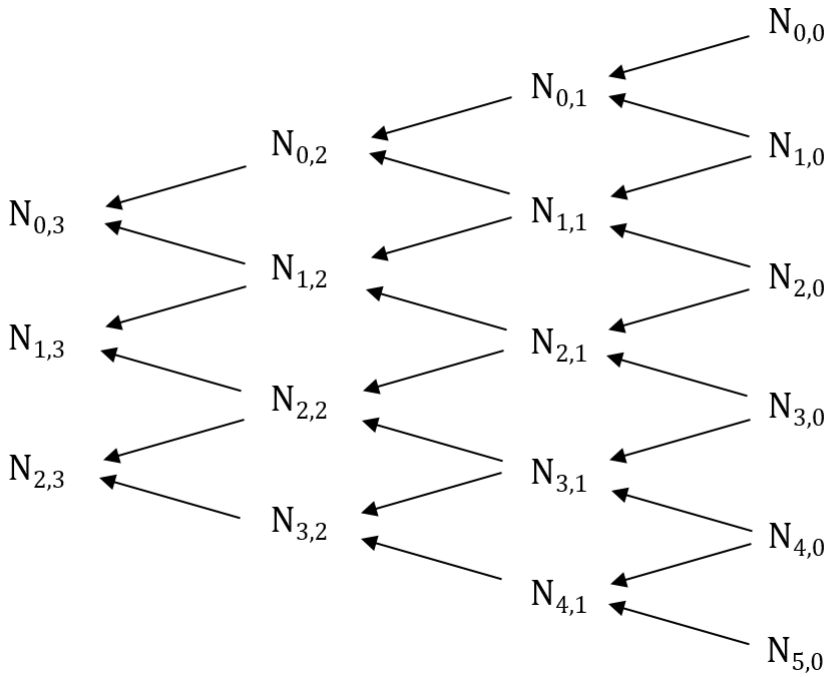

Figure 3.1: The dependencies of B-spline basis functions ($p = 3$) for i=1, 2, 3 [5].

- B-spline function of order p has $p - k$ continuous derivatives on a knot with multiplicity of k. If the knot is not repetitive, $k = 1$.
- B-spline function of order p has support of $p+1$ knot spans. That is, $N_{i,\,p}(\xi) > 0$ over $[\xi_i,\, \xi_{i+p+1}]$.
- Basis functions are generally approximating the control points. However, it is interpolatory when a knot value is repeated $k = p$, and the basis is discontinuous if $k = p + 1$.

3.1.2 Derivatives of B-Spline Basis Functions

Because of the recursive nature of the B-spline basis functions, their derivatives also require computation of the derivatives of lower order basis functions. For polynomial of order p and knot vector Ξ, the first derivative of the i^{th} basis function with respect to parametric coordinate ξ, is calculated as indicated below

$$\frac{d}{d\xi}N_{i,\,p}(\xi) = \frac{p}{\xi_{i+p} - \xi_i}N_{i,\,p-1}(\xi) - \frac{p}{\xi_{i+p+1} - \xi_{i+1}}N_{i+1,\,p-1}(\xi) \tag{3.4}$$

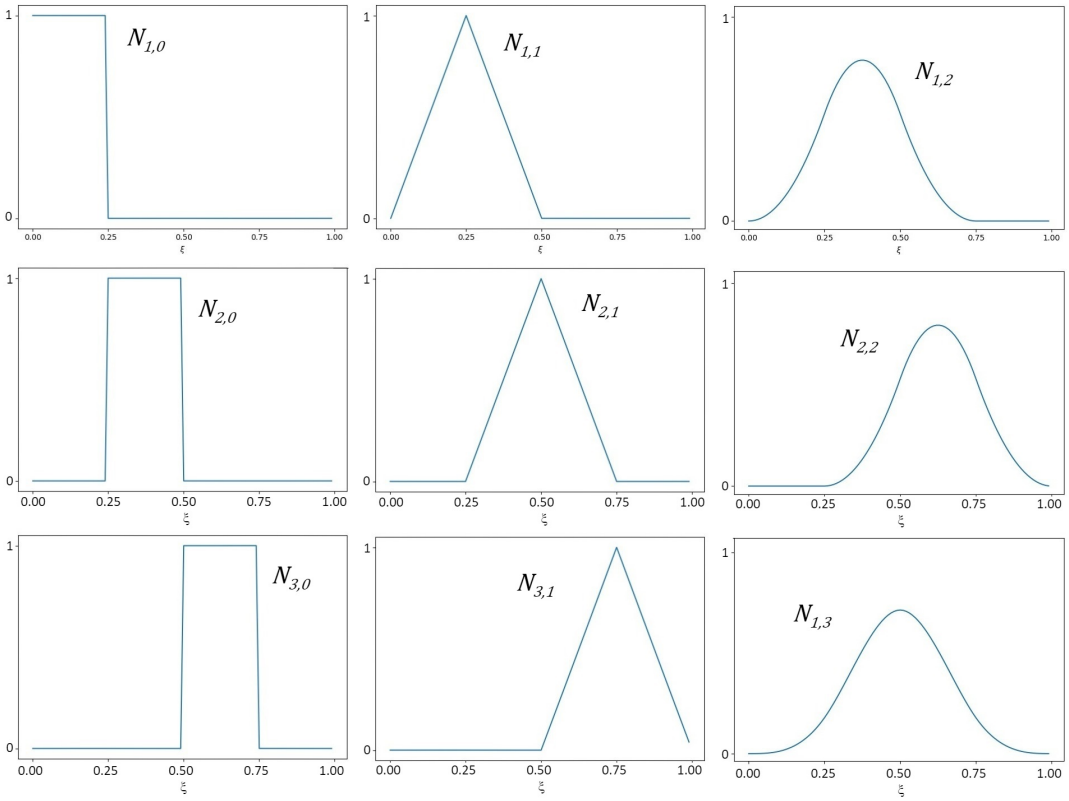

Figure 3.2: Basis functions of order 0, 1, 2, and 3 for uniform knot vector $\Xi = \{0, 0.25, 0.5, 0.75, 1\}$.

Differentiating the Equation (3.4), a generalized expression for k^{th} order derivative is obtained as

$$\begin{aligned}\frac{d^k}{d^k\xi}\, N_{i,\,p}(\xi) = &\frac{p}{\xi_{i+p} - \xi_i}\left(\frac{d^{k-1}}{d^{k-1}\xi}\, N_{i,\,p-1}(\xi)\right) \\ &- \frac{p}{\xi_{i+p+1} - \xi_{i+1}}\left(\frac{d^{k-1}}{d^{k-1}\xi}\, N_{i+1,\,p-1}(\xi)\right)\end{aligned} \tag{3.5}$$

The expansion of Equation (3.5) by means of (3.4) gives series of functions in lower orders $N_{i,p-k}$, $N_{i+1,p-k}$,..., $N_{i+k,p-k}$. That is

$$\frac{d^k}{d^k\xi}\, N_{i,\,p}(\xi) = \frac{p!}{(p-k)!}\sum_{j=0}^{k} a_{k,j} N_{i+j,\,p-k}(\xi) \tag{3.6}$$

where

$$
\begin{aligned}
a_{0,0} &= 1, \\
a_{k,0} &= \frac{a_{k-1,0}}{\xi_{i+p-k+1} - \xi_i}, \\
a_{k,j} &= \frac{a_{k-1,j} - a_{k-1,j-1}}{\xi_{i+p+j-k+1} - \xi_{i+j}} \qquad j = 1, ..., k-1, \\
a_{k,k} &= \frac{-a_{k-1,k-1}}{\xi_{i+p+1} - \xi_{i+k}}.
\end{aligned}
$$

3.1.3 B-Spline Geometries

In this section, construction of 1-D, 2-D and 3-D geometries by use of B-splines will be explained.

3.1.3.1 B-Spline Curves

In a d dimensional space, B-spline curves are formed in $\mathbb{R}^d$ by linearly combined B-spline basis functions with the vector-valued coefficients, known as control points. Generally, B-spline curves do not interpolate these control points. The piecewise linear interpolation of control points is named as control polygon. For a polynomial order p, given n basis functions $N_{i,p}$, and reciprocal control points $P_i \in \mathbb{R}^d$ where $i = 1, 2, ..., n$, B-spline curve is defined as

$$C(\xi) = \sum_{i=1}^{n} N_{i,p}(\xi) P_i \tag{3.7}$$

For knot vectors $\Xi_{p=2} = \{0, 0, 0, 0.2, 0.4, 0.4, 0.6, 0.8, 1, 1, 1\}$, $\Xi_{p=2} = \{0, 0, 0, 0.2, 0.4, 0.6, 0.8, 1, 1, 1\}$ and $\Xi_{p=3} = \{0, 0, 0, 0, 0.2, 0.4, 0.6, 0.8, 1, 1, 1, 1\}$ with control points tabulated in Table 3.1, B-spline curves at Figures 3.3a and 3.3b are constructed for quadratic and the curve at Figure 3.3c is constructed for cubic polynomials. The green points in the figures indicates the control points and the polygons of red lines demonstrate the control polygons. As can be seen both curves interpolate only at the start and the end points since both knot vectors are open. However, the curve at Figure 3.3a also interpolates at knot $\xi = 0.4$ since the number of repetition, k, of the corresponding knot is equal to the order, p. The effect of repeated knot is also seen at continuous derivatives of the curves. The B-spline curves are C^{p-1} continues

everywhere except the repeated knots. Therefore, the curves in the Figures 3.3b and 3.3c are $C^{2-1} = C^1$ and $C^{3-1} = C^2$ continuous, respectively. Whereas, the curve in the Figure 3.3a is $C^{2-1} = C^1$ continues except $\xi = 0.4$. At this knot the curve is $C^{p-k} = C^{2-2} = C^0$ continues. Also, it can be seen from Figures 3.3b and 3.3c that the curve becomes more approximating to the control net and the individual effect of the control points reduces with the increasing order.

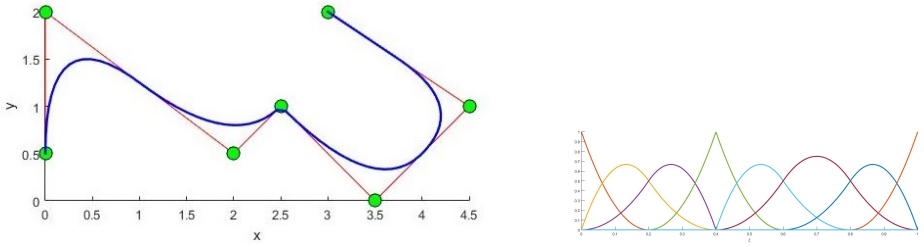

(a)

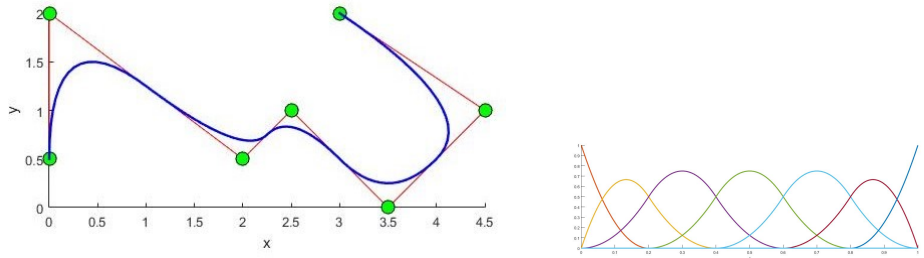

(b)

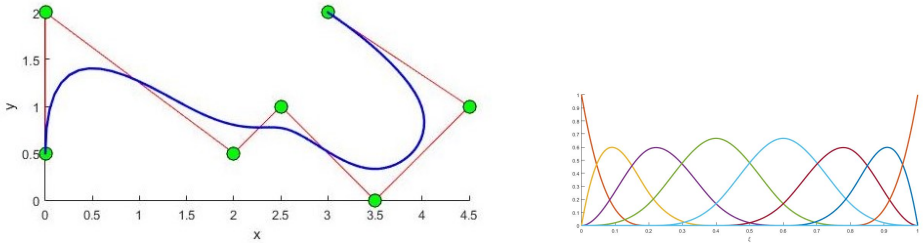

(c)

Figure 3.3: B-spline curves with control points in Table 3.1 and constructing basis functions. (a) $\Xi_{p=2} = \{0, 0, 0, 0.2,\ 0.4, 0.4, 0.6, 0.8, 1, 1, 1\}$, (b) $\Xi_{p=2} = \{0, 0, 0, 0.2, 0.4, 0.6, 0.8, 1, 1, 1\}$ and (c) $\Xi_{p=3} = \{0, 0, 0, 0,\ 0.2, 0.4, 0.6, 0.8, 1, 1, 1, 1\}$ in $\mathbb{R}^2$.

B-spline curves allow local control due to compact support of the B-spline basis func-

Table 3.1: Coordinates of control points of Figure 3.3.

P_i	1	2	3	4	5	6	7
x	0	0	2	2.5	3.5	4.5	3
y	0.5	2	0.5	1	0	1	2

tions. That is, if one of the control points is moved, only $p + 1$ elements of the curve are affected. Moreover, B-spline curves have convex hull property, i.e., the convex hull defined by the control points involves the B-spline curve.

3.1.3.2 B-Spline Surfaces

The B-spline surface is obtained by tensor product of B-spline basis functions in two parametric directions with a given bidirectional control net, $P_{i,j}$, where $i = 1, 2, ..., n$ and $j = 1, 2, ..., m$. For polynomial orders p and q, the knot vector in ξ direction $\Xi = \{\xi_1, \xi_2, ..., \xi_{n+p+1}\}$, in η direction $\mathcal{H} = \{\eta_1, \eta_2, ...\eta_{m+q+1}\}$ and control net $P_{i,j}$, B-spline surface is defined as

$$S(\xi, \eta) = \sum_{i=1}^{n} \sum_{j=1}^{m} N_{i,p}(\xi) M_{j,q}(\eta) P_{i,j} \tag{3.8}$$

where $N_{i,p}(\xi)$ is the univariate basis function of order p of the knot vector Ξ, and $M_{j,q}(\eta)$ is the univariate basis function of order q of the knot vector $\mathcal{H}$. An example of B-spline surface of cubic polynomials ($p = 3$, $q = 3$) with knot vectors $\Xi = \{0, 0, 0, 0, 0.125, 0.25, 0.375, 0.5, 0.75, 1, 1, 1, 1\}$ and $\mathcal{H} = \{0, 0, 0, 0, 0.5, 1, 1, 1, 1\}$ is given in Figure 3.4, and the basis functions creating this surface are shown in Figure 3.5.

B-spline surfaces have partition of unity property, likewise basis functions.

$$\sum_{i=1}^{n} \sum_{j=1}^{m} N_{i,p}(\xi) M_{j,q}(\eta) = \left(\sum_{i=1}^{n} N_{i,p}(\xi) \right) \left(\sum_{j=1}^{m} M_{j,q}(\eta) \right) = 1 \tag{3.9}$$

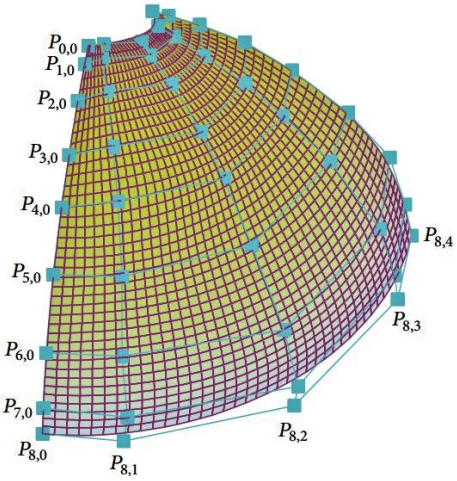

Figure 3.4: B-spline surface and control net [6].

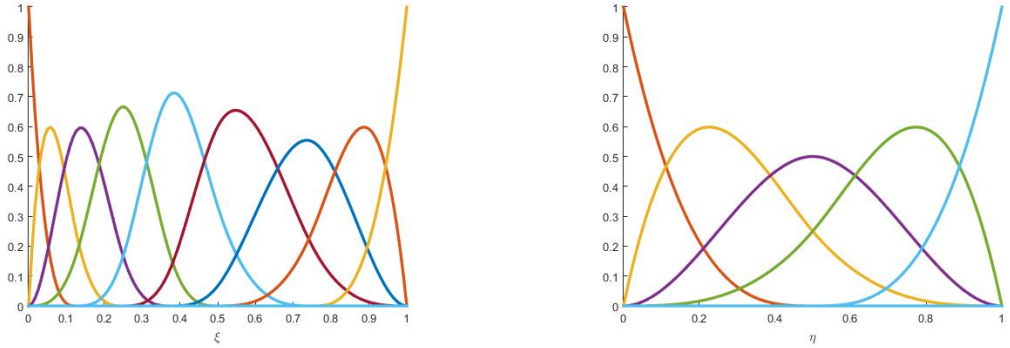

(a) (b)

Figure 3.5: Basis functions of the surface in Figure 3.4 (a) in ξ direction,(b) in η direction

3.1.3.3 B-Spline Solids

The B-spline solids are constructed in a similar manner to the B-spline surfaces. This time, instead of a bidirectional control net, a tri-directional control net $P_{i,j,k}$, $k = 1, 2, ..., l$ is required. For polynomial orders p, q and r, the knot vector in ξ direction $\Xi = \{\xi_1, \xi_2, ..., \xi_{n+p+1}\}$, in η direction $\mathcal{H} = \{\eta_1, \eta_2, ...\eta_{m+q+1}\}$, in ζ direction $\mathcal{Z} = \{\zeta_1, \zeta_2, ...\zeta_{l+r+1}\}$, and control net $P_{i,j,k}$, B-spline solid is defined as

$$S(\xi,\, \eta,\, \zeta) = \sum_{i=1}^{n} \sum_{j=1}^{m} \sum_{k=1}^{l} N_{i,\,p}(\xi) M_{j,\,q}(\eta) L_{k,\,r}(\zeta) P_{i,\,j,\,k} \tag{3.10}$$

where $N_{i,p}(\xi)$ is the univariate basis function of order p of the knot vector Ξ, $M_{j,q}(\eta)$ is the univariate basis function of order q of the knot vector $\mathcal{H}$, $L_{k,r}(\zeta)$ is the univariate basis function of order r of the knot vector $\mathcal{Z}$. A of B-spline solid is illustrated in Figure 3.6.

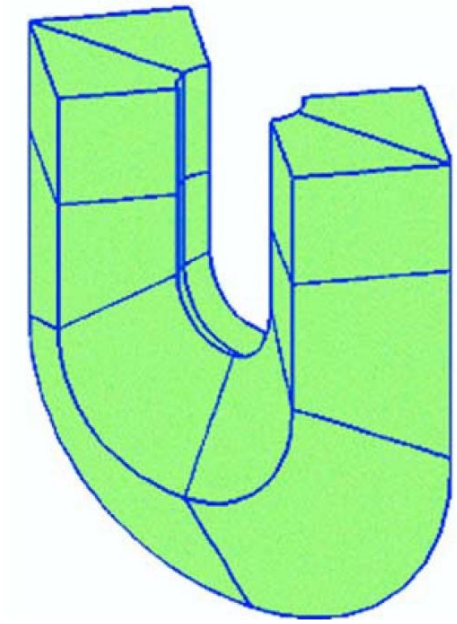

Figure 3.6: A B-spline solid [7].

3.1.4 Refinement

As in FEM, refinement techniques are available in the IGA. Analogous to h-refinement and p-refinement in the FEM, there are knot insertion and order elevation methods in the IGA. Furthermore, there is also an extra refinement procedure called k-refinement, which has no equivalent in the FEM. The geometry does not change in refinements since it is already exact.

3.1.4.1 Knot Insertion

The knot insertion procedure is enriching the basis by inserting the new knots. The new knot values may be new or an already existing. If an already existing knot is inserted, continuity of the basis decreases. Repeating a knot p times causes disconti-

nuity of the curve. For a knot vector $\Xi = \{\xi_1, \xi_2, ..., \xi_{n+p+1}\}$, insertion of a new knot $\bar{\xi}$ after k^{th} knot ξ_k, leads a new modified knot vector $\bar{\Xi} = \{\xi_1, \xi_2, ...\xi_k, \bar{\xi}, \xi_{k+1}...\xi_{n+p+1}\}$. Also the new control points are formed according to the Equation (3.11)

$$\bar{P}_i = \alpha_i P_i + (1 - \alpha_i) P_{i-1} \tag{3.11}$$

where

$$\alpha_i = \begin{cases} 1 & \text{if } 1 \leq i \leq k - p \ , \\ \frac{\bar{\xi} - \xi_i}{\xi_{i+p} - \xi_i} & \text{if } k - p \leq i \leq k \ , \\ 0 & \text{if } k + 1 \leq i \leq n + p + 2 \ . \end{cases}$$

An example of knot insertion can be seen in Figure 3.7, squares indicating the control points and knots denoted by circles [1].

Table 3.2: Control point coordinates of Figure 3.7a.

P_i	1	2	3
x	0	1	2
y	0.5	2	0

Table 3.3: Control point coordinates of Figure 3.7b.

$\bar{P}_i$	1	2	3	4
x	0	0.5	1.5	2
y	0.5	1.25	1	0

3.1.4.2 Order Elevation

The order elevation procedure is enriching the basis by rising the order of the polynomials of the basis functions. For order elevation, curve is divided into Bézier curves by knot insertion, because of the reason explained in Section 3.1.1, as the order increases, multicipality of the knot k should be increased for each unique knot as well, to preserve the continuity [7]. After this knot insertion process, polynomial orders are increased for every Bézier curve, then by removing the extra knots, curves are

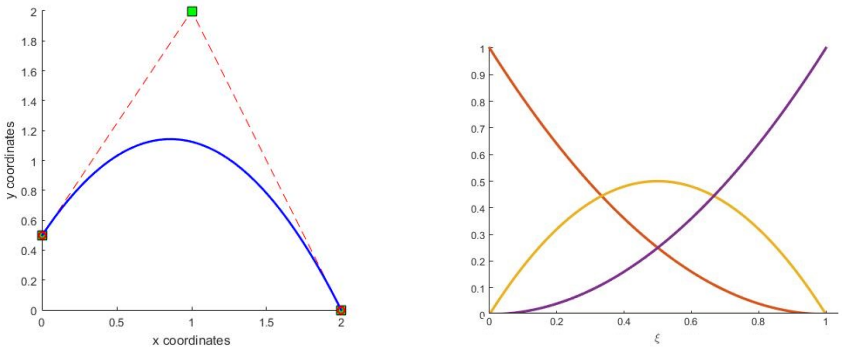

(a)

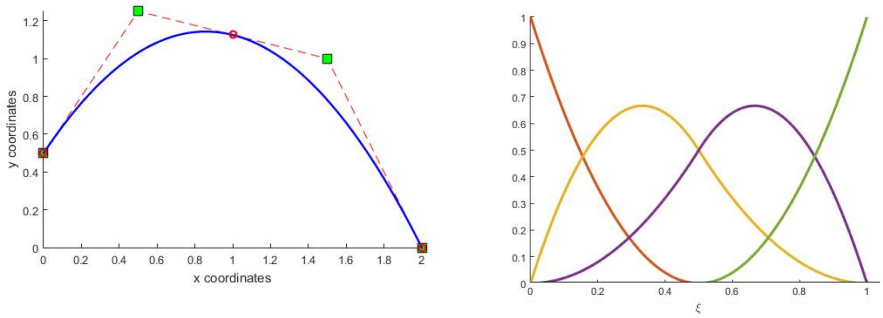

(b)

Figure 3.7: Quadratic B-spline curve and constructing basis functions (a) $\Xi_{p=2} = \{0, 0, 0, 1, 1, 1\}$ and control points in Table 3.1, (b) $\bar{\Xi}_{p=2} = \{0, 0, 0, 0.5, 1, 1, 1\}$ and control points in Table 3.3.

recombined. There are several algorithms for order elevation explained in [5]. To illustrate the order elevation procedure, an example is provided for a single segment curve in Figure 3.8 [1].

3.1.4.3 k-Refinement

The k-refinement procedure is a different order elevation technique, unique to spline basis. For increasing the order, k-refinement takes advantage of previously mentioned refinements independence from each other. The procedure of the k-refinement is as follows: given a curve of order p, fist order of the curve is increased to q then, a unique knot $\bar{\xi}$ is inserted to the knot vector. Continuity at new inserted knot will be C^{q-1}.

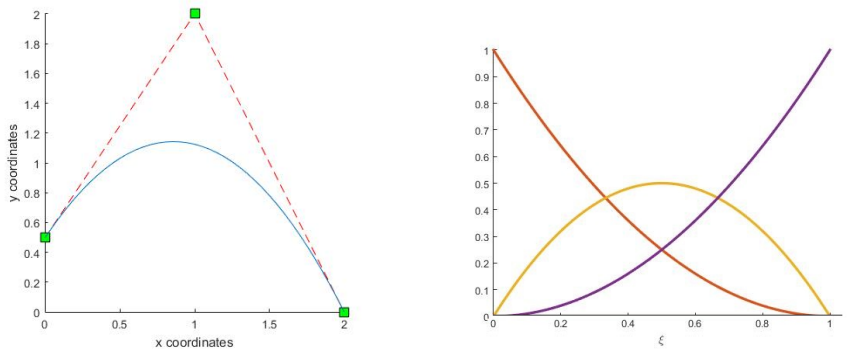

(a)

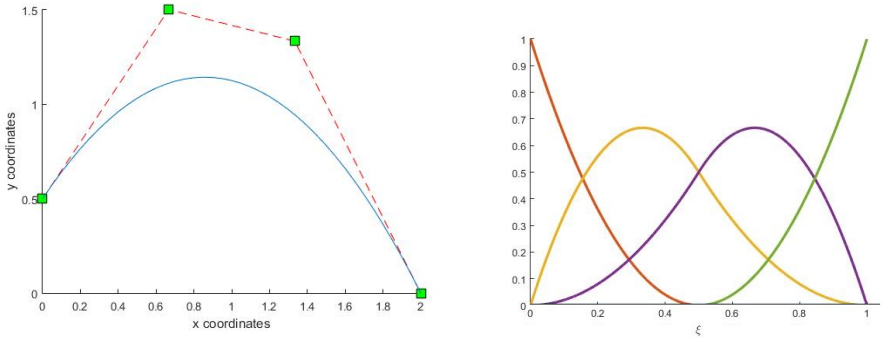

(b)

Figure 3.8: B-spline curve and constructing basis functions (a) $\Xi_{p=2} = \{0, 0, 0, 1, 1, 1\}$. (b) $\Xi_{p=3} = \{0, 0, 0, 0, 1, 1, 1, 1\}$.

Moreover, computational cost becomes significantly low compared to p-refinement which involves first knot insertion, then order elevation due to significant decrease in the number of final basis functions.

k-refinement is shown in the Figure 3.9 [7]. The order of the 3.9a is $p = 1$ and has $p + 1 = 2$ basis functions, then, in the left hand side, p-refinement applied by knot insertion, until there are $n - p$ elements. Then, order increased. In this method, every unique knot is repeated and basis functions are added to every element to maintain the continuity. If the order elevated r times, the number of basis functions would be $(r + 1)n - rp$. In k-refinement on the right hand side, first order elevated, and one basis functions added. Afterwards, again knots are inserted until having $n - p$ elements. For order elevated r times, there would be $r + p - 1$ continuous, $n + r$ basis

functions.

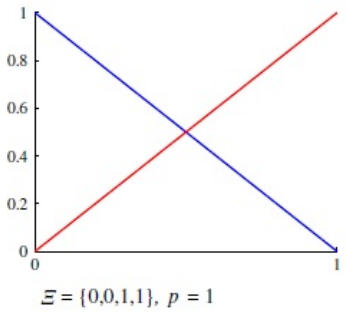

(a)

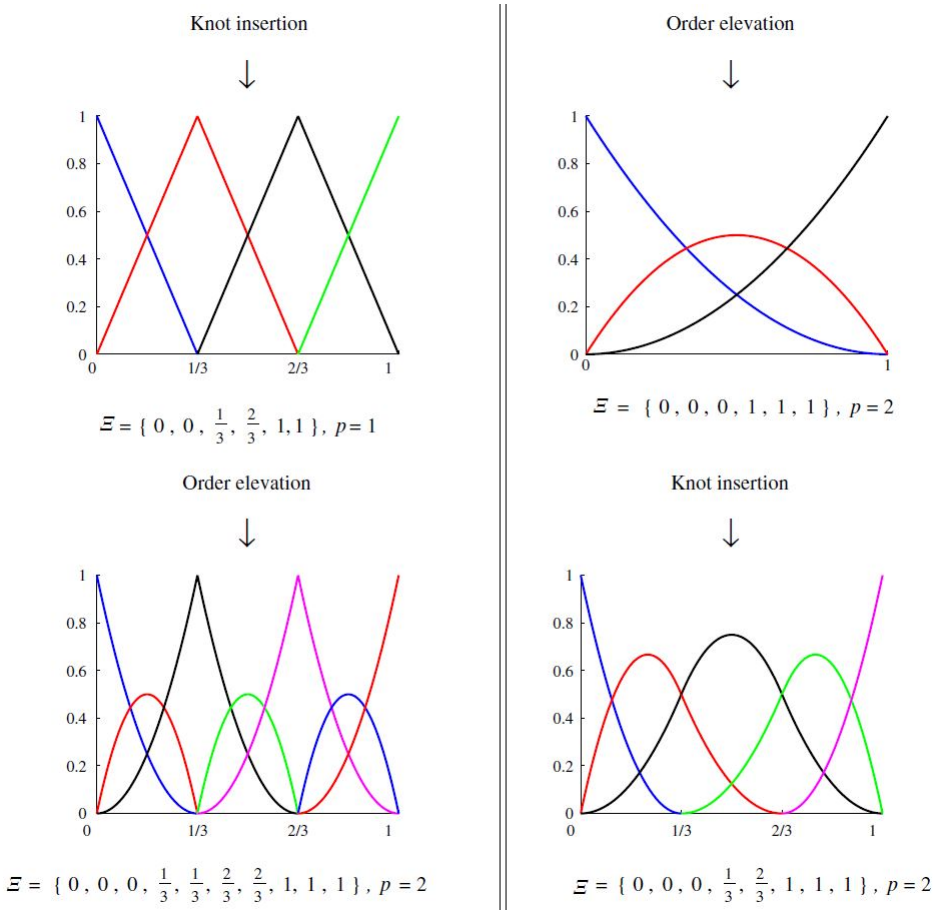

(b)

Figure 3.9: Comparison of the p- and k- refinements [7]. (a) Linear B-spline basis functions. (b) Left hand side, procedure of p-refinement; right hand side, procedure of k-refinement.

3.2 Non-uniform Rational B-Splines

Although B-splines effectively represents many geometries, they remain incapable of exactly representing conic curves. To express a conic curve, ratio of two functions is required. This type of functions called rational functions. Geometrically, Non-uniform Rational B-splines are projective transformation of B-spline entities to a one dimension lower space as illustrated in Figure 3.10 [1].

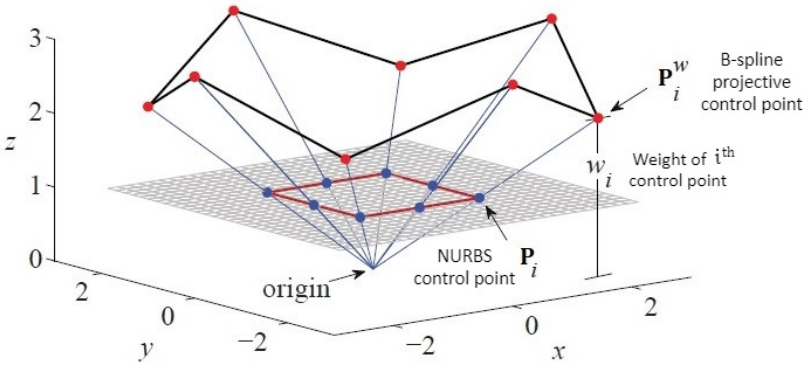

(a) Control polygons

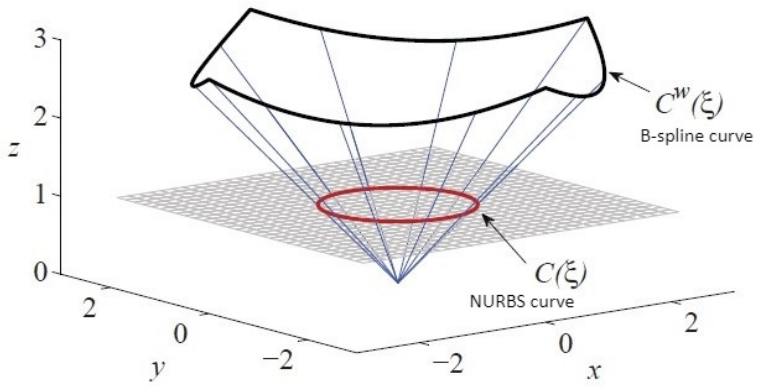

(b) Curves

Figure 3.10: The projective relation between B-spline and NURBS curves [1].

NURBS basis functions constitute of B-spline basis functions, weighting function and positive weight.

$$R_i^p(\xi) = \frac{N_{i,p}(\xi) w_i}{W(\xi)} \tag{3.12}$$

where $N_{i,p}(\xi)$ is the B-spline basis function, w_i is the i_{th} weight and $W(\xi)$ is the weighing function defined as follows

$$W(\xi) = \sum_{i=1}^{n} N_{i,p}(\xi) w_i \tag{3.13}$$

3.2.1 Properties of NURBS Basis Functions

Some properties of NURBS basis functions are as follows:

- NURBS basis functions are superset of B-spline basis functions; therefore, they have many common properties like partition of unity, non-negativity, local support, continuity of the funtions and their derivatives. If all the weights are equal, NURBS basis function is identical to the B-spline basis function.
- NURBS basis functions are rational functions.

3.2.2 Derivatives of NURBS Basis Functions

The derivative of a NURBS basis functions is taken using the chain rule and the derivative of the B-spline basis function yielding

$$\frac{d}{d\xi} R_{i,p}(\xi) = w_i \frac{W(\xi) N'_{i,p} - W'(\xi) N_{i,p}}{(W(\xi))^2} \tag{3.14}$$

where "$'$" means the first derivative with respect to ξ and the derivative of the weighting function is

$$W'(\xi) = \sum_{\hat{i}=1}^{n} N'_{\hat{i},p}(\xi) w_{\hat{i}} \tag{3.15}$$

For higher order derivatives

$$\frac{d^k}{d\xi^k} R_{i,p}(\xi) = \frac{A_i^{(k)}(\xi) - \sum_{j=1}^{k} \binom{k}{j} W^{(j)}(\xi) \frac{d^{(k-j)}}{d\xi^{(k-j)}} R_{i,p}(\xi)}{W(\xi)} \tag{3.16}$$

where

$$W^{(k)}(\xi) = \frac{d^k}{d\xi^k} W(\xi) \tag{3.17}$$

and

$$A_i^{(k)}(\xi) = w_i \frac{d^k}{d\xi^k} N_{i,p}(\xi) \tag{3.18}$$

Note that summation convention does not apply to the repeated index i, for Equation (3.18).

3.2.3 NURBS Geometries

A NURBS curve defined in terms of rational basis functions as

$$C(\xi) = \sum_{i=1}^{n} R_{i,p}(\xi) P_i \tag{3.19}$$

A circle formed by NURBS basis functions with knot vector $\Xi = \{0, 0, 0, 0.25, 0.25, 0.5, 0.5, 0.75, 0.75, 1, 1, 1\}$, control points and weights in Table 3.4 is shown in Figure 3.11. The rational basis function to construct a NURBS surface is defined as following

$$R_{i,j}^{p,q}(\xi, \eta) = \frac{N_{i,p}(\xi) M_{j,q}(\eta) w_{i,j}}{\sum_{\hat{i}=1}^{n} \sum_{\hat{j}=1}^{m} N_{\hat{i},p}(\xi) M_{\hat{j},q}(\eta) w_{\hat{i},\hat{j}}} \tag{3.20}$$

Then, the NURBS surface is

$$S(\xi,\, \eta) = \sum_{i=1}^{n} \sum_{j=1}^{m} R_{i,j}^{p,q}(\xi, \eta) P_{i,j} \tag{3.21}$$

Similarly, the rational basis function to construct a NURBS solid is

$$R_{i,j,k}^{p,q,r}(\xi, \eta, \zeta) = \frac{N_{i,p}(\xi) M_{j,q} L_{k,r}(\zeta) w_{i,j,k}}{\sum_{\hat{i}=1}^{n} \sum_{\hat{j}=1}^{m} \sum_{\hat{k}=1}^{l} N_{\hat{i},p}(\xi) M_{\hat{j},q}(\eta) L_{\hat{k},r}(\zeta) w_{\hat{i},\hat{j},\hat{k}}} \tag{3.22}$$

Lastly, the NURBS solid,

$$S(\xi,\, \eta,\, \zeta) = \sum_{i=1}^{n} \sum_{j=1}^{m} \sum_{k=1}^{l} R_{i,j,k}^{p,q,r}(\xi, \eta, \zeta) P_{i,j,k} \tag{3.23}$$

3.3 Analysis using NURBS based IGA

In this section, different spaces in isogeometric concept will be explained and formulations for using NURBS functions as an analysis tool will be derived.

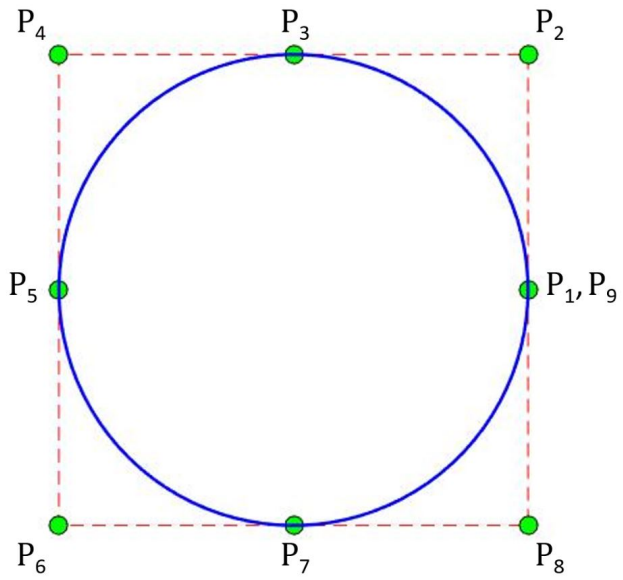

Figure 3.11: A circle formed by quadratic NURBS basis functions ($p = 2$) with knot vector $\Xi = \{0, 0, 0, 0.25, 0.25, 0.5, 0.5, 0.75, 0.75, 1, 1, 1\}$, control points and weights in Table 3.4.

Table 3.4: Coordinates and weights of control points of Figure 3.11.

P_i	1	2	3	4	5	6	7	8	9
x	1	1	0	-1	-1	-1	0	1	1
y	0	1	1	1	0	-1	-1	-1	0
w_i	1	$\frac{1}{\sqrt{2}}$	1	$\frac{1}{\sqrt{2}}$	1	$\frac{1}{\sqrt{2}}$	1	$\frac{1}{\sqrt{2}}$	1

3.3.1 Spaces and Mappings

There are four spaces in IGA. They are index space, parameter space, parent space and physical space. The relation and differences between the spaces is shown schematically in the Figure 3.12 successfully [1].

3.3.1.1 Index Space

Index space is constituted by dividing the space into number of knots in a knot vector without considering their values. In other words, repeating knots have different coor-

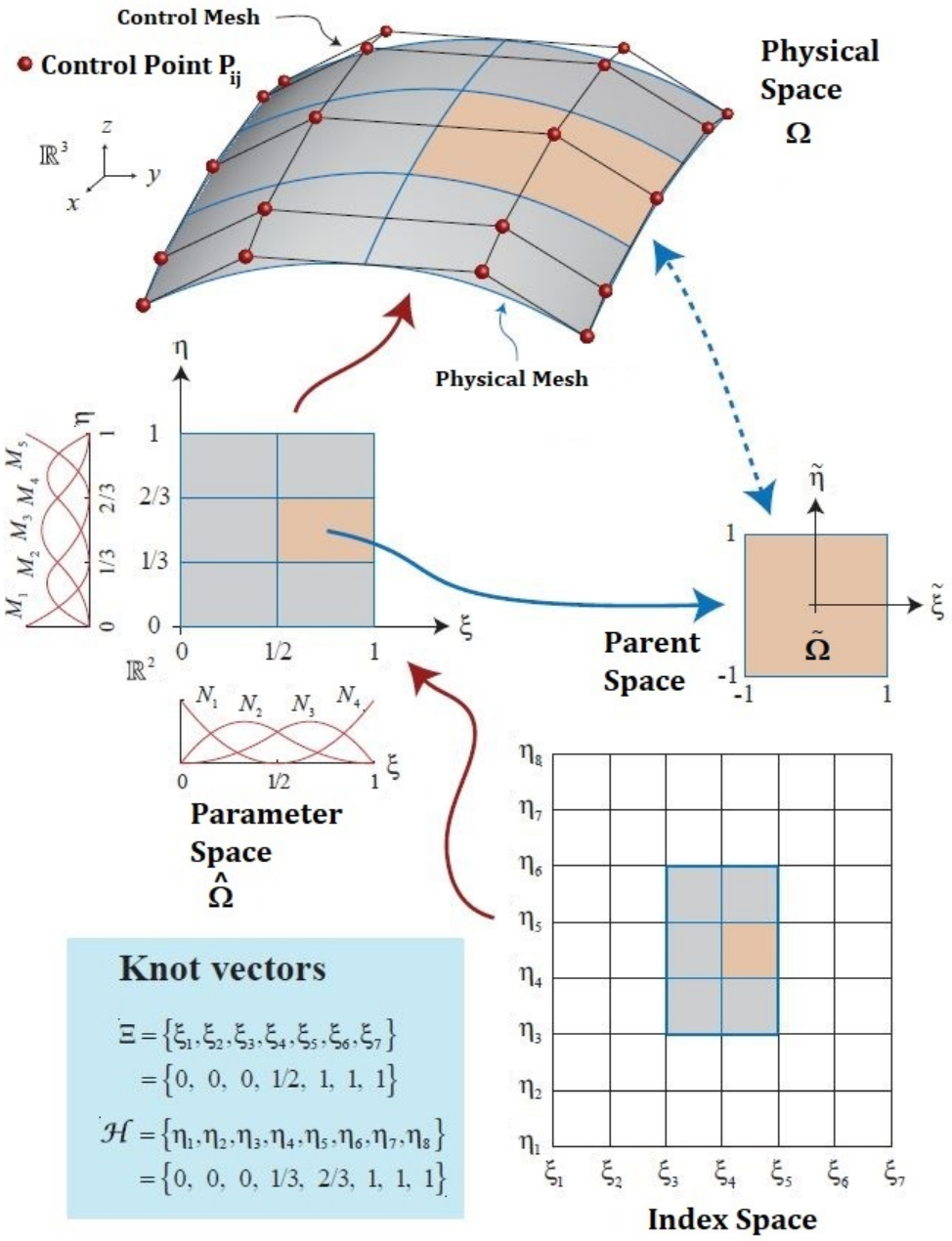

Figure 3.12: Schematic of relations of the relevant spaces [1].

dinates in the index space. To illustrate, for the knot vectors $\Xi = \{0, 0, 0, 0.5, 1, 1, 1\}$ and $\mathcal{H} = \{0, 0, 1, 1\}$ the index space is shown in the Figure 3.13.

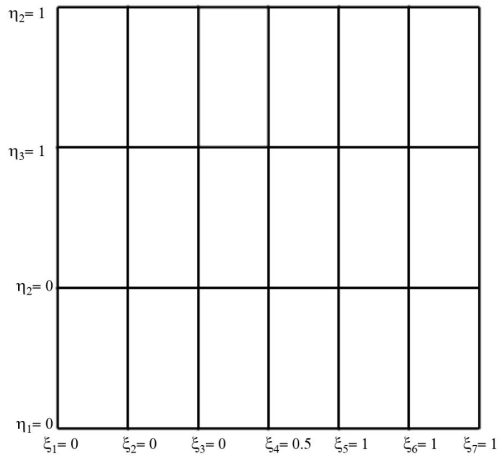

Figure 3.13: Representation of the knot vectors $\Xi = \{0, 0, 0, 0.5, 1, 1, 1\}$ and $\mathcal{H} = \{0, 0, 1, 1\}$ in index space.

3.3.1.2 Parameter Space

Parameter space is a more commonly used subspace of index space. It is obtained by omitting the repeating knots and expressing the modified knot vectors with non-zero knot spans. For a normalized knot vector, i.e., $\xi \in [0, 1]$, parameter space in 2-D is a unit square. The parameter space is indicated by $\hat{\Omega}$. Coordinates of the parameter space are (ξ, η, ζ). An example of the parameter space is provided in the Figure 3.14 for the knot vectors in Figure 3.13. In addition, the knot lines of the parameter space forms the region where elements located [8]. Unlike the parent and physical spaces, the parameter space is the result of using NURBS bases, and does not appear in formulations of conventional finite element method [8].

3.3.1.3 Parent Space

Parent space is where numerical integration, like Gaussian quadrature, performed. It is defined for each knot span. Limits of the parent space is -1 to 1 in every dimension of the problem, its a square for a 2-D problem and a cube for a 3-D problem. Parent space is denoted by $\tilde{\Omega}$ and its coordinates are $(\tilde{\xi}, \tilde{\eta}, \tilde{\zeta})$.

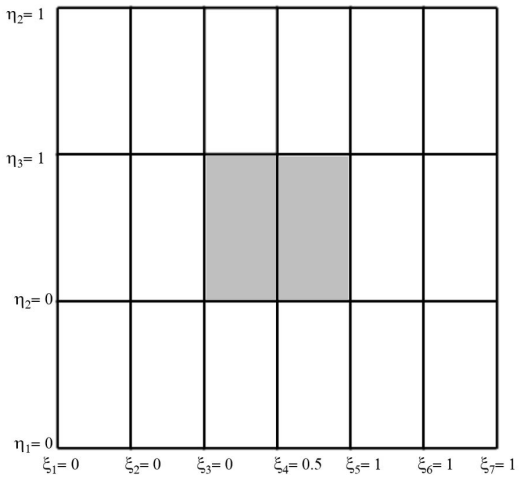

Figure 3.14: Shaded area represents the knot vectors $\Xi = \{0, 0, 0, 0.5, 1, 1, 1\}$ and $\mathcal{H} = \{0, 0, 1, 1\}$ in parameter space.

3.3.1.4 Physical Space

The physical space is representation of the actual geometry by basis functions. When its divided to form the elements, its named as physical mesh. Elements are knot spans for a single patch. Physical space is denoted by Ω, and its coordinates are (x, y, z).

3.3.1.5 Mappings Between the Spaces

All points have equivalence in all the spaces. The spaces serve different purposes. Therefore, transformations between the spaces are required. The transformation procedure is named as mapping. Mappings of an element in parent to parameter space ϕ^e and from parameter to physical space $\mathbf{x}^e$ are shown diagrammatically in Figure 3.15 [8]. Numerically, the mapping of a point $(\tilde{\xi}, \tilde{\eta})$ in the parent space to the parameter space, $\tilde{\phi}$, is defined as

$$\xi = \frac{(\xi_{i+1} - \xi_i)\tilde{\xi} + (\xi_{i+1} + \xi_i)}{2} \tag{3.24}$$

$$\eta = \frac{(\eta_{i+1} - \eta_i)\tilde{\eta} + (\eta_{i+1} + \eta_i)}{2} \tag{3.25}$$

Jacobian determinant of this mapping is

$$|J_\phi| = \frac{(\xi_{i+1} - \xi_i)}{2} \frac{(\eta_{i+1} - \eta_i)}{2} \tag{3.26}$$

The mapping from parameter space to the physical space, **x**, is carried out by by using the NURBS basis functions

$$\begin{Bmatrix} x \\ y \end{Bmatrix} = \sum_{k=1}^{n_{cp}} R_k(\xi, \eta) \begin{Bmatrix} Px_k \\ Py_k \end{Bmatrix} \tag{3.27}$$

where R is the 2-D NURBS basis functions, n_{cp} is the number of control points per element and Px and Py are the coordinates of the control points. Jacobian of the mapping is

$$J_{\mathbf{x}} = \begin{bmatrix} \frac{\partial x}{\partial \xi} & \frac{\partial y}{\partial \xi} \\ \frac{\partial x}{\partial \eta} & \frac{\partial y}{\partial \eta} \end{bmatrix} \tag{3.28}$$

where partial derivatives are calculated by taking the derivative of Equation (3.27).

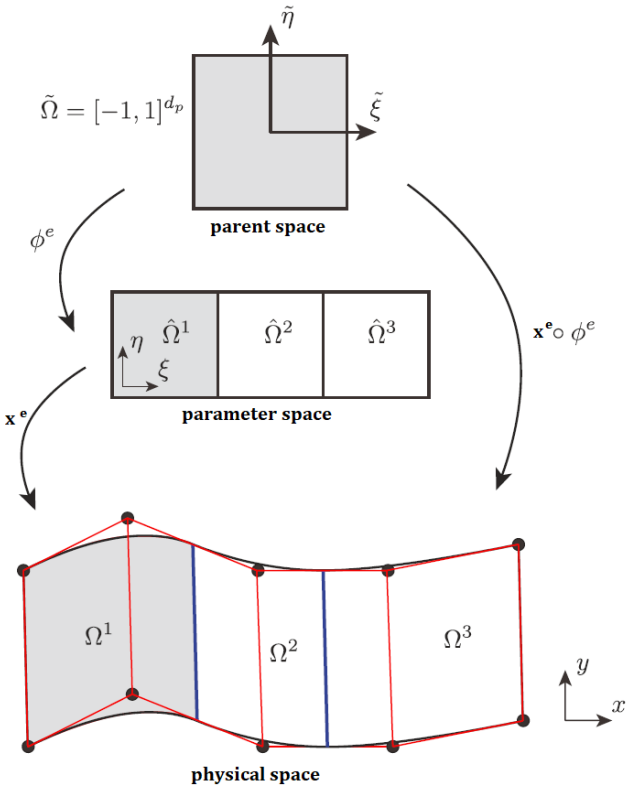

Figure 3.15: Mappings between relevant spaces [8].

To perform integration, quadrature points on an element at the physical space is pulled back to the parent space in two steps. First, by mapping x^{-1} they pulled back to the parameter space, then by mapping ϕ^{-1} they pulled back to the parent space. Inverse of the Jacobians of the corresponding mappings are required in these operations.

$$\begin{Bmatrix} \frac{\partial R_k}{\partial x} \\ \frac{\partial R_k}{\partial y} \end{Bmatrix} = J_{\mathbf{x}}^{-1} \begin{Bmatrix} \frac{\partial R_k}{\partial \xi} \\ \frac{\partial R_k}{\partial \eta} \end{Bmatrix} \tag{3.29}$$

3.3.2 Gaussian Quadrature

Two dimensional Gaussian quadrature is used as the technique for numerical integration. Integration takes place in knot spans as elements. To implement this integration method, the NURBS basis functions, and Jacobian determinants should be calculated for every integration point. Integral of a function $f = f(x, y)$ in physical space is

$$\int_{\Omega} f(x,y) d\Omega = \sum_{e=1}^{n} \int_{\Omega_e} f(x,y) d\Omega_e \tag{3.30}$$

where e indicates element in physical space. When this integration is mapped to the parent space

$$\sum_{e=1}^{n} \int_{\Omega_e} f(x,y) d\Omega_e = \sum_{e=1}^{n} \int_{\Omega_{\tilde{e}}} f(\tilde{\xi},\tilde{\eta}) |J_{\mathbf{x}}| d\Omega_{\tilde{e}} \tag{3.31}$$

Integral can be re-expressed by two integrals

$$\sum_{e=1}^{n} \int_{\Omega_{\tilde{e}}} f(\tilde{\xi},\tilde{\eta}) |J_{\mathbf{x}}| d\Omega_{\tilde{e}} = \sum_{e=1}^{n} \int_{-1}^{1} \int_{-1}^{1} f(\tilde{\xi},\tilde{\eta}) |J_{\mathbf{x}}| d\tilde{\xi} d\tilde{\eta} \tag{3.32}$$

Using Gauss quadrature

$$\int_{-1}^{1} \int_{-1}^{1} f(\tilde{\xi},\tilde{\eta}) d\tilde{\xi} d\tilde{\eta} = \sum_{i=1}^{p} \sum_{j=1}^{q} W_i W_j f(\tilde{\xi}_i, \tilde{\eta}_j) \tag{3.33}$$

Therefore,

$$\int_{\Omega} f(x,y) d\Omega = \sum_{e=1}^{n} \sum_{i=1}^{p} \sum_{j=1}^{q} W_i W_j f(\tilde{\xi}_i, \tilde{\eta}_j) |J_{\mathbf{x}}| \tag{3.34}$$

where p and q are orders of the NURBS basis functions; $\tilde{\xi}_i$ and $\tilde{\eta}_j$ are coordinates of the quadrature points and W_i and W_j are quadrature weights in ξ and η directions, respectively.

3.4 IGA vs FEM, Similarities and Differences

Both IGA and FEM use basis functions to approximate the unknown solution field; however, IGA uses the exact representation of the geometry, and uses the same functions for solution field approximation, on the other hand; the geometry is also approximated in addition to the solution field in finite element analysis. This is the most important and distinct feature of IGA. By not approximating the geometry, results of IGA become more precise. Moreover, since IGA uses the exact geometry, no further work required to redefine the geometry for studies like refinement. Secondly, the NURBS basis functions used in IGA are generally not interpolating to the control points, in contrast with the basis functions of the FEM which interpolated nodal points even though the degrees of freedoms are located at control points and nodal points in IGA and FEM, respectively. Thirdly, while basis functions of the FEM can tale positive or negative values, basis functions of IGA are strictly non-negative. Another difference is about the parameter space. Isoparametric finite element method and IGA have many common characteristics. However, while parameter space is mapped to a unique element in the physical space of FEM, mapping of the IGA is unique for a patch containing multiple elements. Furthermore, IGA has k-refinement method together with its similar refinement techniques with FEM, p- and h- refinements. The differences of the two methods are summed up in the Table 3.5 [1].

In terms of similarities, same methods can be applied to both IGA and isoparametric FEM such as Galerkin and collocation. They have same bandwidth for the same polynomial order and support of the basis functions are compact. Both FEM basis functions and NURBS basis functions constitute a partition of unity. Lastly, they have similar code implementation. Common features of the two method is summarized in the Table 3.6 [1].

Solution architecture of IGA is shown in the diagram in Figure 3.16. There are three main parts of the code, pre-processing, processing and post-processing. Material properties and boundary conditions are defined at pre-processing part. In addition, polynomial degree, control points, knot vectors are provided for isogeometric discretization. Connectivity array and IGA mesh created. Then, force vector and stiffness matrix are initialized. In the processing step, quadrature points are calculated.

Table 3.5: Differences between IGA and FEM [1].

Isogeometric Analysis	**Finite Element Analysis**
NURBS Basis Functions	Polynomial Basis Functions
Exact Representation of the Geometry	Approximation to the Geometry
Control Points	Nodal Points
Control Variables	Nodal Variables
Non-Interpolating Basis	Interpolating Basis
hpk-refinement	hp-refinement
Flexible Continuity	C^0 Continuity
Pointwise Positive Basis	Positive or Negative Basis
Convex Hull Property	No Convex Hull Property
Variation diminishing in the presence of discontinues data	Oscillatory in the presence of discontinues data

Table 3.6: Similarities between IGA and FEM [1].

Isogeometric Analysis and Finite Element Analysis
Isoparametric Concept
Galerkin's Method
Code Architecture
Compactly Supported Basis
Bandwith of Matrices
Partititon of Unity

Next, all elements are traveled in a loop and another loop travels through quadrature points inside the element loop. This loop is where mappings occur, basis functions and derivatives are computed, and calculated values are assembled to the global stiffness matrix and force vector. Afterwards, system is solved. Lastly, outputs are printed in the post-processing step. As is seen, it is almost the same as FEM architecture. Nevertheless, it differs in the application of the some of the steps. Read input changes since the two methods require different inputs. Connectivity array changes because of its dependence on the basis. Inherently, evaluation of basis functions and

their derivatives differ between FEM and IGA.

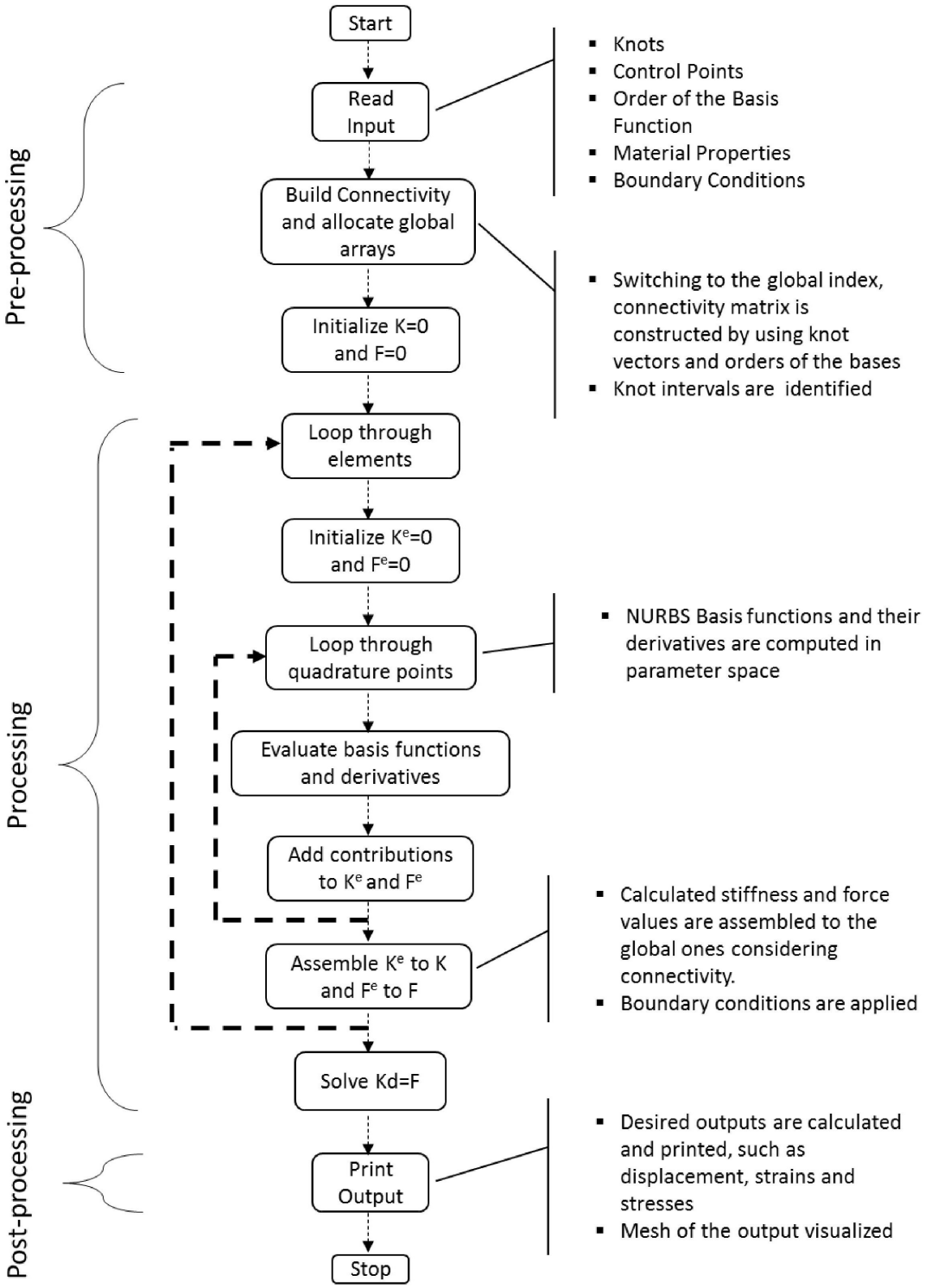

Figure 3.16: Diagram of coding architecture of IGA.

CHAPTER 4

GOVERNING EQUATIONS

In this part, equations will be derived for a composite laminated plate.

4.1 Displacements and strains of First Order Shear Deformation Theory

Let u_o, v_o and w_o be the displacement components along x, y and z coordinate directions, respectively, and ϕ_x denote rotation about x axis and ϕ_y denote rotation about y axis. As mentioned in Chapter 2, the first order shear deformation theory based on the displacement field, as given by Equation (2.2),

$$\begin{aligned} u(x,y,z) &= u_0(x,y) + z\phi_x(x,y) \\ v(x,y,z) &= v_0(x,y) + z\phi_y(x,y) \\ w(x,y,z) &= w_0(x,y) \end{aligned} \tag{4.1}$$

In-plane strains are calculated as follows:

$$\begin{aligned} \varepsilon_{xx} &= \frac{\partial u}{\partial x} \\ &= u_{0,x} + z\phi_{x,x} \\ \varepsilon_{yy} &= \frac{\partial v}{\partial y} \\ &= v_{0,y} + z\phi_{y,y} \\ \gamma_{xy} &= \frac{\partial u}{\partial y} + \frac{\partial v}{\partial x} \\ &= u_{0,y} + v_{0,x} + z(\phi_{x,y} + \phi_{y,x}) \end{aligned} \tag{4.2}$$

Similarly, transverse shear strains can be calculated as shown below:

$$\begin{aligned}\gamma_{yz} &= \frac{\partial v}{\partial z} + \frac{\partial w}{\partial y} \\ &= \phi_{\,y} + w_{\,0,y} \\ \gamma_{xz} &= \frac{\partial u}{\partial z} + \frac{\partial w}{\partial x} \\ &= \phi_{\,x} + w_{\,0,x}\end{aligned} \tag{4.3}$$

In-plane, ε^p, and transverse shear strain, ε^s, vectors can be written as

$$\varepsilon^p = \begin{Bmatrix} \varepsilon_{xx} \\ \varepsilon_{yy} \\ \gamma_{xy} \end{Bmatrix} = \begin{Bmatrix} u_{\,0,x} \\ v_{\,0,y} \\ u_{\,0,y} + v_{\,0,x} \end{Bmatrix} + z \begin{Bmatrix} \phi_{\,x,x} \\ \phi_{\,y,y} \\ \phi_{\,x,y} + \phi_{\,y,x} \end{Bmatrix} = \varepsilon^m + z\varepsilon^b \tag{4.4}$$

$$\varepsilon^s = \begin{Bmatrix} \gamma_{yz} \\ \gamma_{xz} \end{Bmatrix} = \begin{Bmatrix} w_{\,0,y} + \phi_{\,y} \\ w_{\,0,x} + \phi_{\,x} \end{Bmatrix} \tag{4.5}$$

where ε^m and ε^b stands for membrane and bending strains, respectively.

4.2 Constitutive Relations

The single subscript notation of the generalized constitutive equation for composite material is

$$\sigma_{\,i} = C_{ij}\,\varepsilon_{\,j} \tag{4.6}$$

where C_{ij} is stiffness tensor. The fiber reinforced laminated composite plates can be modeled as combination of orthotropic layers since there exist three planes of material symmetry. Therefore, the constitutive relation takes the following form:

$$\begin{Bmatrix} \sigma_1 \\ \sigma_2 \\ \sigma_3 \\ \sigma_4 \\ \sigma_5 \\ \sigma_6 \end{Bmatrix} = \begin{bmatrix} C_{11} & C_{12} & C_{13} & 0 & 0 & 0 \\ C_{12} & C_{22} & C_{23} & 0 & 0 & 0 \\ C_{13} & C_{23} & C_{33} & 0 & 0 & 0 \\ 0 & 0 & 0 & C_{44} & 0 & 0 \\ 0 & 0 & 0 & 0 & C_{55} & 0 \\ 0 & 0 & 0 & 0 & 0 & C_{66} \end{bmatrix} \begin{Bmatrix} \varepsilon_1 \\ \varepsilon_2 \\ \varepsilon_3 \\ \varepsilon_4 \\ \varepsilon_5 \\ \varepsilon_6 \end{Bmatrix} \tag{4.7}$$

where the stress components are $\sigma_1 = \sigma_{xx}$, $\sigma_2 = \sigma_{yy}$, $\sigma_3 = \sigma_{zz}$, $\sigma_4 = \tau_{yz}$, $\sigma_5 = \tau_{xz}$ and $\sigma_6 = \sigma_{xy}$, similarly, the strain components are $\varepsilon_1 = \varepsilon_{xx}$, $\varepsilon_2 = \varepsilon_{yy}$, $\varepsilon_3 = \varepsilon_{zz}$, $\varepsilon_4 = \gamma_{yz}$, $\varepsilon_5 = \gamma_{xz}$ and $\varepsilon_6 = \gamma_{xy}$. The plane stress condition can be assumed for lamina; however, although transverse shear stresses are small, they cannot be neglected since lamina is weak in transverse directions. Therefore, with $\sigma_3 = 0$, rewriting the Equation (4.7) :

$$\begin{Bmatrix} \sigma_1 \\ \sigma_2 \\ \sigma_3 \\ \sigma_4 \\ \sigma_5 \\ \sigma_6 \end{Bmatrix} = \begin{bmatrix} Q_{11} & Q_{12} & 0 & 0 & 0 & 0 \\ Q_{12} & Q_{22} & 0 & 0 & 0 & 0 \\ 0 & 0 & 0 & 0 & 0 & 0 \\ 0 & 0 & 0 & Q_{44} & 0 & 0 \\ 0 & 0 & 0 & 0 & Q_{55} & 0 \\ 0 & 0 & 0 & 0 & 0 & Q_{66} \end{bmatrix} \begin{Bmatrix} \varepsilon_1 \\ \varepsilon_2 \\ \varepsilon_3 \\ \varepsilon_4 \\ \varepsilon_5 \\ \varepsilon_6 \end{Bmatrix} \tag{4.8}$$

where Q_{ij} is known as the plane stress reduced stiffness matrix. Noting that, Poisson ratios ν_{ij} and ν_{ji} are related by $\nu_{ji} = E_j \nu_{ij} / E_i$ for orthotropic materials,

$$Q_{11} = \frac{E_1}{1 - \nu_{12}\nu_{21}}, \quad Q_{12} = \frac{\nu_{12} E_2}{1 - \nu_{12}\nu_{21}}, \quad Q_{22} = \frac{E_2}{1 - \nu_{12}\nu_{21}}$$
$$Q_{44} = G_{23}, \quad Q_{55} = G_{13}, \quad Q_{66} = G_{12}$$

where E_1 and E_2 longitudinal and transverse elastic modulus and G_{ij} is shear modulus in ij plane.

Laminates composed of many layers with different orientations. The coordinates for each lamina are called material coordinates of that lamina, and 1-direction is parallel to the fiber direction, 2-direction is perpendicular to the fiber direction and 3-direction is out-of-plane direction as shown in the Figure 4.1a. So far, the stress-strain relations are expressed in material coordinates. To write constitutive relation for laminate, a general coordinate system is needed. This coordinate system is called problem coordinate system. The difference between the two coordinate systems are illustrated in Figure 4.1b. The relation between stresses in material and problem coordinates are:

$$\sigma_{problem} = [T]\, \sigma_{material} \tag{4.9}$$

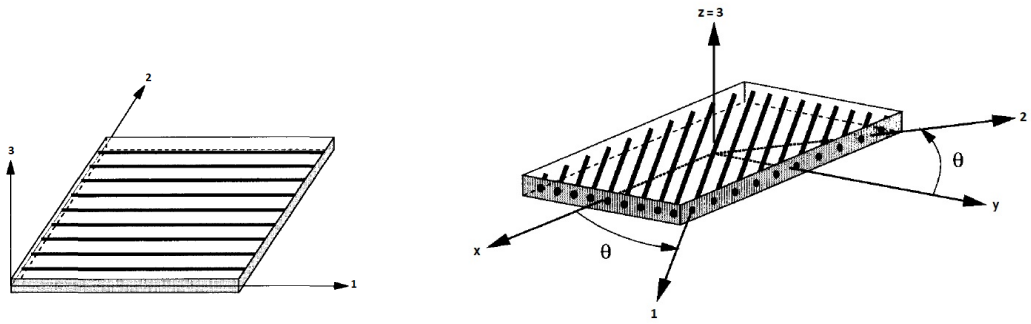

(a) (b)

Figure 4.1: (a) The material coordinates of a unidirectional fiber reinforced lamina [9]. (b) The material coordinates (1, 2, 3) and the problem coordinates (x, y, z) [9].

where T is the transformation matrix in the Equation (4.10)

$$T = \begin{bmatrix} cos^2(\theta) & sin^2(\theta) & 0 & 0 & 0 & -2sin(\theta)cos(\theta) \\ sin^2(\theta) & cos^2(\theta) & 0 & 0 & 0 & 2sin(\theta)cos(\theta) \\ 0 & 0 & 1 & 0 & 0 & 0 \\ 0 & 0 & 0 & cos(\theta) & sin(\theta) & 0 \\ 0 & 0 & 0 & -sin(\theta) & cos(\theta) & 0 \\ sin(\theta)cos(\theta) & -sin(\theta)cos(\theta) & 0 & 0 & 0 & cos^2(\theta) - sin^2(\theta) \end{bmatrix} \tag{4.10}$$

Similarly, the relation between strains in material and problem coordinates are:

$$\varepsilon_{material} = [T]^T \varepsilon_{problem} \tag{4.11}$$

Lastly, the plane stress reduced stiffness matrix in problem coordinates is named as $[\bar{Q}]$ and calculated by the following equation

$$[\bar{Q}] = [T]\,[Q]\,[T]^T \tag{4.12}$$

Now, for the k^{th} lamina, the reduced plane stress constitutive relation in problem

coordinates is:

$$\begin{Bmatrix} \sigma_x \\ \sigma_y \\ \tau_{xy} \\ \tau_{yz} \\ \tau_{xz} \\ \sigma_z \end{Bmatrix}^{(k)} = \begin{bmatrix} \bar{Q}_{11} & \bar{Q}_{12} & \bar{Q}_{16} & 0 & 0 & 0 \\ \bar{Q}_{12} & \bar{Q}_{22} & \bar{Q}_{26} & 0 & 0 & 0 \\ \bar{Q}_{16} & \bar{Q}_{26} & \bar{Q}_{66} & 0 & 0 & 0 \\ 0 & 0 & 0 & \bar{Q}_{44} & \bar{Q}_{45} & 0 \\ 0 & 0 & 0 & \bar{Q}_{45} & \bar{Q}_{55} & 0 \\ 0 & 0 & 0 & 0 & 0 & 0 \end{bmatrix}^{(k)} \begin{Bmatrix} \varepsilon_x \\ \varepsilon_y \\ \gamma_{xy} \\ \gamma_{yz} \\ \gamma_{xz} \\ \varepsilon_z \end{Bmatrix}^{(k)} \tag{4.13}$$

4.3 Resultants and Weak Form Equation for Composite Plates

All stresses and strains are calculated in the mid-plane in the FSDT. The mid-plane and position of the plies can be seen in Figure 4.2 To write the weak form for

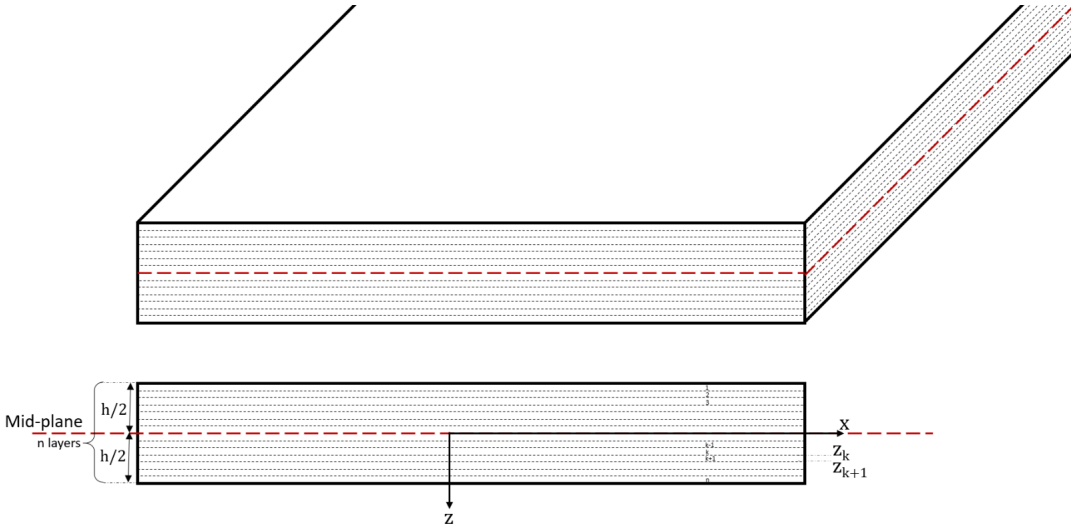

Figure 4.2: Shematic of a laminate

laminated composite plate, stiffness matrix of constitutive equation that relate force and moment resultants to the strains of the laminate is required. Therefore, for n

layered laminate, in-plane force resultants can be calculated by

$$\begin{Bmatrix} N_x \\ N_y \\ N_{xy} \end{Bmatrix} = \sum_{k=1}^{n} \int_{z_k}^{z_{k+1}} \begin{Bmatrix} \sigma_x \\ \sigma_y \\ \tau_{xy} \end{Bmatrix} dz \tag{4.14}$$

$$= \sum_{k=1}^{n} \int_{z_k}^{z_{k+1}} \begin{bmatrix} \bar{Q}_{11} & \bar{Q}_{12} & \bar{Q}_{16} \\ \bar{Q}_{12} & \bar{Q}_{22} & \bar{Q}_{26} \\ \bar{Q}_{16} & \bar{Q}_{26} & \bar{Q}_{66} \end{bmatrix}^{(k)} \begin{Bmatrix} u_{0,x} + z\phi_{x,x} \\ v_{0,y} + z\phi_{y,y} \\ u_{0,y} + v_{0,x} + z(\phi_{x,y} + \phi_{y,x}) \end{Bmatrix} dz$$

$$\begin{Bmatrix} N_x \\ N_y \\ N_{xy} \end{Bmatrix} = \begin{bmatrix} A_{11} & A_{12} & A_{16} \\ A_{12} & A_{22} & A_{26} \\ A_{16} & A_{26} & A_{66} \end{bmatrix} \begin{Bmatrix} u_{0,x} \\ v_{0,y} \\ u_{0,y} + v_{0,x} \end{Bmatrix} + \begin{bmatrix} B_{11} & B_{12} & B_{16} \\ B_{12} & B_{22} & B_{26} \\ B_{16} & B_{26} & B_{66} \end{bmatrix} \begin{Bmatrix} z\phi_{x,x} \\ z\phi_{y,y} \\ z(\phi_{x,y} + \phi_{y,x}) \end{Bmatrix} \tag{4.15}$$

In a similar way, moment resultants are calculated by

$$\begin{Bmatrix} M_x \\ M_y \\ M_{xy} \end{Bmatrix} = \sum_{k=1}^{n} \int_{z_k}^{z_{k+1}} \begin{Bmatrix} \sigma_x \\ \sigma_y \\ \tau_{xy} \end{Bmatrix} z\, dz \tag{4.16}$$

$$= \sum_{k=1}^{N} \int_{z_k}^{z_{k+1}} \begin{bmatrix} \bar{Q}_{11} & \bar{Q}_{12} & \bar{Q}_{16} \\ \bar{Q}_{12} & \bar{Q}_{22} & \bar{Q}_{26} \\ \bar{Q}_{16} & \bar{Q}_{26} & \bar{Q}_{66} \end{bmatrix}^{(k)} \begin{Bmatrix} u_{0,x} + z\phi_{x,x} \\ v_{0,y} + z\phi_{y,y} \\ u_{0,y} + v_{0,x} + z(\phi_{x,y} + \phi_{y,x}) \end{Bmatrix} z\, dz$$

$$\begin{Bmatrix} M_x \\ M_y \\ M_{xy} \end{Bmatrix} = \begin{bmatrix} B_{11} & B_{12} & B_{16} \\ B_{12} & B_{22} & B_{26} \\ B_{16} & B_{26} & B_{66} \end{bmatrix} \begin{Bmatrix} u_{0,x} \\ v_{0,y} \\ u_{0,y} + v_{0,x} \end{Bmatrix} + \begin{bmatrix} D_{11} & D_{12} & D_{16} \\ D_{12} & D_{22} & D_{26} \\ D_{16} & D_{26} & D_{66} \end{bmatrix} \begin{Bmatrix} z\phi_{x,x} \\ z\phi_{y,y} \\ z(\phi_{x,y} + \phi_{y,x}) \end{Bmatrix} \tag{4.17}$$

Lastly, transverse force resultants,

$$\begin{Bmatrix} Q_x \\ Q_y \end{Bmatrix} = \sum_{k=1}^{n} \int_{z_k}^{z_{k+1}} \begin{Bmatrix} \tau_{yz} \\ \tau_{xz} \end{Bmatrix} dz \tag{4.18}$$

$$= \sum_{k=1}^{N} \int_{z_k}^{z_{k+1}} \begin{bmatrix} \bar{Q}_{44} & \bar{Q}_{55} \\ \bar{Q}_{55} & \bar{Q}_{44} \end{bmatrix}^{(k)} \begin{Bmatrix} \phi_y + w_{0,y} \\ \phi_x + w_{0,x} \end{Bmatrix} dz$$

$$\begin{Bmatrix} Q_x \\ Q_y \end{Bmatrix} = \kappa \begin{bmatrix} D^s_{11} & D^s_{12} \\ D^s_{12} & D^s_{22} \end{bmatrix} \begin{Bmatrix} \phi_y + w_{0,y} \\ \phi_x + w_{0,x} \end{Bmatrix} \tag{4.19}$$

z_k and z_{k+1} are top and bottom coordinates of a lamina as shown in the Figure 4.2, and κ is the shear correction factor. The matrices $[A]$, $[B]$, $[D]$ and $[D^s]$ are called extensional stiffness matrix, coupling stiffness matrix, bending stiffness matrix and transverse shearing stiffness matrix, respectively. As can be seen from Equations (4.14)-(4.19), they are defined as:

$$(A_{ij},\ B_{ij},\ D_{ij}) = \sum_{k=1}^{N} \int_{z_k}^{z_{k+1}} \bar{Q}^{(k)}_{ij}(1,\ z,\ z^2)dz \quad i,j = 1,2,6 \tag{4.20a}$$

and

$$D^s_{ij} = \sum_{k=1}^{N} \int_{z_k}^{z_{k+1}} \bar{Q}^{(k)}_{ij} dz \quad i,j = 4,5 \tag{4.20b}$$

or,

$$A_{ij} = \sum_{k=1}^{N} \bar{Q}^{(k)}_{ij}(z_{k+1} - z_k), \quad B_{ij} = \frac{1}{2}\sum_{k=1}^{N} \bar{Q}^{(k)}_{ij}(z^2_{k+1} - z^2_k), \tag{4.20c}$$

$$D_{ij} = \frac{1}{3}\sum_{k=1}^{N} \bar{Q}^{(k)}_{ij}(z^3_{k+1} - z^3_k) \quad i,j = 1,2,6$$

and

$$D^s_{ij} = \sum_{k=1}^{N} \bar{Q}^{(k)}_{ij}(z_{k+1} - z_k) \quad i,j = 4,5 \tag{4.20d}$$

Defining $\bar{C}$ by combining A, B and D matrices,

$$\bar{C} = \begin{bmatrix} A & B \\ B & D \end{bmatrix} \tag{4.21}$$

Consequently, for a domain Ω in $\mathbb{R}^2$, a weak form for laminated composite plate for static analysis is

$$\int_\Omega \delta\varepsilon^{p^T} \bar{C}\, \varepsilon^p \, d\Omega \ + \int_\Omega \delta\varepsilon^{s^T} D^s\, \varepsilon^s \, d\Omega \ = \int_\Omega \delta w\, \boldsymbol{q}\, d\Omega \tag{4.22}$$

where $\boldsymbol{q}$ is the transverse loading per unit area.

4.4 Global Stiffness Matrix and Load Vector

The mid-plane of the laminated plate is a NURBS surface obtained by the equations in Chapter 3. A global index, A, is defined for numbering the control points as follows

$$A = n(j-1) + i \tag{4.23}$$

Using this global index, Equation (3.8) defining a B-spline surface can be rewritten as

$$S(\xi, \eta) = \sum_{A=1}^{nxm} N_A(\xi, \eta) P_A \tag{4.24}$$

where A is the global index of the corresponding control point, nxm is the number of the B-spline basis functions, N_A is product of basis functions $N_{i,p}(\xi)$ and $M_{j,q}(\eta)$ with order p and q and two knot vectors $\Xi = \{\xi_1, \xi_2, ...\xi_{n+p+1}\}$ and $\mathcal{H} = \{\eta_1, \eta_2, ...\eta_{m+q+1}\}$, respectively. Then, using Equation (4.24), Equation (3.21) defining a NURBS surface can be re-expressed as

$$S(\xi, \eta) = \sum_{A=1}^{nxm} R_A(\xi, \eta) P_A \tag{4.25}$$

where the NURBS function R_A is written by using the homogeneous coordinate w_A and weightening function as

$$R_A(\xi, \eta) = \frac{N_A(\xi, \eta) w_A}{w(\xi, \eta)} \tag{4.26}$$

Using the advantage of the IGA, functions that defines the exact geometry is used as interpolation functions of the displacement field

$$u^h = \sum_{A}^{nxm} R_A(\xi, \eta)\, q_A \tag{4.27}$$

where $q_A = [u_A \;\; v_A \;\; w_A \;\; \phi_{xA} \;\; \phi_{yA}]^T$ is the degree of freedom of u^h associated with control point A. Taking derivative of displacement field to obtain strains,

$$\varepsilon^m = \sum_A B_A^m \, q_A, \qquad \text{where} \quad B_A^m = \begin{bmatrix} R_{A,x} & 0 & 0 & 0 & 0 \\ 0 & R_{A,y} & 0 & 0 & 0 \\ R_{A,y} & R_{A,x} & 0 & 0 & 0 \end{bmatrix} \tag{4.28}$$

$$\varepsilon^b = \sum_A B_A^b \, q_A, \qquad \text{where} \quad B_A^b = \begin{bmatrix} 0 & 0 & 0 & R_{A,x} & 0 \\ 0 & 0 & 0 & 0 & R_{A,y} \\ 0 & 0 & 0 & R_{A,y} & R_{A,x} \end{bmatrix} \tag{4.29}$$

$$\varepsilon^s = \sum_A B_A^s \, q_A, \qquad \text{where} \quad B_A^s = \begin{bmatrix} 0 & 0 & R_{A,x} & R_A & 0 \\ 0 & 0 & R_{A,y} & 0 & R_A \end{bmatrix} \tag{4.30}$$

where ε^m, ε^b and ε^s are bending, membrane and shear strains, respectively, and B matrices are called strain-degree of freedom (DOF) matrix. Now, using the global stiffness matrix,

$$K = \int_\Omega {B^m}^T A B^m d\Omega + \int_\Omega {B^m}^T B B^b d\Omega + \int_\Omega {B^b}^T B B^m d\Omega + \int_\Omega {B^b}^T D B^b d\Omega + \int_\Omega {B^s}^T D^s B^s d\Omega \tag{4.31}$$

and the load vector;

$$F = \int_\Omega \boldsymbol{q} R d\Omega \; + f^b \tag{4.32}$$

The equation $Kq = F$, can be solved for global DOF vector q.

4.5 Strains and Stresses

The mid-plane strains can now be calculated using Equations (4.28), (4.29) and (4.30), since $\boldsymbol{q}$ is found. Afterwards, Equation (4.4) and (4.5) give the strains on top and bottom of the each lamina with respect to problem coordinates $(x,\, y,\, z)$. Then, Equation (4.13) can be used to calculate the stresses in problem coordinates $(x,\, y,\, z)$. However, to predict the failure, stresses in material coordinates, $(1,\, 2,\, 3)$, are required.

Using the Equation (4.9), stresses in the material coordinates is obtained as follows:

$$\begin{Bmatrix} \sigma_1 \\ \sigma_2 \\ \tau_{12} \\ \tau_{23} \\ \tau_{13} \end{Bmatrix} = \begin{bmatrix} cos^2(\theta) & sin^2(\theta) & sin(2\theta) & 0 & 0 \\ sin^2(\theta) & cos^2(\theta) & -sin(2\theta) & 0 & 0 \\ -\frac{1}{2}sin(2\theta) & \frac{1}{2}sin(2\theta) & cos(2\theta) & 0 & 0 \\ 0 & 0 & 0 & cos(\theta) & -sin(\theta) \\ 0 & 0 & 0 & sin(\theta) & cos(\theta) \end{bmatrix} \begin{Bmatrix} \sigma_x \\ \sigma_y \\ \tau_{xy} \\ \tau_{yz} \\ \tau_{xz} \end{Bmatrix} \quad (4.33)$$

To check the failure, the stresses in material coordinates found by Equation (4.33) should be substituted into failure criteria mentioned in Chapter 2, Section 2.2.

CHAPTER 5

RESULTS AND DISCUSSION

In this chapter, firstly, the solution procedure is verified by comparing the obtained results with the 3-D elasticity solution of Pagano [17]. Then, some numerical examples of analyses of laminates with different lamination schemes and boundary conditions are presented; displacements, stress and strain distributions, strength ratios are calculated and using the strength ratios a heat-map is generated for the plates showing the most critical regions.

5.1 Comparison of Result with Exact Solution

To verify the solution procedure, the obtained results for 3-layered graphite/epoxy square plate with orientation [0/90/0] are compared with the exact solution of Pagano [2]. Related material properties are tabulated in the Table 5.1. The plate is simply supported from all edges and subjected to a sinusoidal load. The schematic of the plate is shown in the Figure 5.1.

Table 5.1: Material properties of graphite/epoxy lamina.

Mechanical Property	Value
E_1	172.4 GPa
E_2	6.9 GPa
G_{12}	3447 MPa
G_{23}	1379 MPa
G_{13}	3447 MPa
$\nu_{12}, \nu_{13}, \nu_{23}$	0.25

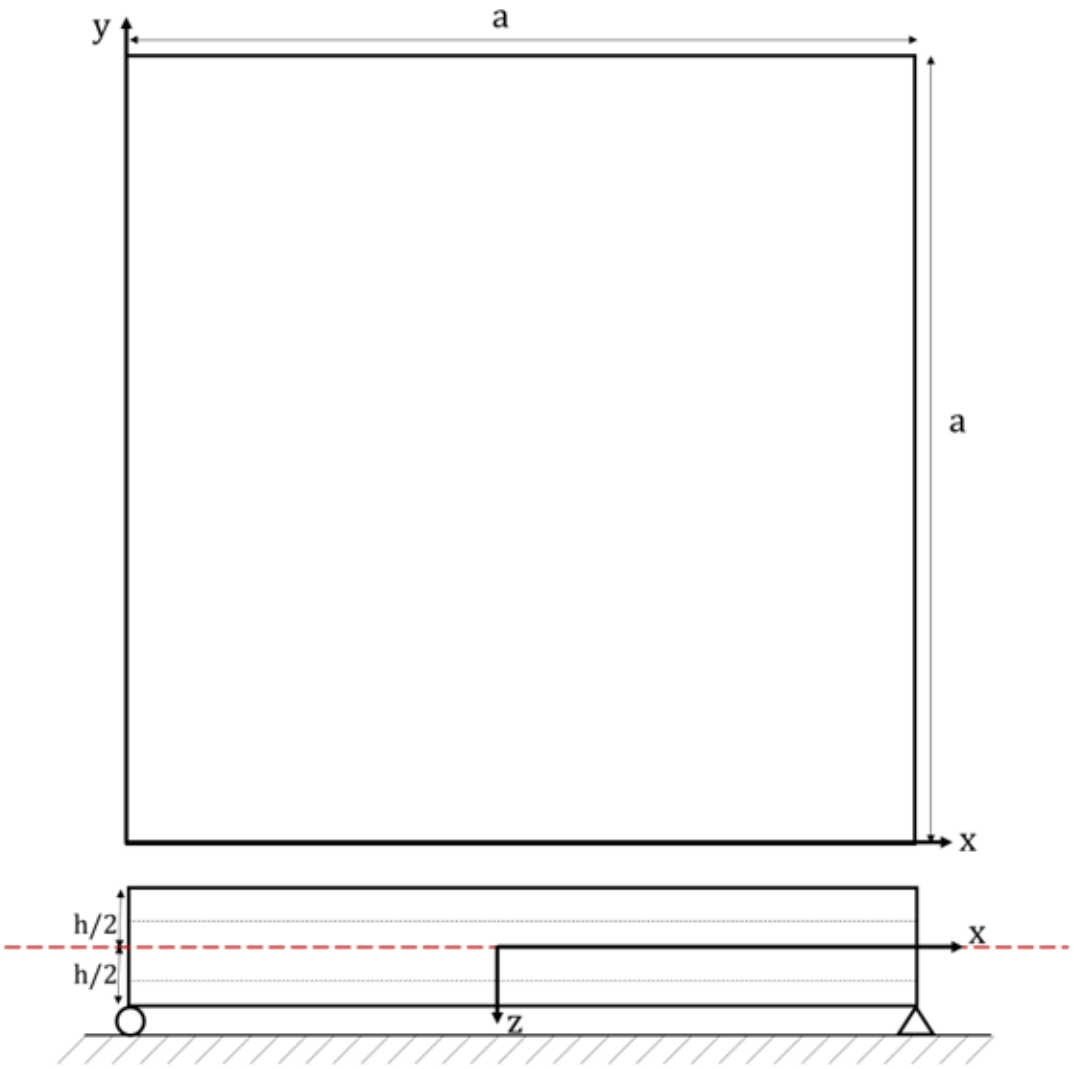

Figure 5.1: 3-layered simply supported square laminate

Dimensions of the square plate are denoted parametrically, where a is the edge length and h is the total thickness. Analyses are performed for plates with 64^2 elements for different a/h ratios. The loading on the top surface is

$$q = q_0 \, sin(\frac{\pi x}{a}) \, sin(\frac{\pi y}{b}) \tag{5.1}$$

Results are compared by normalized length, displacement and stresses defined as

follows

$$
\begin{aligned}
\bar{z} &= \frac{z}{h}, \\
\bar{w} &= \frac{\pi^4\, w\, h^3}{12\, q_0\, a^4}\left(4\, G_{12} + \frac{E_1 + E_2\,(1 + 2\nu_{23})}{1 - \nu_{12}\,\nu_{21}}\right) \\
\bar{\sigma}_x &= \frac{\sigma_x\, h^2}{q_0\, a^2}, \\
\bar{\sigma}_y &= \frac{\sigma_y\, h^2}{q_0\, a^2}, \\
\bar{\tau}_{xy} &= \frac{\tau_{xy}\, h^2}{q_0\, a^2} \\
\bar{\tau}_{yz} &= \frac{\tau_{zy}\, h}{q_0\, a}, \\
\bar{\tau}_{xz} &= \frac{\tau_{xy}\, h}{q_0\, a}
\end{aligned}
$$

Comparison of the results are given in Table 5.2.

Table 5.2: Comparison of the results with 3-D elasticity solution [2].

	a/h	$\bar{\sigma}_x$	$\bar{\sigma}_y$	$\bar{\tau}_{xz}$	$\bar{\tau}_{yz}$	$\bar{\tau}_{xy}$	$\bar{w}$
Elasticity	10	0.559	0.401	0.301	0.196	0.0275	1.709
IGA-FSDT		0.505	0.365	0.433	0.136	0.0202	1.556
Elasticity	50	0.539	0.176	0.337	0.141	0.0216	1.031
IGA-FSDT		0.538	0.274	0.440	0.176	0.0208	1.026
Elasticity	100	0.539	0.271	0.339	0.139	0.0214	1.008
IGA-FSDT		0.539	0.271	0.442	0.211	0.0220	1.007

As the results in Table 5.2 indicates, with increasing a/h ratio accuracy of the IGA-FSDT solution increases and results for $a/h = 100$ is obtained for $\bar{\sigma}_x$ and $\bar{\sigma}_y$ are the same, for $\bar{\tau}_{xy}$ and $\bar{w}$ are very close to the elasticity solutions. Therefore, in the following numerical examples, plates with higher a/h ratios are examined. For the lower values, other methods such as higher order, layerwise or 3-D approaches might be implemented for solution. Nevertheless, transverse shear values, $\bar{\tau}_{xz}$ and $\bar{\tau}_{yz}$ are still overestimated in the FSDT. It is result of constant shear assumption of the FSDT with shear correction factor. In the above calculations, the SCF is taken as $5/6$ which is the most commonly used value in literature. Increasing the SCF, results get closer

to the exact solution as shown in Table 5.3. However, it should be noted that the SCF depends many other properties such as material coefficients, alignment of the plies, geometry of the plate, loading and boundary conditions [43, 49]; therefore, this trend cannot be generalized.

Table 5.3: Effect of the shear correction factor for $a/h = 100$.

	SCF	$\bar{\tau}_{xz}$	$\bar{\tau}_{yz}$
Elasticity		0.339	0.139
IGA-FSDT	$5/6$	0.442	0.211
	$6/7$	0.429	0.203
	1	0.3670	0.162

5.2 Numerical Examples

In this section, several laminated plates are analyzed. Their critical regions are presented through a heat-map obtained by the strength ratios (SR). SR values are calculated according to five different failure theories which are maximum stress, Tsai-Hill, Hoffman, Tsai-Wu and Hashin. Although SR values of all theories are given for comparison of the theories, the heat-map always generated for Hashin failure criteria because of the failure mode prediction property of the theory. Moreover, variation of the stresses through the thickness is plotted for all examples. Analyses are carried out for fully clamped, one-end clamped and two-ends clamped plates. To ensure that linear analysis procedure is acceptable, linear and nonlinear analyses are performed using MSC Nastran for all examples and force-displacement curves are obtained. Commenting on the curves, and knowing the practical application in aerospace industry, the applied loads are chosen so that the maximum displacement is less than the half of the thickness of the plate for fully clamped plates and 20% of the thickness for one-end and two-ends clamped plates. For each boundary conditions, symmetric plates with various ply orientation are examined.

The laminates considered in this study are consist of unidirectional carbon/epoxy layers with properties given in Table 5.4. Ply thickness is $0.25\,mm$ for all cases.

For isogeometric analyses of the plate by FSDT, the mid-plane geometry is modeled using knot vectors in ξ and η directions, order of the basis polynomials, p and q and the control points.

Table 5.4: Material properties of carbon/epoxy lamina.

Mechanical Property	Value
E_1	152 GPa
E_2	9.7 GPa
G_{12}	4900 MPa
G_{23}	4900 MPa
G_{13}	4900 MPa
ν_{12}	0.34
$(\sigma_1^T)_{ult}$	2700 MPa
$(\sigma_1^C)_{ult}$	1500 MPa
$(\sigma_2^T)_{ult}$	75 MPa
$(\sigma_2^C)_{ult}$	300 MPa
$(\sigma_3^T)_{ult}$	75 MPa
$(\sigma_3^C)_{ult}$	300 MPa
$(\tau_{12})_{ult}$	140 MPa
$(\tau_{13})_{ult}$	95 MPa
$(\tau_{23})_{ult}$	95 MPa

5.2.1 Fully Clamped Plates

This section consists of solutions of fully clamped square plate with different thickness and different ply orientations under uniform loading on the top surface. Dimension of the plate is $200\,mm$ x $200\,mm$. Aforementioned, ply thickness is $0.25\,mm$ for each layer and material is carbon/epoxy with properties given in Table 5.4. The fully clamped square plate is illustrated in Figure 5.2.

The inputs to model the square plate are listed in Table 5.5 and Table 5.6. After k-refinement control points are increased to 66x66 to have accurate solution on the

mid-point of the surface.

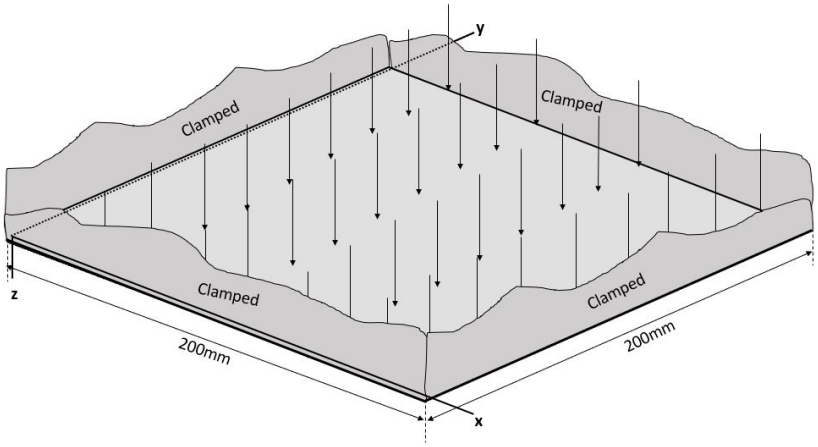

Figure 5.2: Distributed load applied to the top surface of a fully clamped square plate.

Table 5.5: Polynomial orders and knot vectors representing the mid-plane of a square laminate before refinement.

p	1
q	1
Ξ	0, 0, 1, 1
$\mathcal{H}$	0, 0, 1, 1

Table 5.6: Control points of mid-plane of a square laminate before refinement.

Point	(x,y) $[mm]$
1	(0, 0)
2	(200, 0)
3	(0, 200)
4	(200, 200)

5.2.1.1 14-layer symmetric square cross-ply laminate with orientation $[\mathbf{0/90/0/90/0/90/0}]_s$

The total thickness of the laminate is $3.5\,mm$. The linear and nonlinear pressure-displacement graph obtained by MSC Nastran is shown in the Figure 5.3. For dis-

placement less than 50% of the thickness is assumed in linear region. Therefore, according to the linear solution in Figure 5.3, pressure leading $1.75\,mm$ displacement, $0.195\,MPa$, is applied at the top surface of the plate. For the results obtained by IGA code, displacement of the $(x,\ 100,\ 0)$ line, which is the mid-line of the mid-plate, is given in the Figure 5.4. The maximum displacement of $1.74\,mm$ is read from the results. Figure 5.5 shows the variation of problem stresses through the thickness where stresses have maximum values. The minimum SR for all failure criteria and expected strength ratios at failure (ESRF) according to different theories are listed in Table 5.7. The heat-map on Figure 5.6 is generated from SR values of the Hashin theory for layer 14 (bottom layer) which is the most critical layer according to the criteria. The failure mode is predicted to be tensile failure of the matrix. Red regions are more critical regions (low SR values), whereas blue regions represent the safer regions (high SR values).

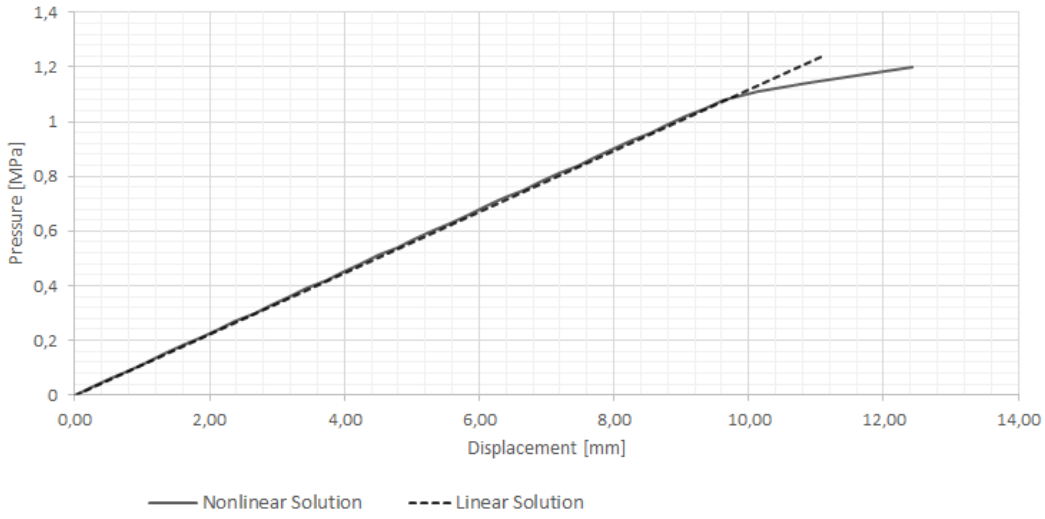

Figure 5.3: Pressure-displacement graph of $[\ 0/90/0/90/0/90/0\ ]_s$ laminae at maximum displacement location, $(x,\ 100,\ 0)$ for linear and nonlinear solutions.

Table 5.7: Minimum strength ratios and expected strength ratios at failure according to different failure criteria of the laminate $[0/90/0/90/0/90/0]_s$.

	Maximum Stress	Tsai-Hill	Hoffman	Tsai-Wu	Hashin
Minimum SR	2.948	2.920	2.920	2.932	2.920
ESRF	1.010	1.000	1.000	1.004	1.000

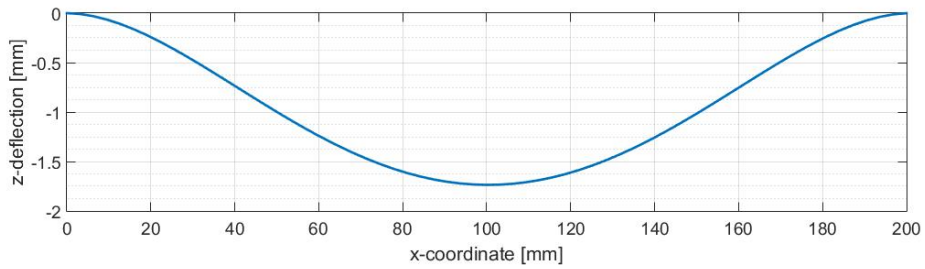

Figure 5.4: z-displacement graph of the IGA solution of the laminate $[0/90/0/90/0/90/0]_s$ at $(x,\ 100,\ 0)$.

5.2.1.2 14-layer symmetric square angle-ply laminate with orientation [45/-45/45/-45/45/-45/45]$_s$

Having $0.25\,mm$ layers, the total thickness of the plate is $3.5\,mm$. MSC Nastran results in Figure 5.7 shows the pressure-displacement graphs for linear and nonlinear solutions. Assuming linear solutions agrees well with the nonlinear solution for maximum displacement of half of the thickness, i.e. $1.75\,mm$, corresponding pressure $0.182\,MPa$, is applied to the top surface. Figure 5.8 shows the displacement of the $(x,\ 100,\ 0)$ line for IGA solutions. The maximum displacement is $1.71\,mm$. The variation of in-plane problem stresses through the thickness where stresses have maximum values are shown in Figure 5.9. The minimum SR for all failure criteria and expected strength ratios at failure (ESRF) according to different theories are listed in Table 5.8. The generated heat-map for SR values of the Hashin criteria for the layer having the lowest SR value, layer 14 (bottom layer), is shown in Figure 5.10. More critical regions with lower SR values are represented by red, and safer regions with higher SR values are shown with blue. The failure mode is predicted to be tensile failure of the matrix.

Table 5.8: Minimum strength ratios and expected strength ratios at failure according to different failure criteria of the laminate [45/-45/45/-45/45/-45/45]$_s$.

	Maximum Stress	Tsai-Hill	Hoffman	Tsai-Wu	Hashin
Minimum SR	3.614	3.176	3.372	3.839	3.316
ESRF	1.138	1.000	1.062	1.209	1.044

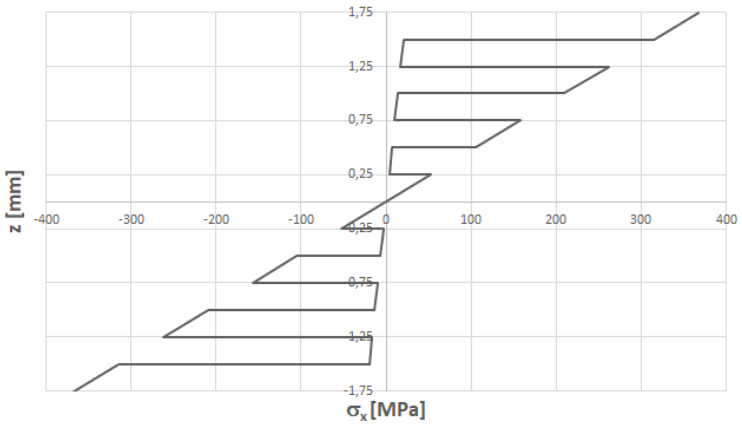

(a) σ_x

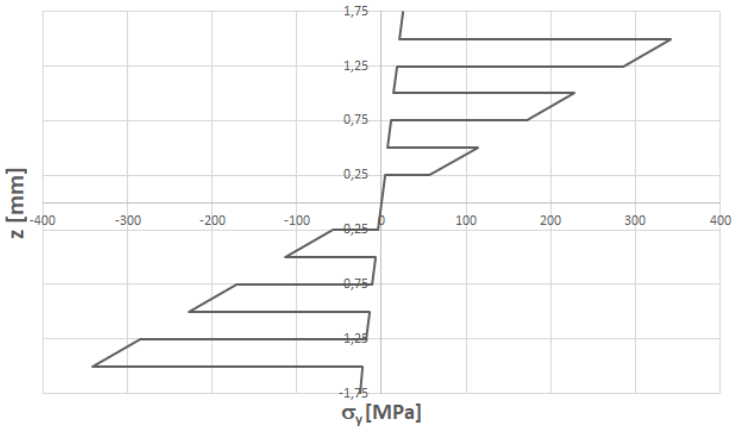

(b) σ_y

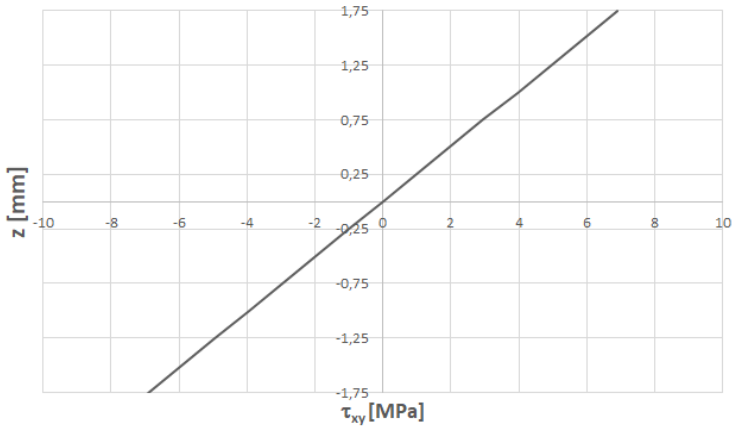

(c) τ_{xy}

Figure 5.5: Stress distribution through the thickness of fully clamped laminate $[0/90/0/90/0/90/0\,]_s$.

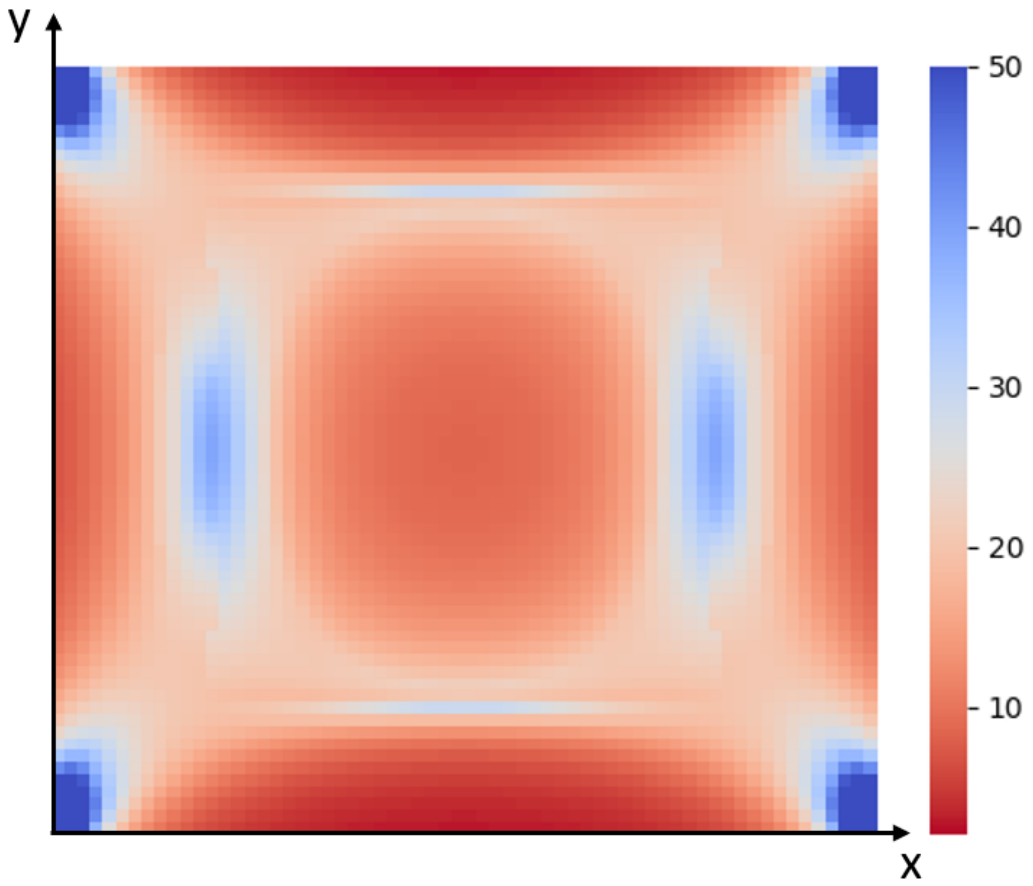

Figure 5.6: The SR distribution of the fully clamped square plate $[0/90/0/90/0/90/0]_s$ according to the Hashin criteria at layer 14.

5.2.1.3 14-layer symmetric square angle-ply laminate with orientation $[0/90/0/90/45/-45/0]_s$

14-layer laminate has the total thickness of $3.5\,mm$. The linear and nonlinear pressure-displacement graph obtained by MSC Nastran is shown in the Figure 5.11. For maximum displacement of half of the thickness, i.e. $1.75\,mm$, linear solutions agrees well with the nonlinear solution. Corresponding pressure for this displacement, $0.195\,MPa$, is applied to the top surface. The displacement of the IGA code, for the $(x,\ 100,\ 0)$ line is given in the Figure 5.12. The maximum displacement is $1.74\,mm$. The variation of problem stresses through the thickness for the elements with highest stresses, is shown in Figure 5.13. The minimum SR for all failure criteria and expected strength ratios at failure (ESRF) according to different theories are listed in Table 5.9. The

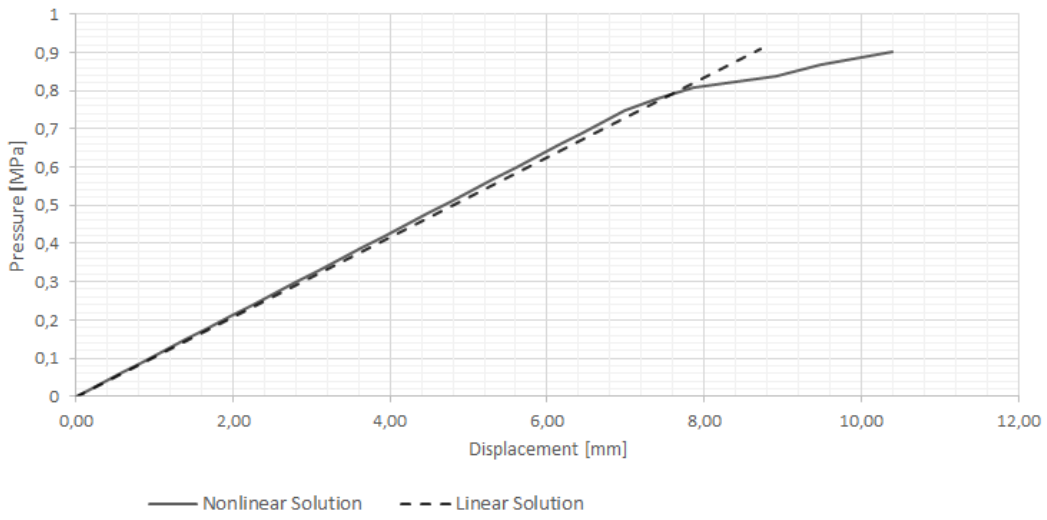

Figure 5.7: Pressure-displacement graph of $[45/\text{-}45/45/\text{-}45/45/\text{-}45/45]_s$ laminae at maximum displacement location, $(x,\ 100,\ 0)$ for linear and nonlinear solutions.

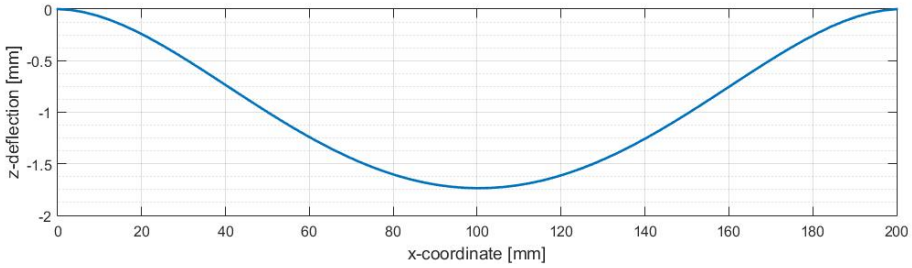

Figure 5.8: z-displacement graph of the IGA solution of the laminate $[45/\text{-}45/45/\text{-}45/45/\text{-}45/45]_s$ at $(x,\ 100,\ 0)$.

heat-map on Figure 5.14 is generated from SR values of the Hashin theory for layer 14 (bottom layer) which is the most critical layer according to the criteria. The failure mode is predicted to be tensile failure of the matrix. Red regions are more critical regions (low SR values), whereas blue regions represent the safer regions (high SR values).

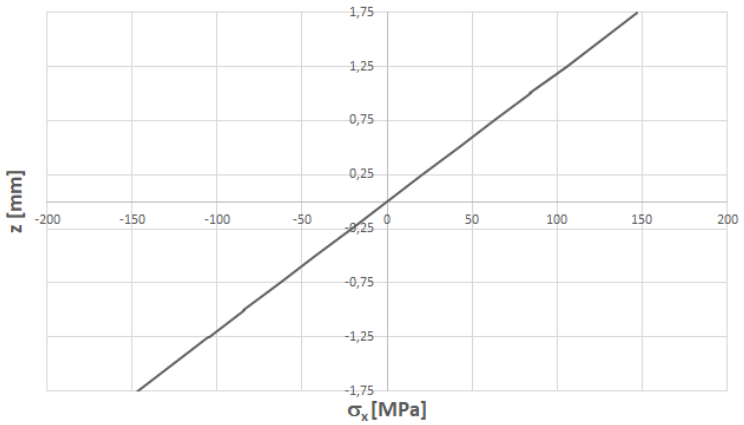

(a) σ_x

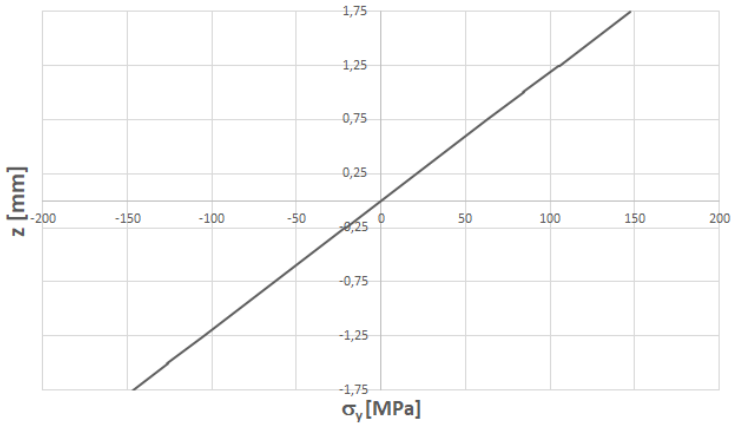

(b) σ_y

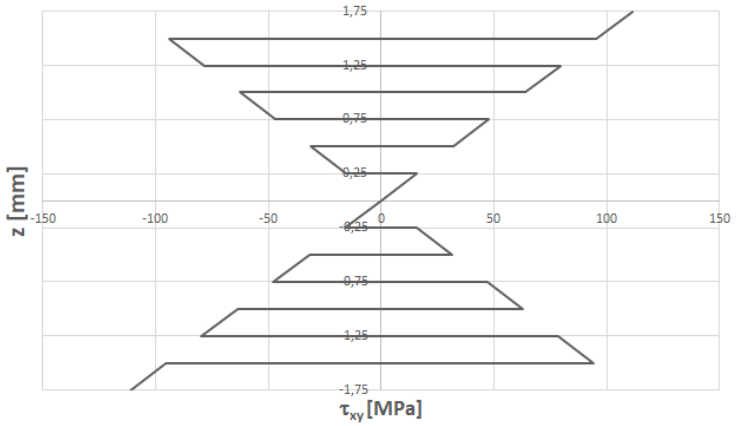

(c) τ_{xy}

Figure 5.9: Stress distribution through the thickness of fully clamped laminate $[45/\text{-}45/45/\text{-}45/45/\text{-}45/45]_s$.

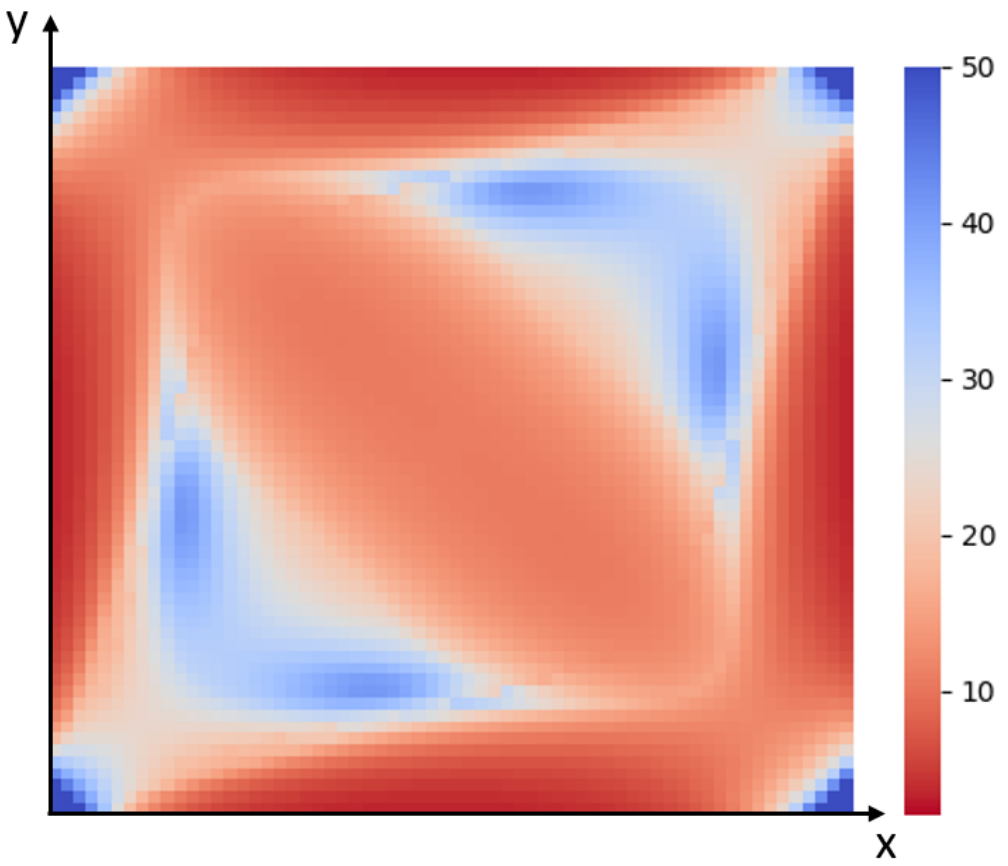

Figure 5.10: The SR distribution of the fully clamped square plate $[45/\text{-}45/\ 45/\ \text{-}45/45/\text{-}45/45]_s$ according to the Hashin criteria at layer 14.

5.2.1.4 8-layer symmetric square angle-ply laminate with orientation $[45/\text{-}45/45/\text{-}45]_s$

The total thickness of 14-layer laminate having $0.25\,mm$ layers, is $2\,mm$. Figure 5.15 shows applied pressure versus displacement graphs of linear and nonlinear solutions of MSC Nastran. The pressure causing maximum 50% of the thickness displacement, i.e. $1\,mm$, is $0.020\,MPa$. The pressure is applied to the top surface of the plate. For the obtained results by IGA code, displacement of the $(x,\ 100,\ 0)$ line is given in the Figure 5.16. The maximum displacement of $1\,mm$ is read from the IGA results. Figure 5.17 shows the variation of problem stresses through the thickness where stresses have maximum values. The minimum SR for all failure criteria and expected strength ratios at failure (ESRF) according to different theories are listed in Table 5.10. The heat-map on Figure 5.18 is generated from SR values of the Hashin theory for layer 8

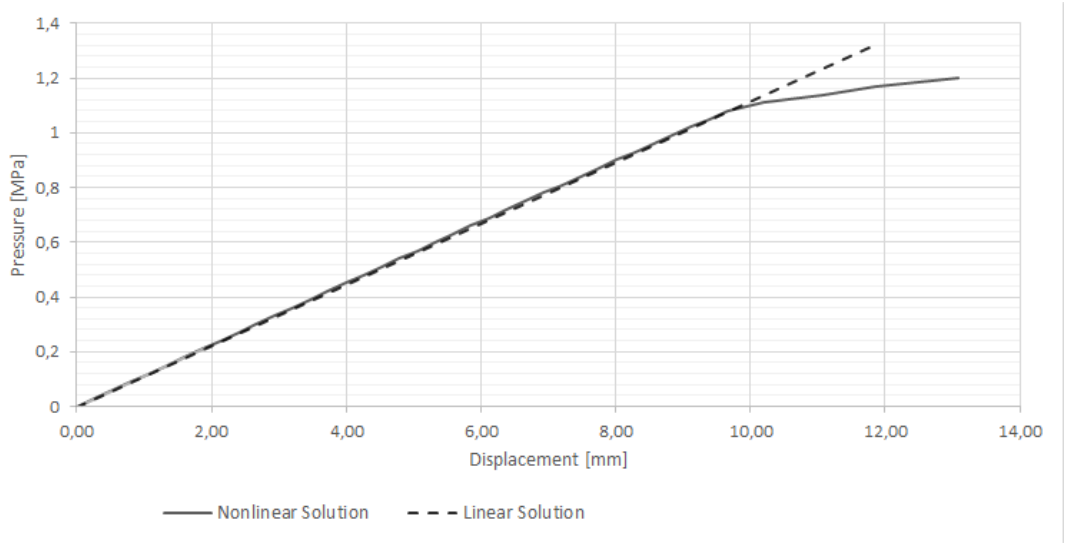

Figure 5.11: Pressure-displacement graph of $[0/90/0/90/45/\text{-}45/0]_s$ laminae at maximum displacement location, $(x,\ 100,\ 0)$ for linear and nonlinear solutions.

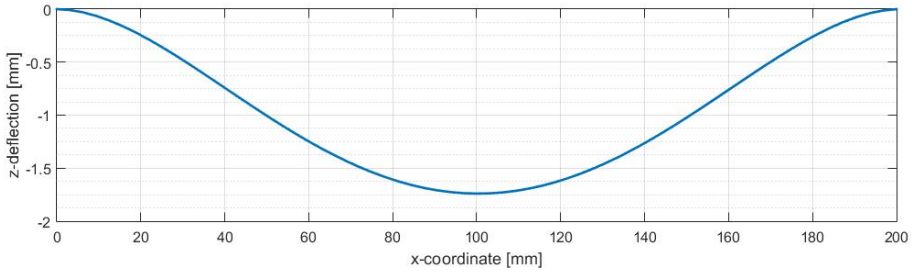

Figure 5.12: z-displacement graph of the IGA solution of the laminate $[0/90/0/90/45/\text{-}45/0]_s$ at $(x,\ 100,\ 0)$.

(bottom layer) which is the most critical layer according to the criteria. The criticality of the regions reduce from red to blue. The failure mode is predicted to be tensile failure of the matrix.

5.2.1.5 Comparison of Displacements of Laminae $[0/90/0/90/\ 0/90/0]_s$, $[45/\text{-}45/\ 45/\text{-}45/45/\text{-}45/45]_s$, $[0/90/0/90/\ 45/\text{-}45/0]_s$ and $[45/\text{-}45/45/\text{-}45]_s$ Under the Same Load

To observe the effect of stacking sequence, code is rerun with the load $0.02\,MPa$. Displacements of laminae with orientations $[0/90/0/90/0\ /90/0]_s$, $[45/\text{-}45/\ 45/\text{-}$

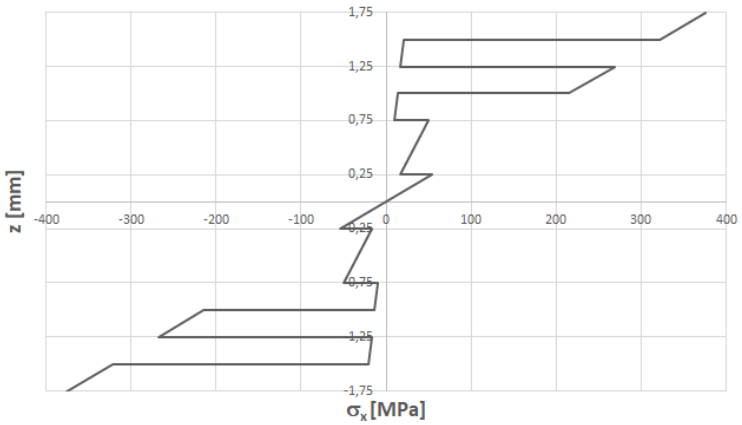

(a) σ_x

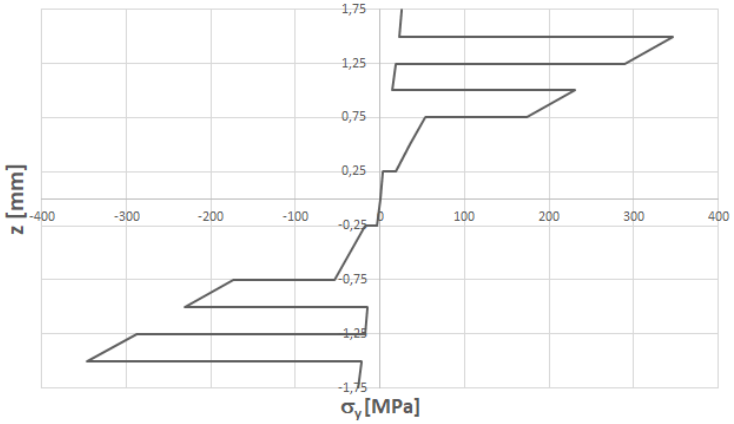

(b) σ_y

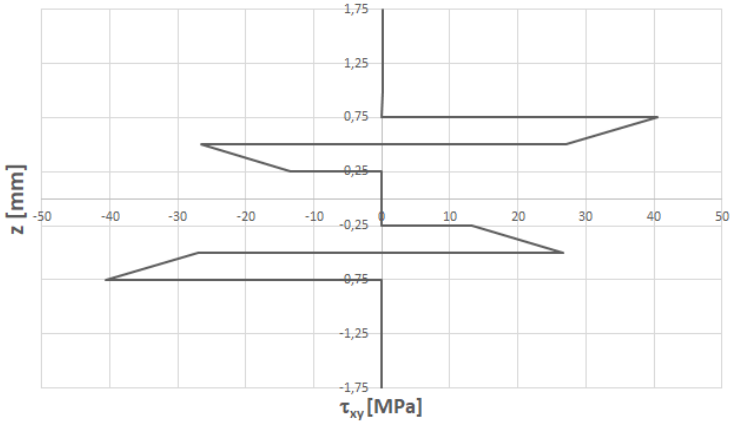

(c) τ_{xy}

Figure 5.13: Stress distribution through the thickness of fully clamped laminate $[0/90/0/90/45/\text{-}45/0]_s$.

Table 5.9: Minimum strength ratios and expected strength ratios at failure according to different failure criteria of the laminate $[0/90/0/90/45/\text{-}45/0]_s$.

	Maximum Stress	Tsai-Hill	Hoffman	Tsai-Wu	Hashin
Minimum SR	2.909	2.879	2.878	2.890	2.879
ESRF	1.011	1.000	1.000	1.004	1.000

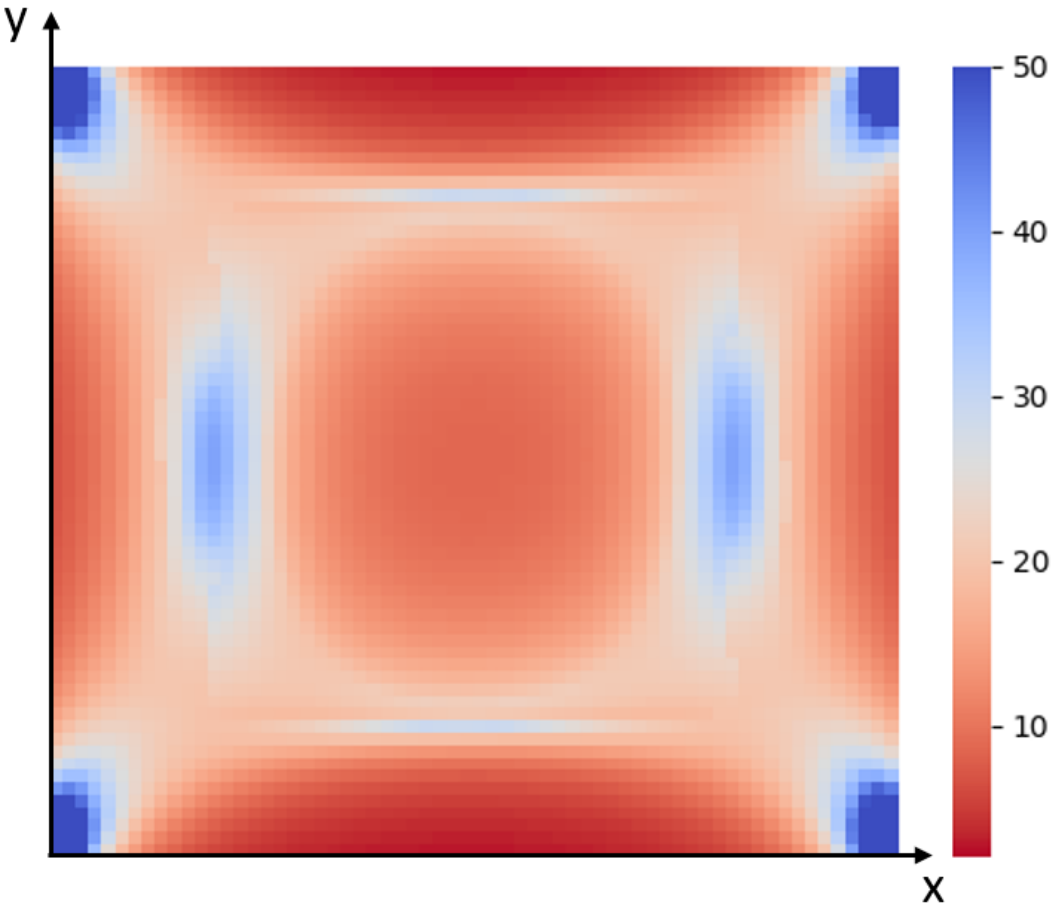

Figure 5.14: The SR distribution of the fully clamped square plate $[0/90/0/\ 90/45/\text{-}45/0]_s$ according to the Hashin criteria at layer 14.

$45/45/\text{-}45/45]_s$ and $[0/90/0/90/45/\text{-}45/0]_s$ are shown in the Figure 5.19. To examine the effect of the thickness, the displacements of the laminae $[45/\text{-}45/\ 45/\text{-}45/45/\text{-}45/45]_s$ and $[45/\text{-}45/45/\text{-}45]_s$ are compared in Figure 5.20.

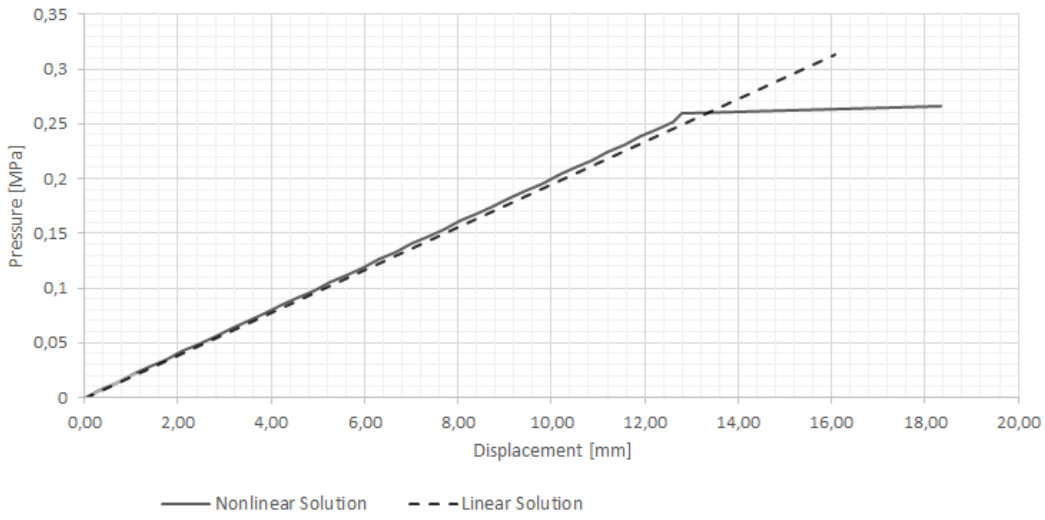

Figure 5.15: Pressure-displacement graph of $[45/\text{-}45/45/\text{-}45]_s$ laminae at maximum displacement location, $(x,\ 100,\ 0)$ for linear and nonlinear solutions.

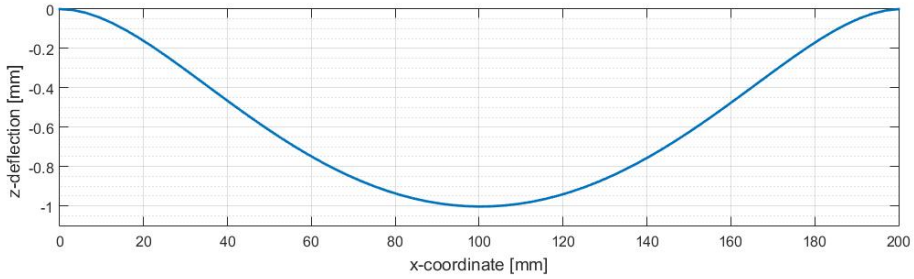

Figure 5.16: z-displacement graph of the IGA solution of the laminate $[45/\text{ -}45/45/\text{-}45]_s$ at $(x,\ 100,\ 0)$.

5.2.2 One-End Clamped Plate

This section consists of solutions of one-end clamped rectangular plate with different ply orientations under uniform loading on the top surface. Dimension of the plate is $300\,mm$ x $100\,mm$. Aforementioned, ply thickness is $0.25\,mm$ for each layer and material is carbon/epoxy with properties given in Table 5.4. The one-end clamped rectangular plate is illustrated in Figure 5.21.

The inputs to model the rectangular plate are listed in Table 5.11 and Table 5.12. After k-refinement control points are increased to 66x66 to have accurate solution on the mid-point of the surface.

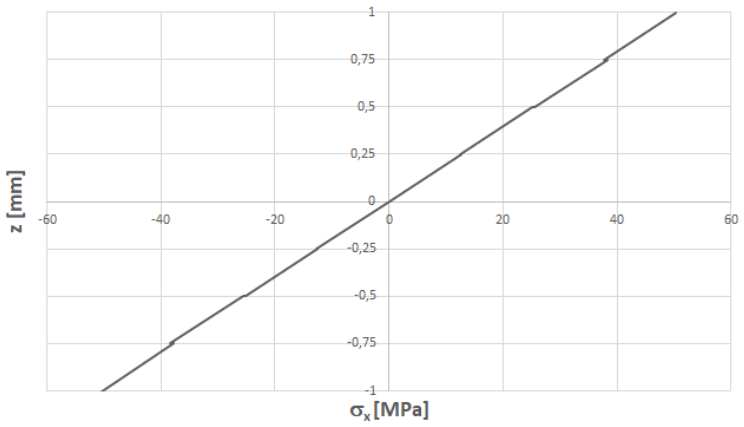

(a) σ_x

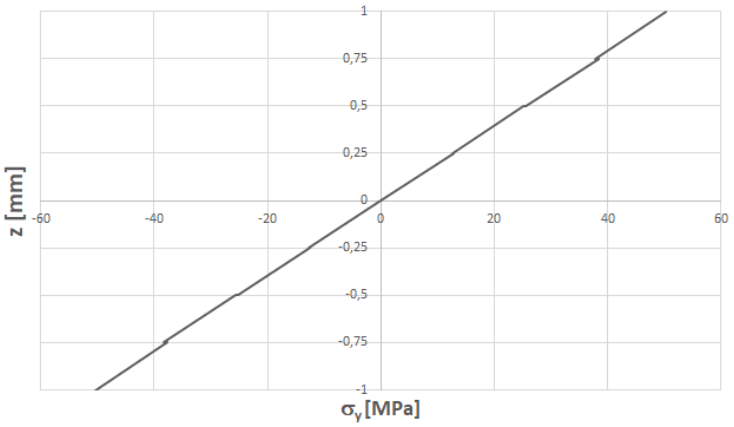

(b) σ_y

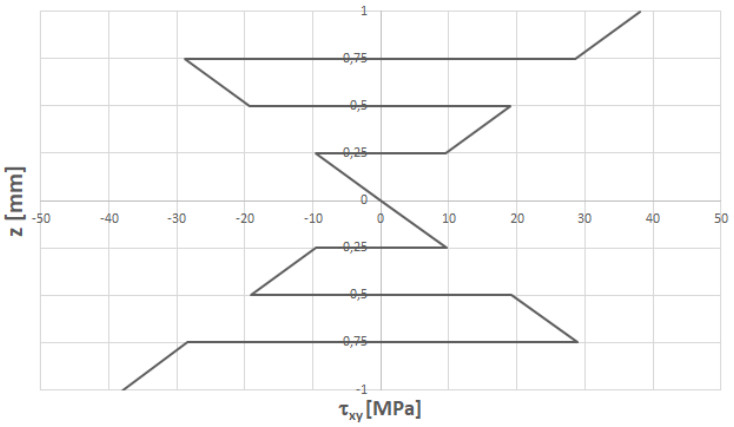

(c) τ_{xy}

Figure 5.17: Stress distribution through the thickness of fully clamped laminate $[45/\text{-}45/45/\text{-}45]_s$.

Table 5.10: Minimum strength ratios and expected strength ratios at failure according to different failure criteria of the laminate $[45/\text{-}45/45/\text{-}45]_s$.

	Maximum Stress	Tsai-Hill	Hoffman	Tsai-Wu	Hashin
Minimum SR	10.577	9.401	10.037	11.514	9.794
ESRF	1.125	1.000	1.068	1.225	1.042

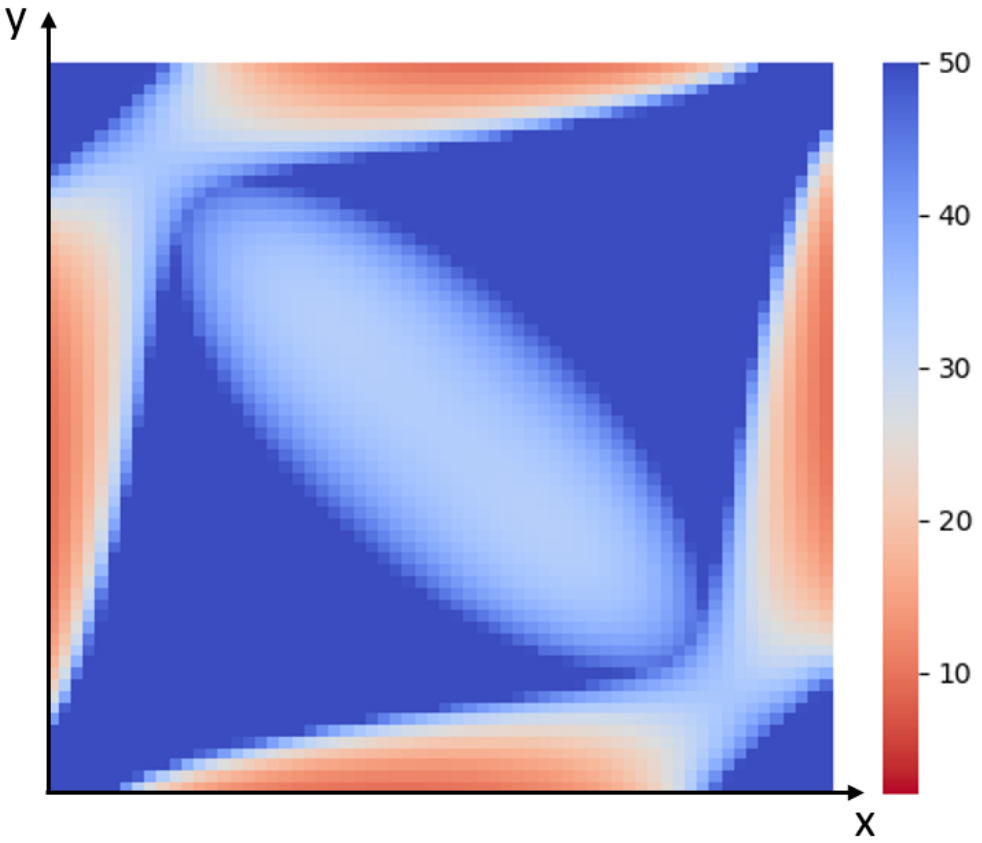

Figure 5.18: The SR distribution of the fully clamped square plate $[45/\text{-}45/\ 45/\text{-}45]_s$ according to the Hashin criteria at layer 8.

5.2.2.1 14-layer symmetric rectangular cross-ply laminate with orientation $[\mathbf{0/90/0/90/0/90/0}]_s$

Having $0.25\,mm$ layers, the total thickness of the laminate is $3.5\,mm$. Relation between pressure and displacement obtained by linear and nonlinear solutions by MSC Nastran is presented in Figure 5.22. Allowing the maximum displacement of 20% of the thickness, i.e. $0.7\,mm$, corresponding pressure $0.0002\,MPa$, is applied to the

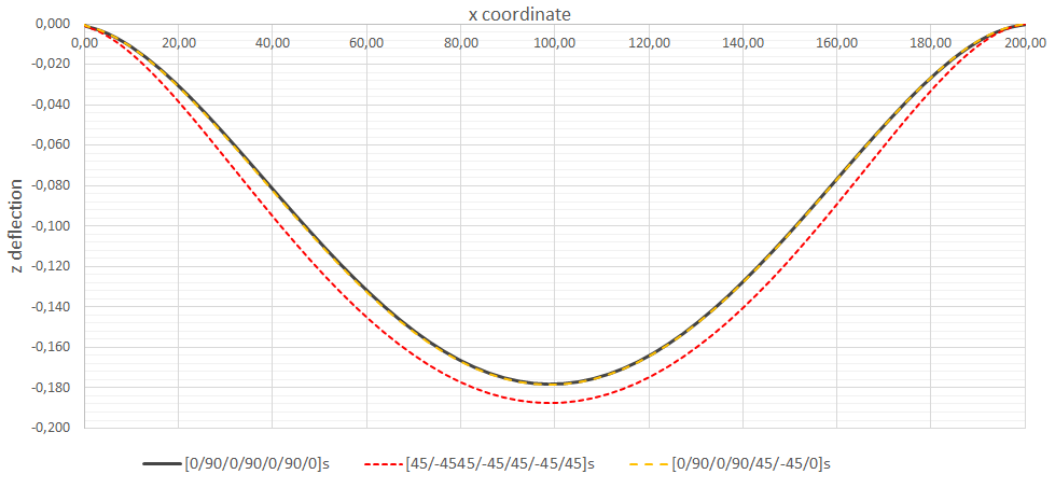

Figure 5.19: Comparison of the displacements of the fully clamped square laminae with different ply orientations under the same load.

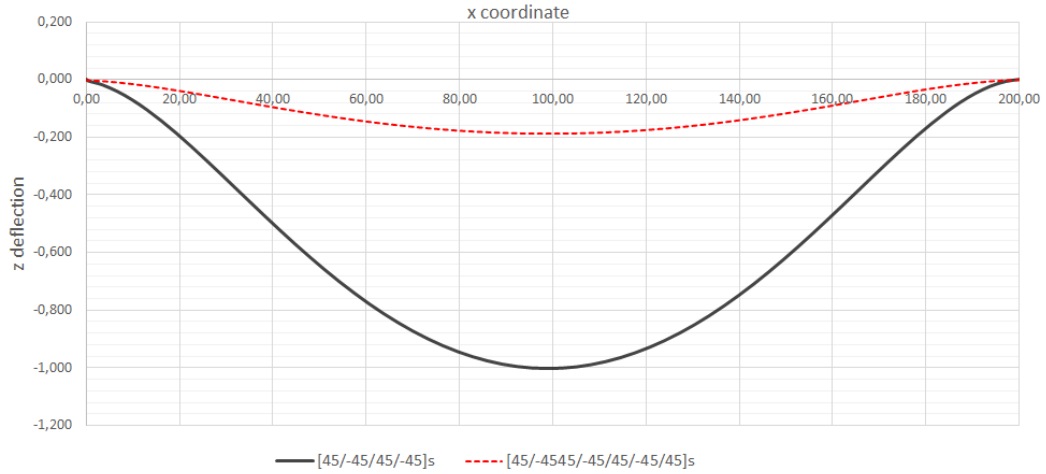

Figure 5.20: Comparison of the displacements of the fully clamped square laminae, $[45/\text{-}45/\ 45/\text{-}45/45/\text{-}45/45]_s$ and $[45/\text{-}45/45/\text{-}45]_s$, under the same load.

Table 5.11: Polynomial orders, knot vectors and control points of mid-plane of a rectangular laminate before refinement.

p	1
q	1
Ξ	0, 0, 1, 1
$\mathcal{H}$	0, 0, 1, 1

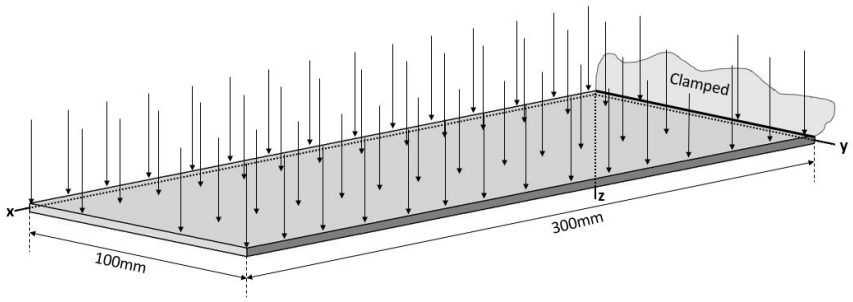

Figure 5.21: Distributed load applied to the top surface of a one-end clamped rectangular plate.

Table 5.12: Control points of mid-plane of a rectangular laminate before refinement.

Point	(x,y) $[mm]$
1	(0, 0)
2	(300, 0)
3	(0, 100)
4	(300, 100)

top surface of the laminate. The displacement of the $(x,\ 50,\ 0)$ line obtained by IGA is given in the Figure 5.23. The maximum displacement is $0.62\,mm$. Figure 5.24 shows the variation of in-plane problem stresses through the thickness where stresses have maximum values. The minimum SR for all failure criteria and expected strength ratios at failure (ESRF) according to different theories are listed in Table 5.13. The heat-map on Figure 5.25 is generated from SR values of the Hashin theory for layer 13 which is the most critical layer according to the criteria. The transition from red to blue express the transition from critic to safe. The failure mode is predicted to be tensile failure of the matrix.

Table 5.13: Minimum strength ratios and expected strength ratios at failure according to different failure criteria of the laminate $[0/90/0/90/0/90\ /0\ ]_s$.

	Maximum Stress	Tsai-Hill	Hoffman	Tsai-Wu	Hashin
Minimum SR	186.600	186.419	187.456	188.345	186.403
ESRF	1.001	1.000	1.006	1.010	1.000

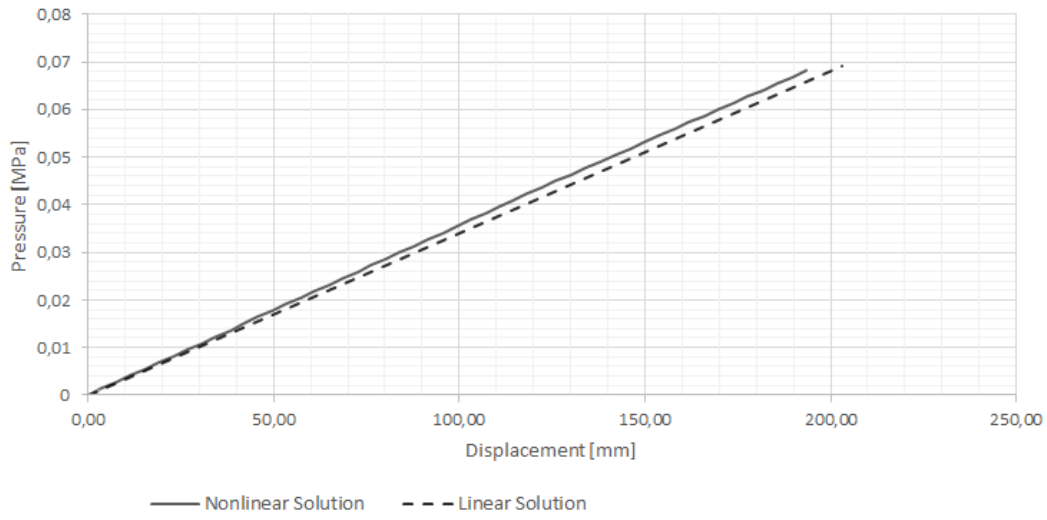

Figure 5.22: Pressure-displacement graph of $[0/90/0/90/0/90/0\,]_s$ laminae at maximum displacement location, $(x,\ 50,\ 0)$ for linear and nonlinear solutions.

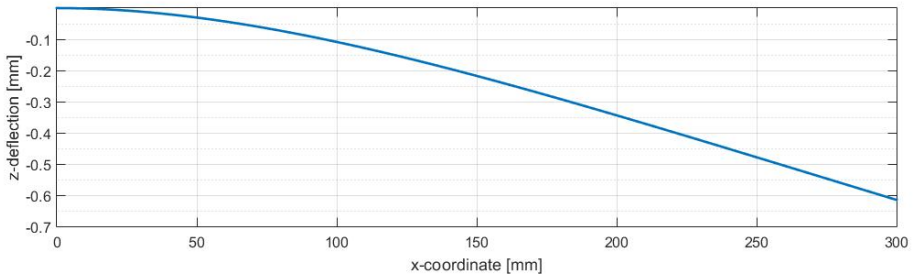

Figure 5.23: z-displacement graph of the IGA solution of the laminate $[0/90/0/90/0/90/0\,]_s$ at $(x,\ 50,\ 0)$.

5.2.2.2 14-layer symmetric rectangular angle-ply laminate with orientation $[45/-45/45/-45/45/-45/45]_s$

The 14-layer plate has the total thickness of $3.5\,mm$. The linear and nonlinear pressure-displacement graph obtained by MSC Nastran is shown in the Figure 5.26. For for maximum displacement of 20% of the thickness, i.e. $0.7\,mm$, corresponding pressure $70\,Pa$, is applied to the top surface. The displacement of the $(x,\ 50,\ 0)$ line is given in the Figure 5.27 for IGA solution. The maximum displacement is $0.71\,mm$. The variation of in-plane stresses through the thickness is presented in Figure 5.28for the elements with highest stresses. Table 5.14 shows the minimum SR for all failure

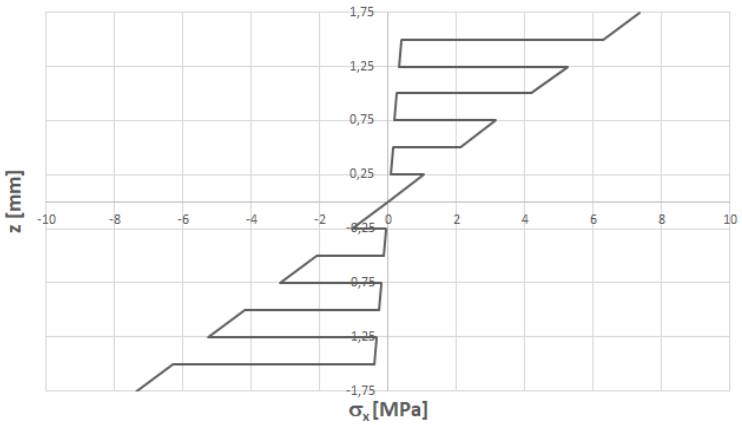

(a) σ_x

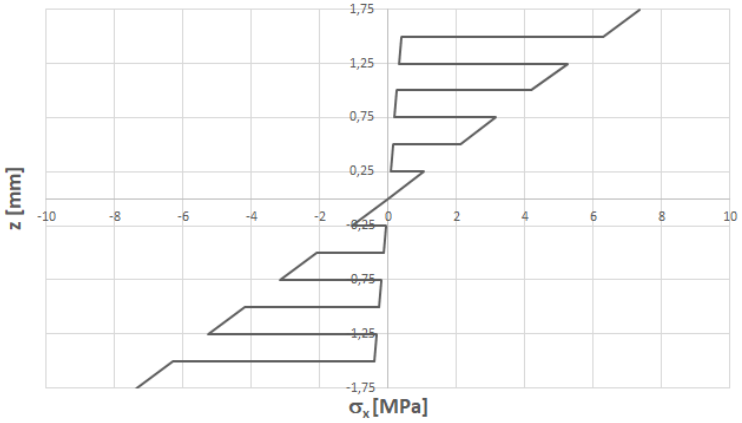

(b) σ_y

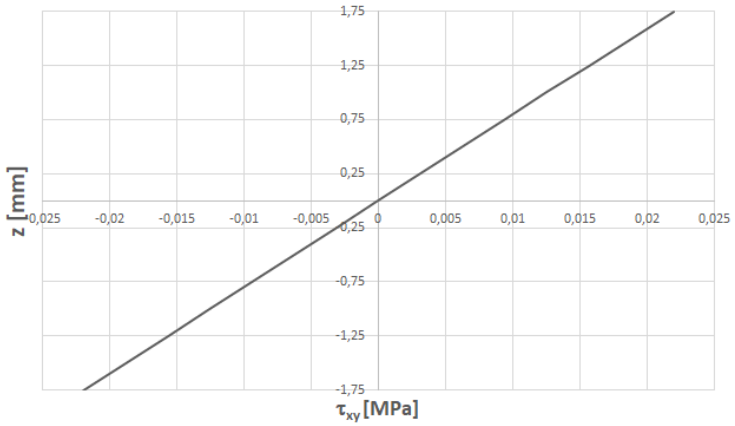

(c) τ_{xy}

Figure 5.24: Stress distribution through the thickness of one-end clamped laminate $[0/90/0/90/0/90\ /0\ ]_s$.

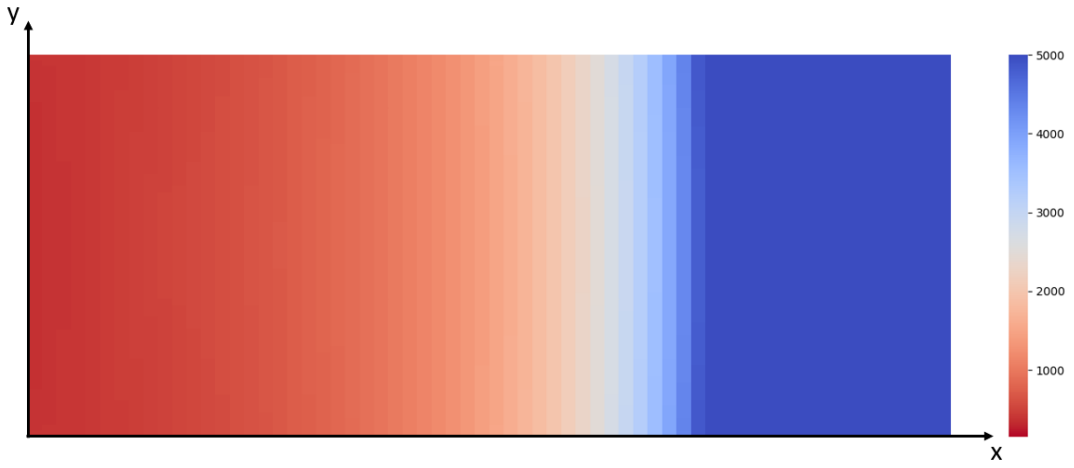

Figure 5.25: The SR distribution of the one-end clamped plate $[0/90/0/90/0/\ 90/0]_s$ according to the Hashin criteria at layer 13.

criteria and expected strength ratios at failure (ESRF) according to different theories. The heat-map in Figure 5.29 is generated from SR values of Hashin theory at the most critical layer, which is layer 7. Red regions are more critical regions (low SR values), whereas blue regions represent the safer regions (high SR values). The failure mode is predicted to be compressive failure of the matrix.

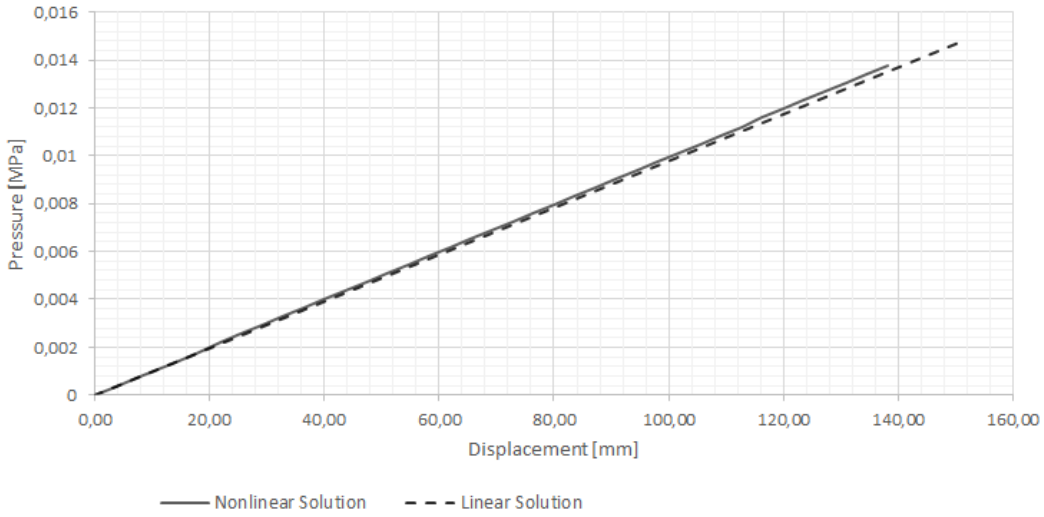

Figure 5.26: Pressure-displacement graph of $[45/\text{-}45/45/\text{-}45/45/\text{-}45/45]_s$ laminae at maximum displacement location, $(x,\ 50,\ 0)$ for linear and nonlinear solutions.

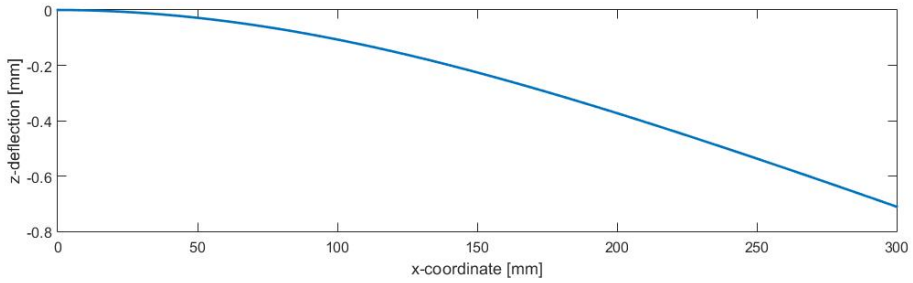

Figure 5.27: z-displacement graph of the IGA solution of the laminate $[45/\text{-}45/45/\text{-}45/45/\text{-}45/45]_s$ at $(x,\ 50,\ 0)$.

Table 5.14: Minimum strength ratios and expected strength ratios at failure according to different failure criteria of the laminate $[45/\text{-}45/45/\text{-}45/45/\text{-}45/45]_s$.

	Maximum Stress	Tsai-Hill	Hoffman	Tsai-Wu	Hashin
Minimum SR	236.387	198.707	186.763	186.344	204.176
ESRF	1.269	1.066	1.002	1.000	1.096

5.2.2.3 14-layer symmetric rectangular angle-ply laminate with orientation $[\mathbf{0/90/0/90/45/\text{-}45/0}]_s$

Each layer having $0.25\,mm$ layers, the total thickness of the laminate is $3.5\,mm$. The pressure-displacement graph obtained by MSC Nastran results for linear and nonlinear solutions is shown in the Figure 5.30. Assuming linear solutions agrees well with the nonlinear solution for maximum displacement of 20% of the thickness, i.e. $0.7\,mm$, corresponding pressure $0.0002\,MPa$, is applied to the top surface. Figure 5.31 shows the displacement of the $(x,\ 50,\ 0)$ for IGA solution. The maximum displacement obtained by code is $0.65\,mm$. Figure 5.32 shows the variation of problem stresses through the thickness where stresses have maximum values. In Table 5.15, the minimum SR and expected strength ratios at failure (ESRF) according to different theories are listed. The heat-map on Figure 5.33 is generated from SR values of the Hashin theory for layer 13 which is the most critical layer according to the criteria. Red regions are more critical regions, whereas blue regions represent the safer regions. The failure mode is predicted to be tensile failure of the matrix.

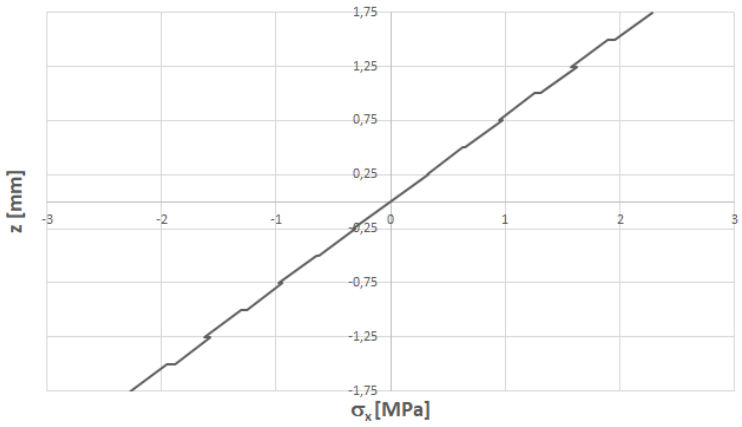

(a) σ_x

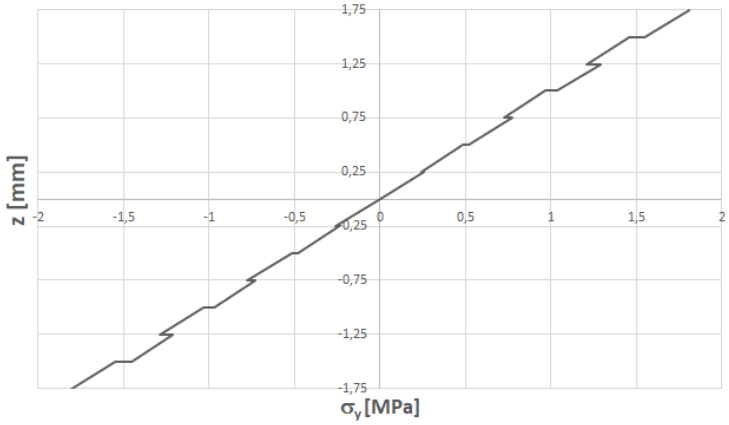

(b) σ_y

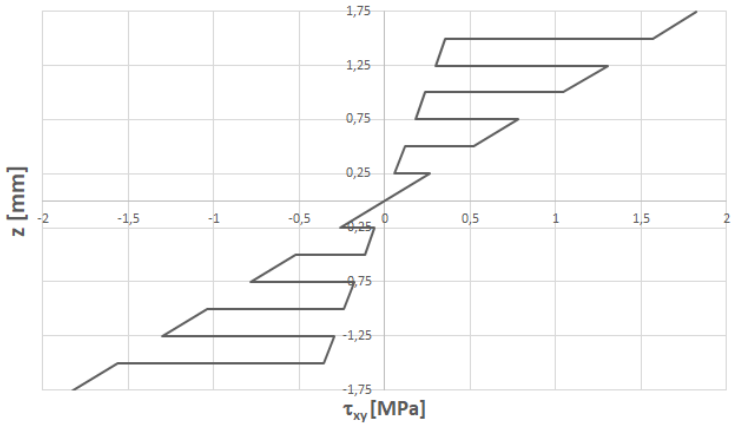

(c) τ_{xy}

Figure 5.28: Stress distribution through the thickness of one-end clamped laminate $[45/\text{-}45/45/\text{-}45/45/\text{-}45/45]_s$.

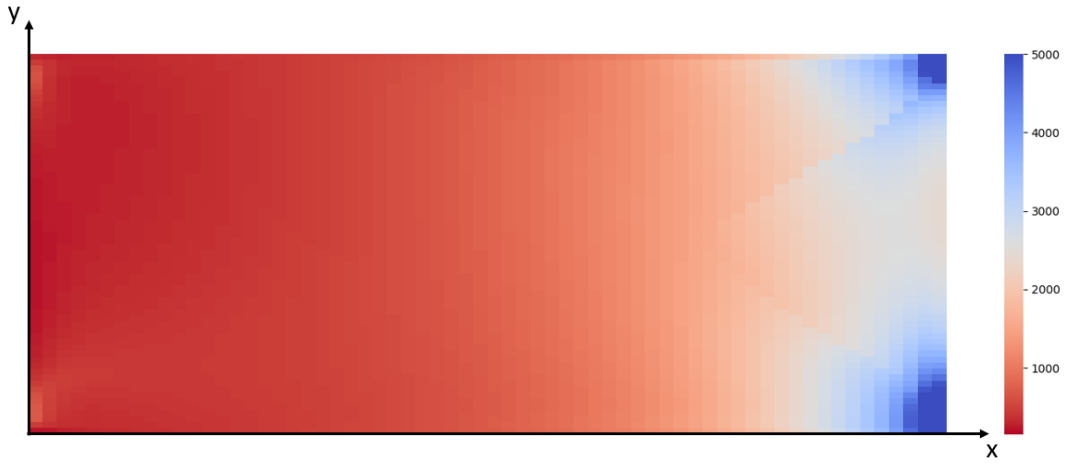

Figure 5.29: The SR distribution of the one-end clamped plate $[45/\text{-}45/45/\text{-}45/45/\text{-}45/45]_s$ according to the Hashin criteria at layer 7.

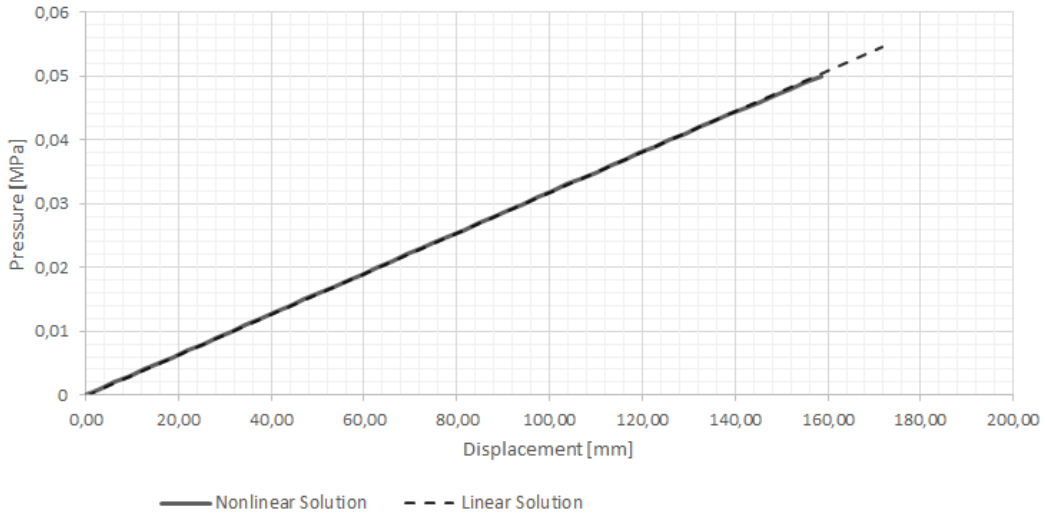

Figure 5.30: Pressure-displacement graph of $[0/90/0/\ 90/45/\text{-}45/0]_s$ laminae at maximum displacement location, $(x,\ 50,\ 0)$ for linear and nonlinear solutions.

5.2.2.4 Comparison of Displacements of Laminae $[0/90/0/90/0\ /90/0]_s$, $[45/\text{-}45/\ 45/\text{-}45/45/\text{-}45/45]_s$ and $[0/90/0/90/\ 45/\text{-}45/0]_s$ Under the Same Load

The analyses are rerun for the one-end clamped plates by applying the same load of $70\ Pa$. Comparison of the resulting displacements are shown in the Figure 5.34.

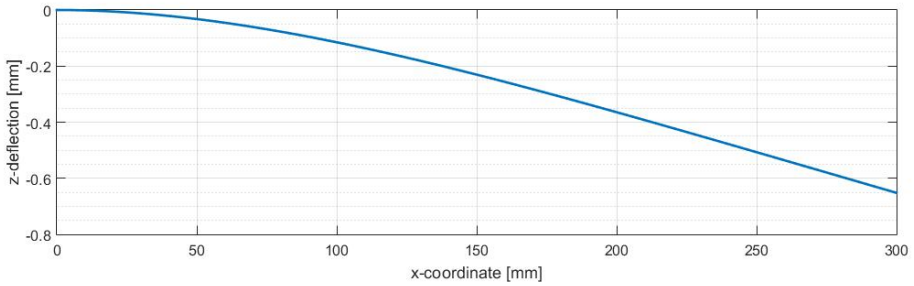

Figure 5.31: z-displacement graph of the IGA solution of the laminate $[0/90/0/90/45/\text{-}45/0]_s$ at $(x,\ 50,\ 0)$.

Table 5.15: Minimum strength ratios and expected strength ratios at failure according to different failure criteria of the laminate$[0/90/0/90/45/\text{-}45/0]_s$.

	Maximum Stress	Tsai-Hill	Hoffman	Tsai-Wu	Hashin
Minimum SR	172.330	172.119	173.014	173.805	172.105
ESRF	1.001	1.000	1.005	1.010	1.000

5.2.3 Two-Ends Clamped Plate

This section consists of solutions of two-ends clamped rectangular plate with different ply orientations under uniform loading on the top surface. Dimension of the plate is $300\,mm$ x $100\,mm$. Aforementioned, ply thickness is $0.25\,mm$ for each layer and material is carbon/epoxy with properties given in Table 5.4. The one-end clamped rectangular plate is illustrated in Figure 5.35.

The inputs to model the rectangular plate are listed in Table 5.11, which are same as the one-end clamped plate. After k-refinement control points are increased to 66x66 to have accurate solution on the mid-point of the surface.

5.2.3.1 14-layer symmetric rectangular cross-ply laminate with orientation $[0/90/0/90/0/90/0]_s$

14-layer laminate having $0.25\,mm$ layers, the total thickness is $3.5\,mm$. According to the linear and nonlinear solutions, the obtained pressure-displacement graph by

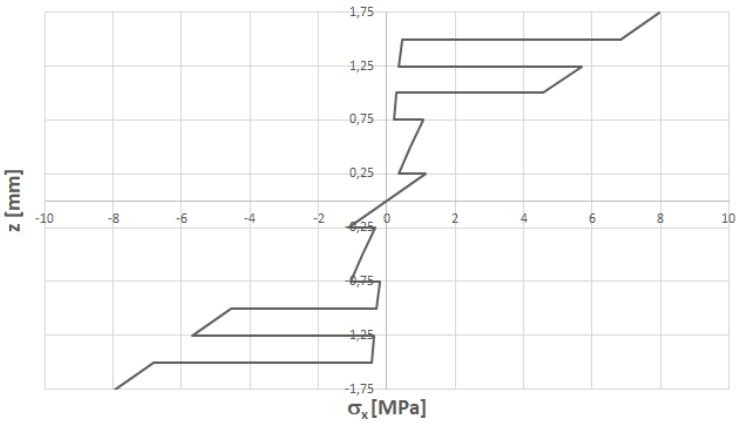

(a) σ_x

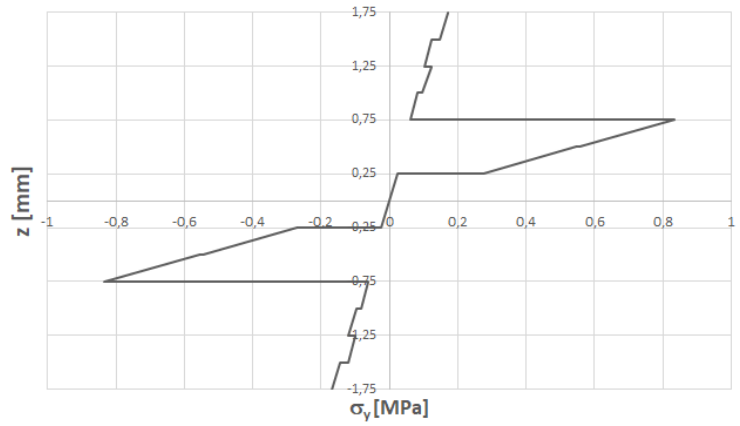

(b) σ_y

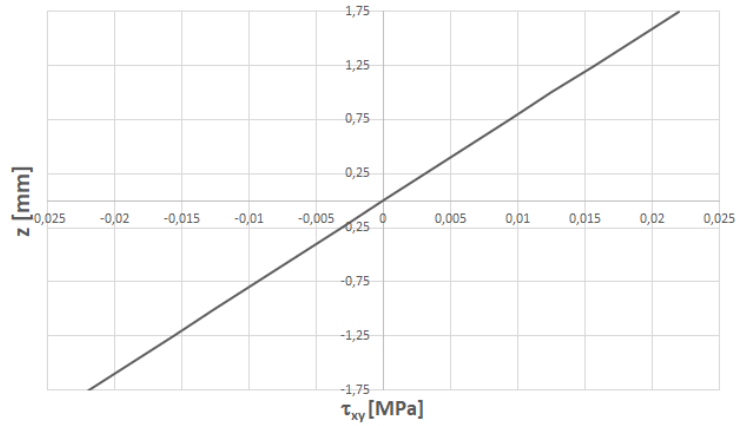

(c) τ_{xy}

Figure 5.32: Stress distribution through the thickness of one-end clamped laminate $[0/90/0/90/45/\text{-}45/0]_s$.

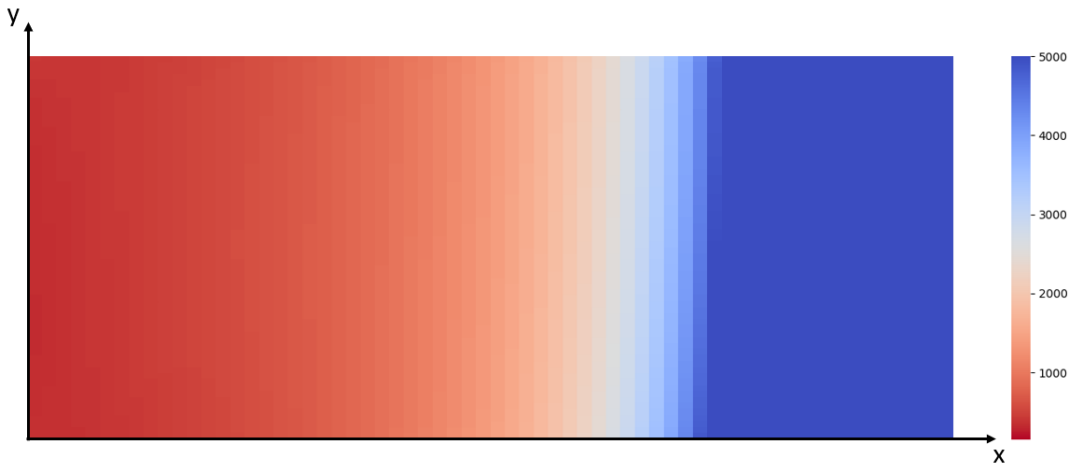

Figure 5.33: The SR distribution of the one-end clamped plate $[0/90/0/90/45/$ -$45/0]_s$ according to the Hashin criteria at layer 13.

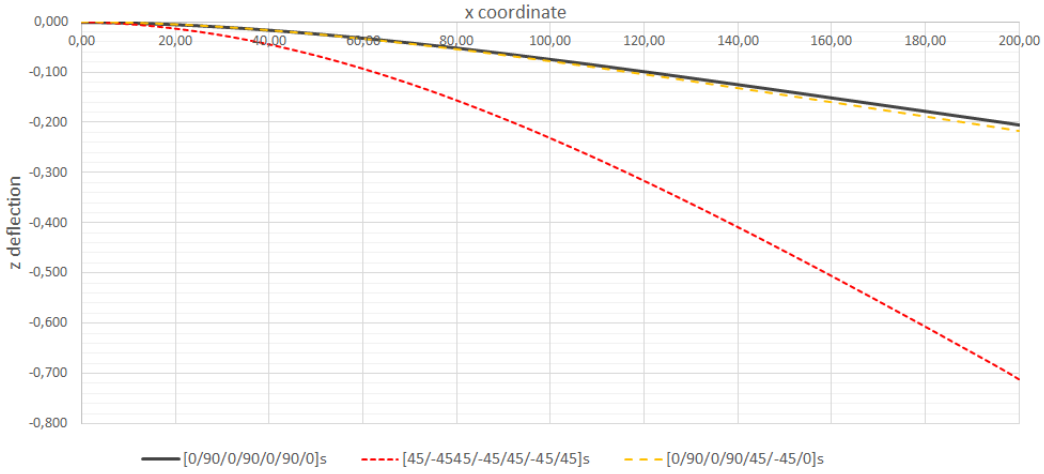

Figure 5.34: Comparison of the displacements of the one-end clamped rectangular laminae under the same load.

MSC Nastran results is shown in the Figure 5.36. For maximum displacement less than 20% of the thickness, it is assumed that the solution is in linear region. Thus, pressure resulting $0.7\,mm$ maximum displacement, $0.0113\,MPa$, is applied to the top surface of the plate. For the results obtained by IGA, displacement of the $(x,\ 50,\ 0)$ line is given in the Figure 5.37. The maximum displacement is $0.7\,mm$. Figure 5.38 shows the variation of in-plane problem stresses through the thickness where they have maximum values at an element. The minimum SR for all failure criteria and expected strength ratios at failure (ESRF) according to different theories are listed in

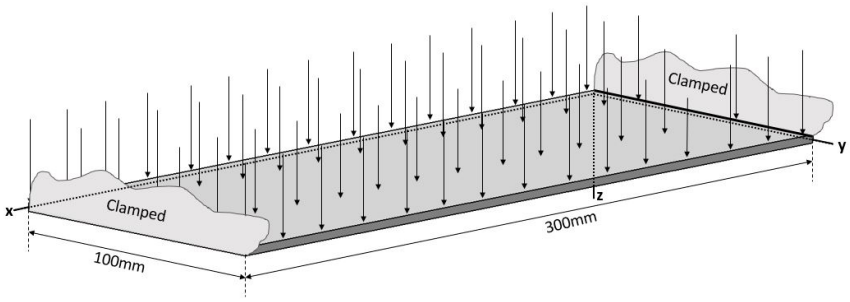

Figure 5.35: Distributed load applied to the top surface of a two-ends clamped rectangular plate.

Table 5.16. The heat-map on Figure 5.39 is generated from SR values of the Hashin theory for layer 13 which is the most critical layer according to the criteria. Color distribution from red to blue represents the transition from critical to safe. The failure mode is predicted to be tensile failure of the matrix.

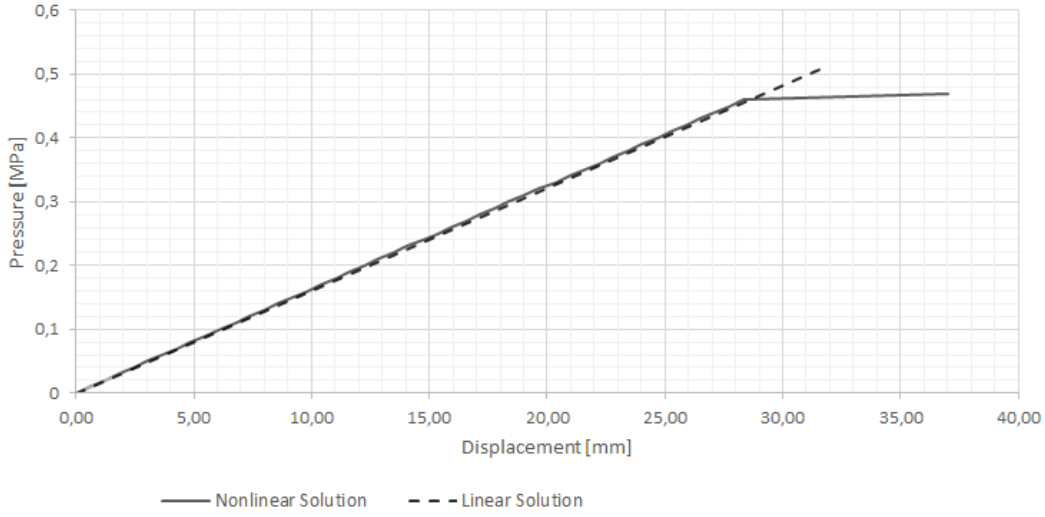

Figure 5.36: Pressure-displacement graph of $[0/90/0/90/\ 0/90/0\ ]_s$ laminae at maximum displacement location, $(x,\ 50,\ 0)$ for linear and nonlinear solutions.

5.2.3.2 14-layer symmetric rectangular angle-ply laminate with orientation $[45/\text{-}45/45/\text{-}45/45/\text{-}45/45]_s$

The total thickness of the 14-layer laminate is $3.5\,mm$. Figure 5.40 shows the applied pressure-displacement graph obtained by MSC Nastran. For maximum displacement

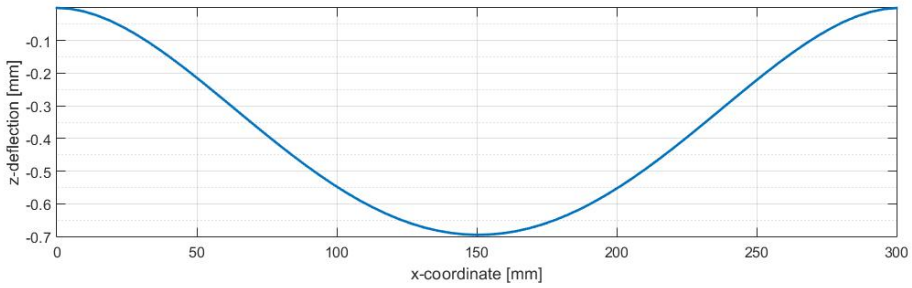

Figure 5.37: z-displacement graph of the IGA solution of the laminate $[0/90/0/90/0/90/0]_s$ at $(x,\ 50,\ 0)$.

Table 5.16: Minimum strength ratios and expected strength ratios at failure according to different failure criteria of the laminate $[0/90/0/90/0/90/0]_s$.

	Maximum Stress	Tsai-Hill	Hoffman	Tsai-Wu	Hashin
Minimum SR	21.756	21.606	21.631	21.730	21.604
ESRF	1.007	1.000	1.001	1.006	1.000

of 20% of the thickness, i.e. $0.7\,mm$, corresponding pressure $0.004\,MPa$, is applied to the top surface. Figure 5.41 presents the displacement obtained by IGA of the $(x,\ 50,\ 0)$ line. The maximum displacement is $0.69\,mm$. The variation of in-plane problem stresses through the thickness are shown in Figure 5.42 where stresses have maximum values. The minimum SR for all failure criteria and expected strength ratios at failure (ESRF) according to different theories are listed in Table 5.17. The heat-map generated from SR values of the Hashin theory for layer 14 (bottom layer) which is the most critical layer according to the criteria is shown in Figure 5.43. Red areas are more critical regions, whereas blue areas are safer regions. The failure mode is predicted to be tensile failure of the matrix.

Table 5.17: Minimum strength ratios and expected strength ratios at failure according to different failure criteria of the laminate $[45/\text{-}45/45/\text{-}45/45/\text{-}45/45]_s$.

	Maximum Stress	Tsai-Hill	Hoffman	Tsai-Wu	Hashin
Minimum SR	28.288	25.200	26.896	27.948	26.210
ESRF	1.123	1.000	1.067	1.109	1.040

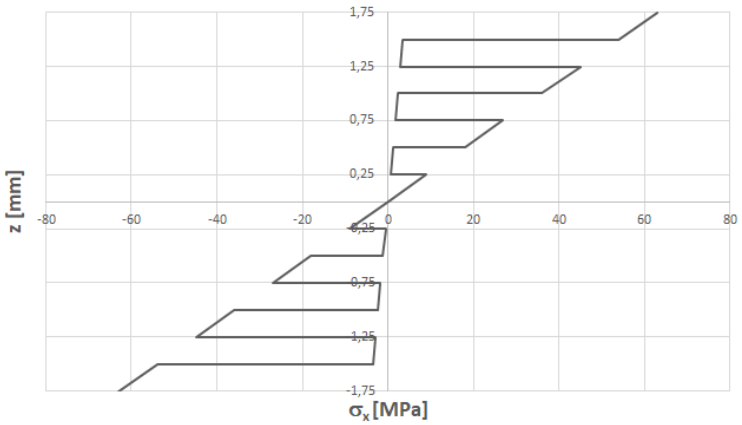

(a) σ_x

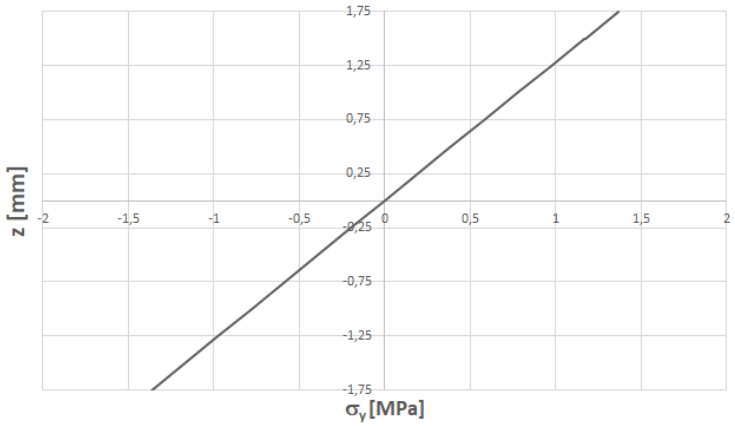

(b) σ_y

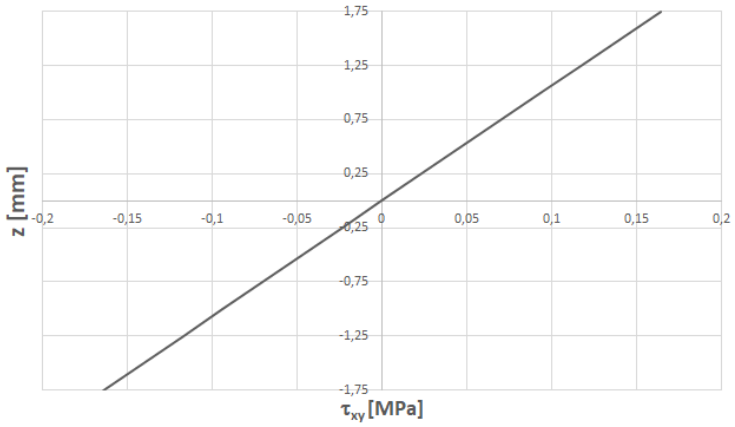

(c) τ_{xy}

Figure 5.38: Stress distribution through the thickness of two-ends clamped laminate $[0/90/0/90/0/90/0]_s$.

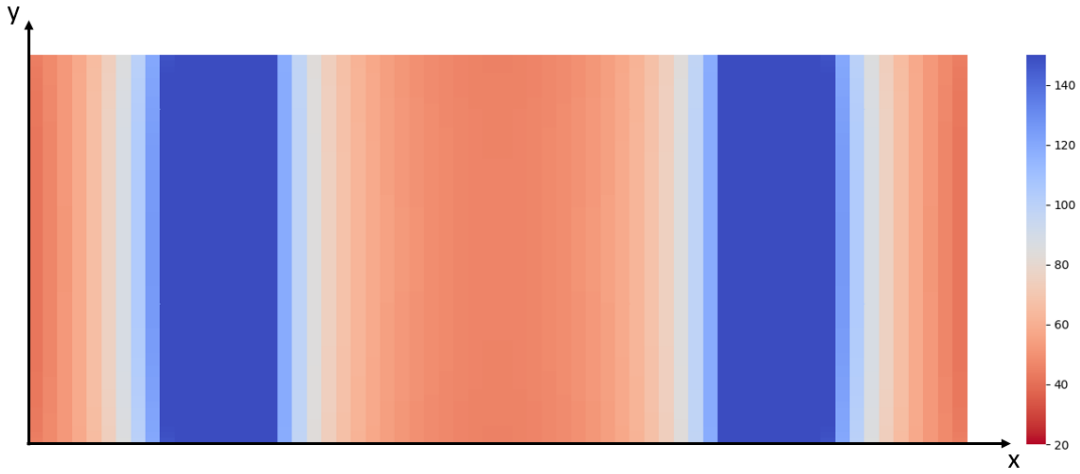

Figure 5.39: The SR distribution of the two-ends clamped plate $[0/90/0/90/0/90/0]_s$ according to the Hashin criteria at layer 13.

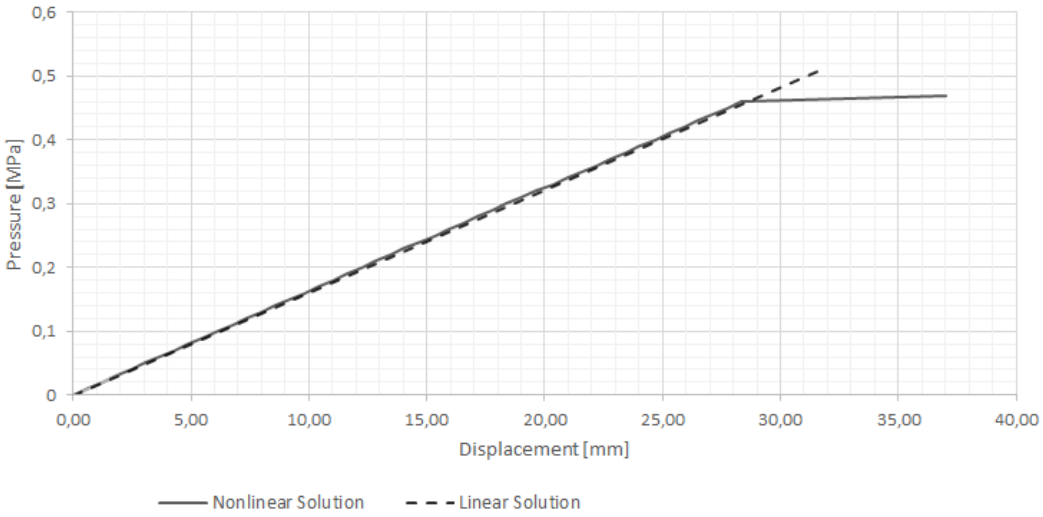

Figure 5.40: Pressure-displacement graph of $[45/\text{-}45/45/\text{-}45/45/\text{-}45/45]_s$ laminae at maximum displacement location, $(x,\ 50,\ 0)$ for linear and nonlinear solutions.

5.2.3.3 14-layer symmetric rectangular angle-ply laminate with orientation $[0/90/0/90/45/\text{-}45/0]_s$

Having $0.25\,mm$ layers, the total thickness of the plate is $3.5\,mm$. The linear and nonlinear pressure-displacement graph obtained by MSC Nastran results is shown in the Figure 5.44. Assuming linear solutions agrees well with the nonlinear solu-

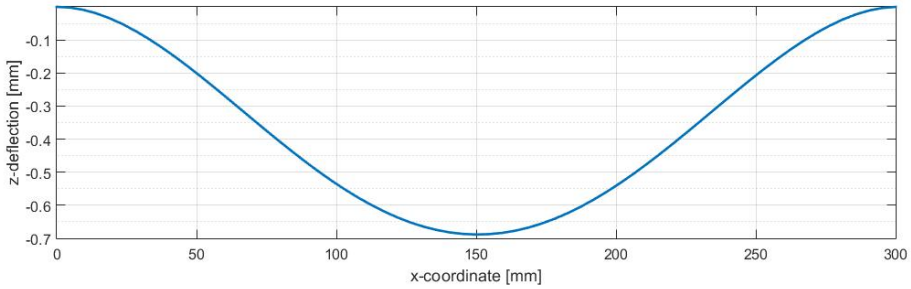

Figure 5.41: z-displacement graph of the IGA solution of the laminate [45/-45/45/-45/45/-45/45]$_s$ at $(x,\ 50,\ 0)$.

tion for maximum displacement of 20% of the thickness, i.e. $0.7\,mm$, corresponding pressure $0.0106\,MPa$, is applied to the top surface of the plate. For the results obtained by IGA code, displacement of the $(x,\ 50,\ 0)$ line is given in the Figure 5.45. The maximum displacement is $0.69\,mm$. Figure 5.46 shows the variation of in-plane problem stresses through the thickness where stresses have maximum values. Table 5.18 shows the comparison of minimum SR and expected strength ratios at failure (ESRF) for different criteria. The heat-map on Figure 5.47 is generated from SR values of the Hashin theory for layer 13 which is the most critical layer according to the criteria. The transition from red to blue represents the transition from critical to safe. The failure mode is predicted to be tensile failure of the matrix.

Table 5.18: Minimum strength ratios and expected strength ratios at failure according to different failure criteria of the laminate [0/90/0/90/45/-45/0]$_s$.

	Maximum Stress	Tsai-Hill	Hoffman	Tsai-Wu	Hashin
Minimum SR	21.576	21.396	21.405	21.489	21.395
ESRF	1.008	1.000	1.000	1.004	1.000

5.2.3.4 Comparison of Displacements of Laminae [0/90/0/90/0 /90/0]$_s$, [45/-45/ 45/-45/45/-45/45]$_s$ and [0/90/0/90/ 45/-45/0]$_s$ Under the Same Load

To observe the effect of stacking sequence, displacements of four two-ends clamped laminae with different orientations under $0.004\,MPa$ are shown in the Figure 5.48.

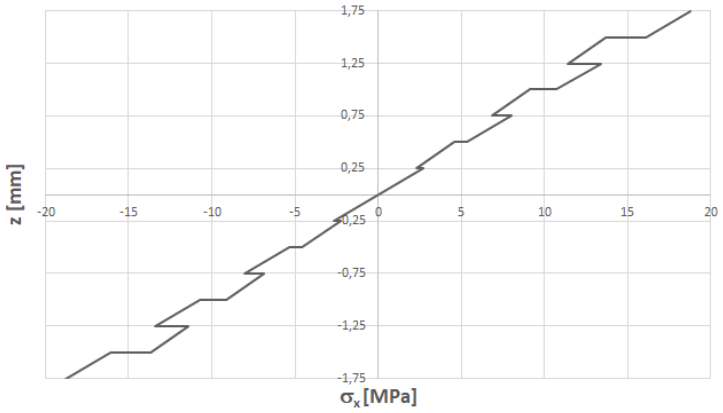

(a) σ_x

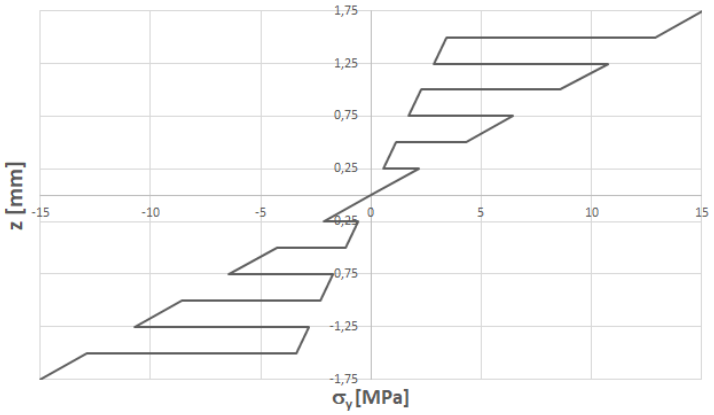

(b) σ_y

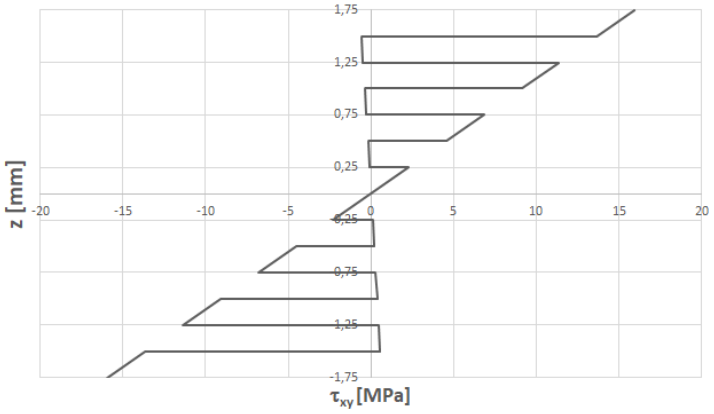

(c) τ_{xy}

Figure 5.42: Stress distribution through the thickness of two-ends clamped laminate $[45/\text{-}45/45/\text{-}45/45/\text{-}45/45]_s$.

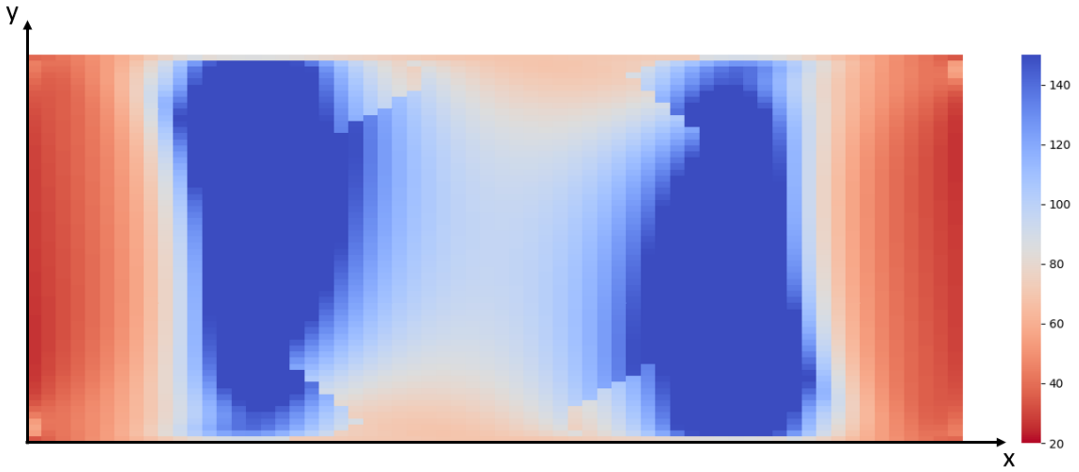

Figure 5.43: The SR distribution of the two-ends clamped plate $[45/\text{-}45/45/\text{-}45/45/\text{-}45/45]_s$ according to the Hashin criteria at layer 14.

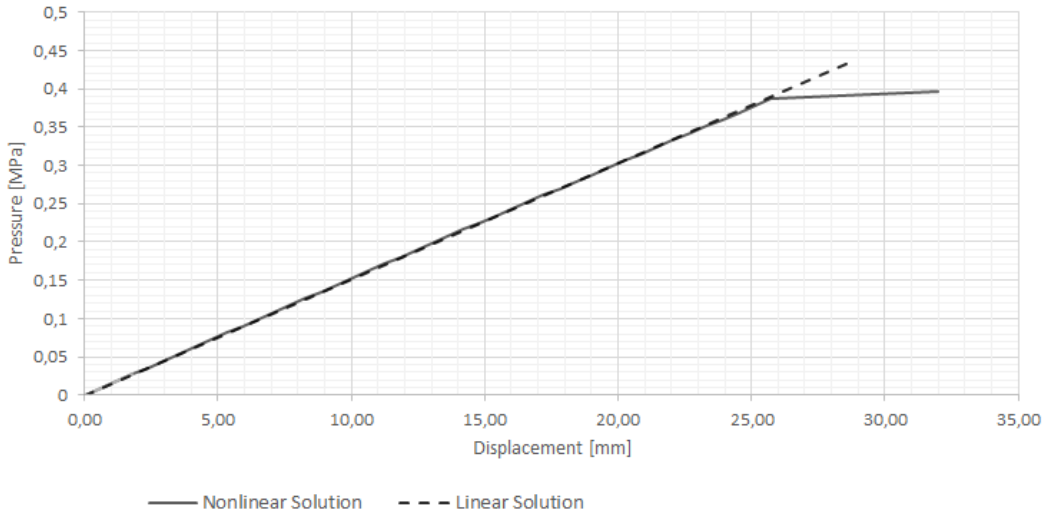

Figure 5.44: Pressure-displacement graph of $[0/90/0/90/45/\text{-}45/0]_s$ laminae at maximum displacement location, $(x,\ 50,\ 0)$ for linear and nonlinear solutions.

5.3 Discussion of Numerical Examples

Table 5.19 summarizes the numerical examples. In this table, names of the examples are abbreviated as "FC 1" for example in Section 5.2.1.1, "FC 2" for example in Section 5.2.1.2, "FC 3" for example in Section 5.2.1.3, "FC 4" for example in Section 5.2.1.4, "OC 1" for example in Section 5.2.2.1, "OC 2" for example in Section 5.2.2.2,

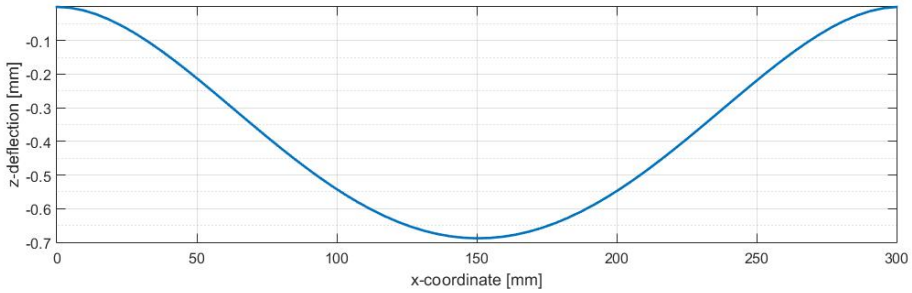

Figure 5.45: z-displacement graph of the IGA solution of the laminate $[0/90/0/90/45/\text{-}45/0]_s$ at $(x,\ 50,\ 0)$.

"OC 3" for example in Section 5.2.2.3, "TC 1" for example in Section 5.2.3.1, "TC 2" for example in Section 5.2.3.2 and "TC 3" for example in Section 5.2.3.3. "t", "Exp" "Disp" and "Pres" stand for the total thickness of laminate, expected, displacement and pressure, respectively. Expected failure modes are abbreviated as tensile failure of fiber, "TF"; compressive failure of fiber, "CF"; tensile failure of matrix, "TM"; and compressive failure of matrix, "CM". Similarly, failure criteria are abbreviated as maximum stress, "MS"; Tsai-Hill, "T-H"; Hoffman, "Hof"; Tsai-Wu, "T-W"; and Hashin, "Has".

In example in Section 5.2.1.1, the fully clamped plate with orientation $[0/90/0/90/0/90/0]_s$ has the most critical layer is the bottom layer with 0° orientation. Therefore, the most critical regions for the plate are near the boundaries at $y = 0$ and $y = 200$. Noting that z-axis is at the symmetry plane and pointing to the bottom of the plate, stress distribution in x-direction has negative values on the layers above the symmetry plane and positive values on the layers below the symmetry plane. It is an expected result since there is a pressure loading on the top of the plate and top layers should be in compression whereas bottom layers should be in tension. In addition, layers of the laminate can be clearly seen from the in-plane normal stress distributions through the thickness for this example. In the laminate since the load is mainly carried by fibers and stresses are low at y-direction and high at x-direction for the 0° plies, whereas low at x-direction and high at y-direction for the 90° plies.

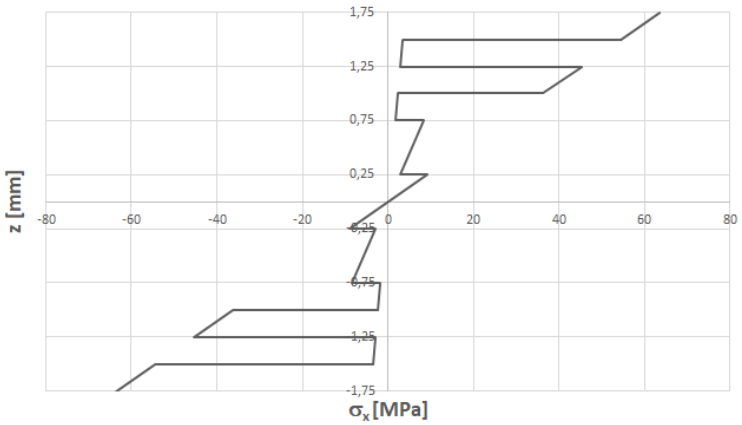

(a) σ_x

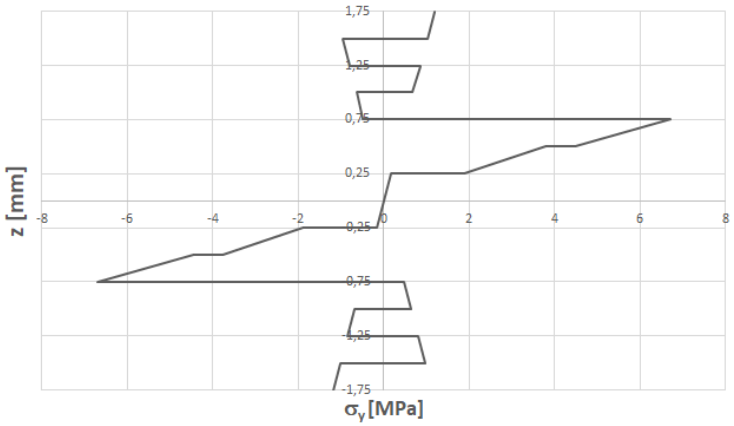

(b) σ_y

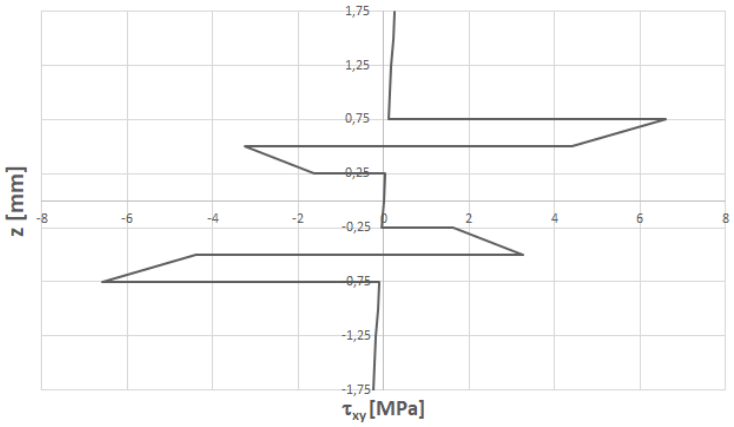

(c) τ_{xy}

Figure 5.46: Stress distribution through the thickness of two-ends clamped laminate $[0/90/0/90/45/\text{-}45/0]_s$.

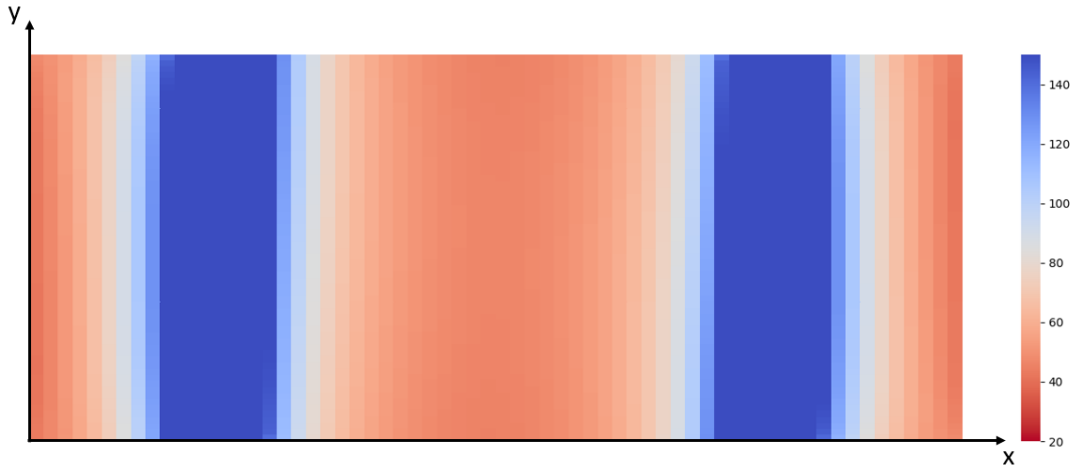

Figure 5.47: The SR distribution of the two-ends clamped plate $[0/90/0/90/\ 45/$ $-45/0]_s$ according to the Hashin criteria at layer 13.

In example in Section 5.2.1.2, the fully clamped plate with orientation $[45/\text{-}45/\ 45/$ $-45/45/\text{-}45/45]_s$ is examined. The most critical layer is the bottom layer with 45° orientation. Different than the cross-ply laminate in the first example, the safest regions for the layer are in the diagonal where 45° plies lie. While in-plane normal stresses are compressive at the top and tensile at the bottom as expected, layers are distinguishable in in-plane shear stress distribution due to fiber orientation.

For the example in Section 5.2.1.3, the fully clamped plate with orientation $[0/90/0/90/45$ $/\text{-}45/0]_s$,similar to the cross-ply laminate in the first example, the failure is at the bottom layer even though having $\pm 45°$ plies. The critical layer might change if the $\pm 45°$ plies moved away from the symmetry axis of the plate. While effect of these plies can be seen in the stress distributions through the thickness (having lower in-plane normal stresses and higher in-plane shear stresses), it is not obvious when maximum displacement under the same load or critical regions distribution are considered.

In example in Section 5.2.1.4, the fully clamped plate with orientation $[45/\text{-}45/45/\ \text{-}$ $45]_s$ is thinner than the plates in other examples. The slope of the linear trend is greater than the thicker plates; therefore, applied pressure for displacement 50% thickness is much lower. The distribution of the critical regions is similar to the second example and the most critical layer is the bottom layer having 45°. The orientation of the safer regions agree well with the orientation of this ply. In this example, strength ratios

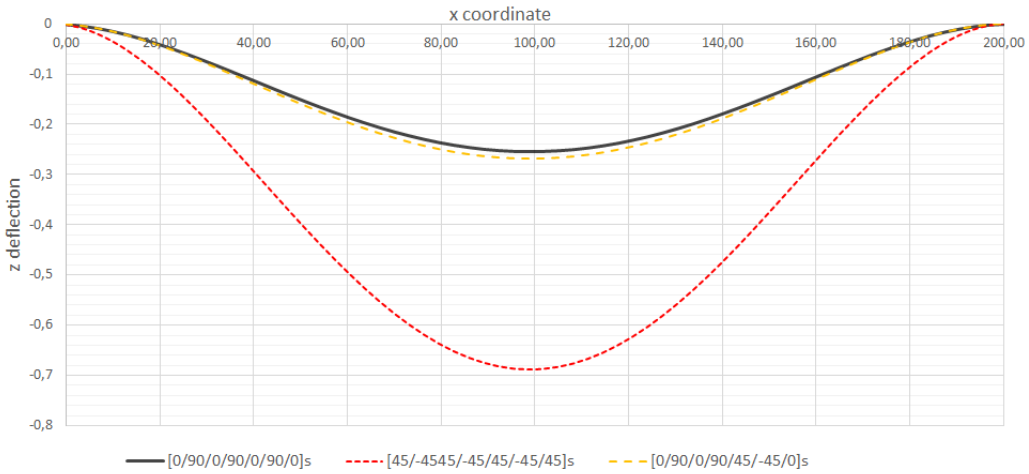

Figure 5.48: Comparison of the displacements of the two-ends clamped rectangular laminae under the same load.

are higher for the pressure to obtain desired displacement. It indicates the greater deviation between linear and nonlinear solutions of the displacements at failure loads.

In example in Section 5.2.2.1, the slope of the linear trend for the one-end clamped plate with orientation $[0/90/0/90/0/90/0]_s$ is much greater than the fully clamped plate with same orientation as expected. As a result, applied load for valid analyses with linear solution is smaller. Nonetheless, linear analyses still gives a first intuition about the distribution of critical regions. The regions near to the clamped end are expected to be failed first and the free and is the least critical since there is no restriction. In addition, having the failure at the boundary changes the behavior of the nonlinear graph as well and percentage difference of the displacements of the linear and nonlinear solutions at failure is smaller.

In example in Section 5.2.2.2, the one-end clamped plate with orientation $[45/\text{-}45/45/\text{-}45/45/\text{-}45/45]_s$ shows different bahavior than the rest of the examples. Only in this example, failure is due to compression of the matrix and maximum displacement calculated by IGA is greater than the calculated displacement by MSC Nastran. This might be due to having the greatest slope of the linear trend among all examples. Although the effect of the fiber orientation can still be observed in the distribution of the critical regions, lower SR values are seen in much larger area than the previous example having cross-ply laminate.

Table 5.19: Summary of numerical examples.

	t [mm]	Exp Disp (%)	Exp Disp [mm]	IGA Disp [mm]	Aplied Pres [MPa]	Exp Failed Layer	Exp Failure Mode	Min SR	Max SR
FC 1	3.5	50	1.75	1.74	0.195	14	TM	T-H Hof Has	MS
FC 2	3.5	50	1.75	1.71	0.182	14	TM	T-H	T-W
FC 3	3.5	50	1.75	1.74	0.195	14	TM	T-H Hof Has	MS
FC 4	2	50	1	1	0.020	8	TM	T-H	T-W
OC 1	3.5	20	0.7	0.62	0.0002	13	TM	T-H Has	T-W
OC 2	3.5	20	0.7	0.71	0.00007	7	CM	T-W	MS
OC 1	3.5	20	0.7	0.65	0.0002	13	TM	T-H Has	T-W
TC 1	3.5	20	0.7	0.7	0.0113	13	TM	T-H Has	MS
TC 2	3.5	20	0.7	0.69	0.004	14	TM	T-H	MS
TC 3	3.5	20	0.7	0.69	0.0106	13	TM	T-H Hof Has	MS

In example in Section 5.2.2.3, the one-end clamped plate with orientation $[0/90/0/90/45/\text{-}45/0]_s$ shows a very similar to the one end cross-ply example. The effect of the $\pm 45^\circ$ plies are again visible in the stress distribution through the thickness graphs.

In example in Section 5.2.3.1, the two-ends clamped plate with orientation $[0/90/0/90/0/90/0]_s$ have strength ratios between the fully clamped and one-end clamped cases. The most critical regions are the clamped boundaries followed by the midsection of the plate. Clamping only in x-direction where 0° plies lie, result in similar pattern of σ_y and τ_{xy} in all two-ends clamped examples.

In example in Section 5.2.3.2, the two-ends clamped plate with orientation $[45/\text{-}45/45/\text{-}45/45/\text{-}45/45]_s$ sustain the least load among at the same displacement among the two-end clamped plated same as the other boundary conditions. The effect of orientation is again visible in the distribution of the critical regions. The clamped boundaries are much more critical in this example than the previous cross-ply laminate.

In example in Section 5.2.3.3, the two-ends clamped plate with orientation $[0/90/0/90/45\ /\text{-}45/0]_s$ has the most critical regions around the clamped boundaries similar to the other examples. $\pm 45^\circ$ plies have dominant σ_y and τ_{xy} whereas, 0/90° plies overpowering σ_x.

CHAPTER 6

CONCLUSION AND FUTURE WORK

In this thesis study, an isogeometric formulation is derived for the analysis of the laminated composite plates. The displacement field is assumed by the first order shear deformation theory. The maximum stress, Tsai-Hill, Hoffman, Tsai-Wu and Hashin criteria are employed to determine the critical regions. To verify the validity of the formulation, results are compared with the exact solution of Pagano [2]. Several numerical examples are performed for laminated composite plates with different shapes, stacking schemes and boundary conditions. Using linear and nonlinear solutions obtained by MSC Nastran, applied loads that can be used for linear analyses are decided by limiting the maximum displacements within a certain percentage of the thickness of the plate. The displacement through the larger span and in-plane stress distributions through the thickness for the elements with maximum stresses are plotted. Moreover, heat-maps are obtained by strength ratios of the Hashin criteria, showing distribution of the critical regions for the most critical layer.

i. It is observed that IGA method is used effectively for analysis of laminated composite plates.

ii. Comparison with the exact solution show that with increasing a/h ratio in-plane stresses and maximum displacement are predicted accurately by IGA with FSDT; whereas the simulation results deviate from the exact solution for transverse shear stresses. It is also observed that increasing the shear correction factor gives better results.

iii. For the fully clamped plates displacements are lower under the same load compared to one-end and two-ends clamped cases. Moreover, laminates with orientation $[45/\text{-}45/\ 45/\text{-}45/45/\text{-}45/45]_s$ displace more than other orientations

used in the examples. Therefore, analyses can be performed for higher loads in linear range for these cases having lower displacements.

iv. From the numerical examples, it can be seen that the relationship between load and the thickness is not linear. Reducing the thickness 45% results in 5 times increase of the maximum displacement for the fully clamped plate with the same dimensions.

v. Boundary conditions effect the failure loads drastically. Clamping one more end of one-end clamped case decrease the displacements and increase the applicable load leading the same displacement more than 50 times for two-ends clamped case.

vi. Laminates with all $\pm 45^{\circ}$ plies are exposed to the most displacement under the same load for all boundary conditions.

vii. As it can be seen from the results, Tsai-Hill criterion gives the minimum strength ratio for almost all examples. In other words, the theory expects failure at least loads. Therefore, it can be said that it is the most conservative theory.

viii. In all the examples failure is due to matrix failures; moreover, almost in all of them failure mode is tensile failure of matrix. Thus, it can be concluded that for the composite plates under transverse pressure, matrix failures are more critical than the fiber failures.

To conclude, the isogeometric analysis method is a very promising method having many benefits due to representing the geometry exactly and the use of spline based functions. As future work, more complex geometries can be investigated. The studies can be extend for large deformations and for nonlinear solutions of the problems. In addition, more complex analysis like delamination can be examined. By adding iterative procedure involving elimination or reduction of stiffness terms for the failed elements together with nonlinear solutions, progressive failure analysis can be conducted.

REFERENCES

[1] J. A. Cottrell, T. J. Hughes, and Y. Bazilevs, *Isogeometric analysis: toward integration of CAD and FEA*. John Wiley & Sons, 2009.

[2] N. Pagano and S. J. Hatfield, "Elastic behavior of multilayered bidirectional composites," in *Mechanics of Composite Materials*. Springer, 1994, pp. 124–127.

[3] F. C. Campbell, *Structural composite materials*. ASM international, 2010.

[4] R. M. Jones, *Mechanics of composite materials*. CRC press, 2014.

[5] L. Piegl and W. Tiller, *The NURBS Book*, 2nd ed. New York, NY, USA: Springer-Verlag, 1997.

[6] R.-J. Yan, J. Wu, J. Y. Lee, and C.-S. Han, "Representation of 3d environment map using b-spline surface with two mutually perpendicular lrfs," *Mathematical Problems in Engineering*, vol. 2015, 2015.

[7] T. J. Hughes, J. A. Cottrell, and Y. Bazilevs, "Isogeometric analysis: Cad, finite elements, nurbs, exact geometry and mesh refinement," *Computer methods in applied mechanics and engineering*, vol. 194, no. 39-41, pp. 4135–4195, 2005.

[8] V. P. Nguyen, C. Anitescu, S. P. Bordas, and T. Rabczuk, "Isogeometric analysis: an overview and computer implementation aspects," *Mathematics and Computers in Simulation*, vol. 117, pp. 89–116, 2015.

[9] J. N. Reddy, *Mechanics of laminated composite plates and shells: theory and analysis*. CRC press, 2003.

[10] A. K. Kaw, *Mechanics of composite materials*. CRC press, 2005.

[11] L. V. Tran, A. Ferreira, and H. Nguyen-Xuan, "Isogeometric analysis of functionally graded plates using higher-order shear deformation theory," *Composites Part B: Engineering*, vol. 51, pp. 368–383, 2013.

[12] G. Farin, “A history of curves and surfaces,” *Handbook of computer aided geometric design*, vol. 1, 2002.

[13] D. Weisberg, “The engineering design revolution cad history,” 2008.

[14] P. Bézier, “Procédé de définition numérique des courbes et surfaces non mathématiques,” *Automatisme*, vol. 13, no. 5, pp. 189–196, 1968.

[15] R. F. Riesenfeld, “Applications of b-spline approximation to geometric problems of computer-aided design,” Ph.D. dissertation, Syracuse University Syracuse, NY, 1973.

[16] N. Pagano, “Exact solutions for composite laminates in cylindrical bending,” *Journal of composite materials*, vol. 3, no. 3, pp. 398–411, 1969.

[17] N. J. Pagano, “Exact solutions for rectangular bidirectional composites and sandwich plates,” *Journal of composite materials*, vol. 4, no. 1, pp. 20–34, 1970.

[18] J. Reddy and D. Robbins, “Theories and computational models for composite laminates,” *Applied mechanics reviews*, vol. 47, no. 6, pp. 147–169, 1994.

[19] G. Castellazzi, P. Krysl, and I. Bartoli, “A displacement-based finite element formulation for the analysis of laminated composite plates,” *Composite Structures*, vol. 95, pp. 518–527, 2013.

[20] W. Yu, “Mathematical construction of a reissner–mindlin plate theory for composite laminates,” *International journal of solids and structures*, vol. 42, no. 26, pp. 6680–6699, 2005.

[21] B. Adim, T. H. Daouadji, and A. Rabahi, “A simple higher order shear deformation theory for mechanical behavior of laminated composite plates,” *International Journal of Advanced Structural Engineering (IJASE)*, vol. 8, no. 2, pp. 103–117, 2016.

[22] C. de Falco, A. Reali, and R. Vázquez, “Geopdes: a research tool for isogeometric analysis of pdes,” *Advances in Engineering Software*, vol. 42, no. 12, pp. 1020–1034, 2011.

[23] B. Marussig, “Isogeometric analysis with trimmed cad models,” *PAMM*, vol. 18, no. 1, p. e201800184, 2018.

[24] Y. Bazilevs, C. Michler, V. Calo, and T. Hughes, "Isogeometric variational multiscale modeling of wall-bounded turbulent flows with weakly enforced boundary conditions on unstretched meshes," *Computer Methods in Applied Mechanics and Engineering*, vol. 199, no. 13-16, pp. 780–790, 2010.

[25] L. B. da Veiga, A. Buffa, D. Cho, and G. Sangalli, "Isogeometric analysis using t-splines on two-patch geometries," *Computer methods in applied mechanics and engineering*, vol. 200, no. 21-22, pp. 1787–1803, 2011.

[26] D. Schillinger, L. Dede, M. A. Scott, J. A. Evans, M. J. Borden, E. Rank, and T. J. Hughes, "An isogeometric design-through-analysis methodology based on adaptive hierarchical refinement of nurbs, immersed boundary methods, and t-spline cad surfaces," *Computer Methods in Applied Mechanics and Engineering*, vol. 249, pp. 116–150, 2012.

[27] N. Nguyen-Thanh, J. Kiendl, H. Nguyen-Xuan, R. Wüchner, K.-U. Bletzinger, Y. Bazilevs, and T. Rabczuk, "Rotation free isogeometric thin shell analysis using pht-splines," *Computer Methods in Applied Mechanics and Engineering*, vol. 200, no. 47-48, pp. 3410–3424, 2011.

[28] N. Nguyen-Thanh, J. Muthu, X. Zhuang, and T. Rabczuk, "An adaptive three-dimensional rht-splines formulation in linear elasto-statics and elasto-dynamics," *Computational Mechanics*, vol. 53, no. 2, pp. 369–385, 2014.

[29] F. Auricchio, L. B. da Veiga, A. Buffa, C. Lovadina, A. Reali, and G. Sangalli, "A fully "locking-free" isogeometric approach for plane linear elasticity problems: A stream function formulation," *Computer methods in applied mechanics and engineering*, vol. 197, no. 1-4, pp. 160–172, 2007.

[30] F. Auricchio, L. B. Da Veiga, C. Lovadina, and A. Reali, "The importance of the exact satisfaction of the incompressibility constraint in nonlinear elasticity: mixed fems versus nurbs-based approximations," *Computer Methods in Applied Mechanics and Engineering*, vol. 199, no. 5-8, pp. 314–323, 2010.

[31] D. Benson, Y. Bazilevs, M.-C. Hsu, and T. Hughes, "A large deformation, rotation-free, isogeometric shell," *Computer Methods in Applied Mechanics and Engineering*, vol. 200, no. 13-16, pp. 1367–1378, 2011.

[32] J. Kiendl, K.-U. Bletzinger, J. Linhard, and R. Wüchner, "Isogeometric shell analysis with kirchhoff–love elements," *Computer Methods in Applied Mechanics and Engineering*, vol. 198, no. 49-52, pp. 3902–3914, 2009.

[33] L. Espath, A. Braun, A. Awruch, and S. Maghous, "Nurbs-based three-dimensional analysis of geometrically nonlinear elastic structures," *European Journal of Mechanics-A/Solids*, vol. 47, pp. 373–390, 2014.

[34] Y. Bazilevs and I. Akkerman, "Large eddy simulation of turbulent taylor–couette flow using isogeometric analysis and the residual-based variational multiscale method," *Journal of Computational Physics*, vol. 229, no. 9, pp. 3402–3414, 2010.

[35] A. Buffa, G. Sangalli, and R. Vázquez, "Isogeometric analysis in electromagnetics: B-splines approximation," *Computer Methods in Applied Mechanics and Engineering*, vol. 199, no. 17-20, pp. 1143–1152, 2010.

[36] I. Temizer, P. Wriggers, and T. Hughes, "Three-dimensional mortar-based frictional contact treatment in isogeometric analysis with nurbs," *Computer Methods in Applied Mechanics and Engineering*, vol. 209, pp. 115–128, 2012.

[37] G. Zhang, R. Alberdi, and K. Khandelwal, "Analysis of three-dimensional curved beams using isogeometric approach," *Engineering Structures*, vol. 117, pp. 560–574, 2016.

[38] I. N. Tsiptsis and E. J. Sapountzakis, "Generalized warping and distortional analysis of curved beams with isogeometric methods," *Computers & Structures*, vol. 191, pp. 33–50, 2017.

[39] G. Radenković and A. Borković, "Linear static isogeometric analysis of an arbitrarily curved spatial bernoulli–euler beam," *Computer Methods in Applied Mechanics and Engineering*, vol. 341, pp. 360–396, 2018.

[40] K. A. Hasim, "Isogeometric static analysis of laminated composite plane beams by using refined zigzag theory," *Composite Structures*, vol. 186, pp. 365–374, 2018.

[41] S. Faroughi, E. Shafei, and A. Eriksson, "Nurbs-based modeling of laminated composite beams with isogeometric displacement-only theory," *Composites Part B: Engineering*, vol. 162, pp. 89–102, 2019.

[42] K. Fan, J. Zeng, Z. Huang, and Q. Liu, "Tensor-decomposition based matrix computation: A fast method for the isogeometric fsdt analysis of laminated composite plate," *Thin-Walled Structures*, vol. 144, p. 106326, 2019.

[43] C. H. Thai, H. Nguyen-Xuan, N. Nguyen-Thanh, T.-H. Le, T. Nguyen-Thoi, and T. Rabczuk, "Static, free vibration, and buckling analysis of laminated composite reissner–mindlin plates using nurbs-based isogeometric approach," *International Journal for Numerical Methods in Engineering*, vol. 91, no. 6, pp. 571–603, 2012.

[44] M. Lyly, R. Stenberg, and T. Vihinen, "A stable bilinear element for the reissner-mindlin plate model," *Computer Methods in Applied Mechanics and Engineering*, vol. 110, no. 3-4, pp. 343–357, 1993.

[45] C. H. Thai, H. Nguyen-Xuan, S. P. A. Bordas, N. Nguyen-Thanh, and T. Rabczuk, "Isogeometric analysis of laminated composite plates using the higher-order shear deformation theory," *Mechanics of Advanced Materials and Structures*, vol. 22, no. 6, pp. 451–469, 2015.

[46] C. H. Thai, A. Ferreira, S. P. A. Bordas, T. Rabczuk, and H. Nguyen-Xuan, "Isogeometric analysis of laminated composite and sandwich plates using a new inverse trigonometric shear deformation theory," *European Journal of Mechanics-A/Solids*, vol. 43, pp. 89–108, 2014.

[47] H. Nguyen-Xuan, C. H. Thai, and T. Nguyen-Thoi, "Isogeometric finite element analysis of composite sandwich plates using a higher order shear deformation theory," *Composites Part B: Engineering*, vol. 55, pp. 558–574, 2013.

[48] C. H. Thai, A. Ferreira, E. Carrera, and H. Nguyen-Xuan, "Isogeometric analysis of laminated composite and sandwich plates using a layerwise deformation theory," *Composite Structures*, vol. 104, pp. 196–214, 2013.

[49] X. Li, J. Zhang, and Y. Zheng, "Static and free vibration analysis of laminated composite plates using isogeometric approach based on the third order shear

deformation theory," *Advances in Mechanical Engineering*, vol. 6, p. 232019, 2014.

[50] A. Gupta and A. Ghosh, "Bending analysis of laminated and sandwich composite reissner-mindlin plates using nurbs-based isogeometric approach," *Procedia engineering*, vol. 173, pp. 1334–1341, 2017.

[51] L. V. Tran, J. Lee, H. Nguyen-Van, H. Nguyen-Xuan, and M. A. Wahab, "Geometrically nonlinear isogeometric analysis of laminated composite plates based on higher-order shear deformation theory," *International Journal of Non-Linear Mechanics*, vol. 72, pp. 42–52, 2015.

[52] H. Kapoor and R. Kapania, "Geometrically nonlinear nurbs isogeometric finite element analysis of laminated composite plates," *Composite Structures*, vol. 94, no. 12, pp. 3434–3447, 2012.

[53] T. Le-Manh, T. Luu-Anh, and J. Lee, "Isogeometric analysis for flexural behavior of composite plates considering large deformation with small rotations," *Mechanics of Advanced Materials and Structures*, vol. 23, no. 3, pp. 328–336, 2016.

[54] V. P. Nguyen, P. Kerfriden, and S. P. Bordas, "Two-and three-dimensional isogeometric cohesive elements for composite delamination analysis," *Composites Part B: Engineering*, vol. 60, pp. 193–212, 2014.

[55] H. Kapoor, R. K. Kapania, and S. R. Soni, "Interlaminar stress calculation in composite and sandwich plates in nurbs isogeometric finite element analysis," *Composite Structures*, vol. 106, pp. 537–548, 2013.

[56] F. Auricchio, F. Calabro, T. J. Hughes, A. Reali, and G. Sangalli, "A simple algorithm for obtaining nearly optimal quadrature rules for nurbs-based isogeometric analysis," *Computer Methods in Applied Mechanics and Engineering*, vol. 249, pp. 15–27, 2012.

[57] G. Pavan and K. N. Rao, "Bending analysis of laminated composite plates using isogeometric collocation method," *Composite Structures*, vol. 176, pp. 715–728, 2017.

[58] J. N. Reddy, "A simple higher-order theory for laminated composite plates," *Journal of applied mechanics*, vol. 51, no. 4, pp. 745–752, 1984.

[59] C. Nwoji, H. Onah, B. Mama, and C. Ike, "Theory of elasticity formulation of mindlin plate equations," *International Journal of Engineering and Technology*, vol. 9, no. 6, pp. 4344–4352, 2017.

[60] J. Whitney and N. Pagano, "Shear deformation in heterogeneous anisotropic plates," 1970.

[61] P. Madabhusi-Raman and J. F. Davalos, "Static shear correction factor for laminated rectangular beams," *Composites Part B: Engineering*, vol. 27, no. 3-4, pp. 285–293, 1996.

[62] T. J. Hughes, R. L. Taylor, and W. Kanoknukulchai, "A simple and efficient finite element for plate bending," *International Journal for Numerical Methods in Engineering*, vol. 11, no. 10, pp. 1529–1543, 1977.

[63] O. Zienkiewicz, R. Taylor, and J. Too, "Reduced integration technique in general analysis of plates and shells," *International Journal for Numerical Methods in Engineering*, vol. 3, no. 2, pp. 275–290, 1971.

[64] N. Grover, D. K. Maiti, and B. N. Singh, "Flexural behavior of general laminated composite and sandwich plates using a secant function based shear deformation theory," *Latin American Journal of Solids and Structures*, vol. 11, no. 7, pp. 1275–1297, 2014.

[65] M. Slimane, "Study and comparison of different plate theory," *International Journal of Engineering Research And Advanced Technology (IJERAT)*, vol. 3, no. 8, pp. 49–59, 2017.

[66] R. Rolfes and K. Rohwer, "Improved transverse shear stresses in composite finite elements based on first order shear deformation theory," *International Journal for Numerical Methods in Engineering*, vol. 40, no. 1, pp. 51–60, 1997.

[67] N. Germain, J. Besson, and F. Feyel, "Simulation of laminate composites degradation using mesoscopic non-local damage model and non-local layered shell element," *Modelling and Simulation in Materials Science and Engineering*, vol. 15, no. 4, p. S425, 2007.

[68] P. Pal and S. Bhattacharyya, "Progressive failure analysis of cross-ply laminated composite plates by finite element method," *Journal of reinforced plastics and composites*, vol. 26, no. 5, pp. 465–477, 2007.

[69] R. Hill, "The mathematical theory of plasticity, clarendon," *Oxford*, vol. 613, p. 614, 1950.

[70] S. W. Tsai, "Strength theories of filamentary structure," *Fundamental aspects of fiber reinforced plastic composites*, 1968.

[71] O. Hoffman, "The brittle strength of orthotropic materials," *Journal of Composite Materials*, vol. 1, no. 2, pp. 200–206, 1967.

[72] R. B. Pipes and B. Cole, "On the off-axis strength test for anisotropic materials1," *Journal of Composite Materials*, vol. 7, no. 2, pp. 246–256, 1973.

[73] S. W. Tsai and E. M. Wu, "A general theory of strength for anisotropic materials," *Journal of composite materials*, vol. 5, no. 1, pp. 58–80, 1971.

[74] H. T. Hahn and S. W. Tsai, *Introduction to composite materials*. CRC Press, 1980.

[75] G. N. Naik and A. K. Murty, "A failure mechanism-based approach for design of composite laminates," *Composite structures*, vol. 45, no. 1, pp. 71–80, 1999.

[76] Z. Hashin, "Failure criteria for unidirectional fiber composites," *Journal of applied mechanics*, vol. 47, no. 2, pp. 329–334, 1980.

[77] M. G. Cox, "The numerical evaluation of b-splines," *IMA Journal of Applied Mathematics*, vol. 10, no. 2, pp. 134–149, 1972.

[78] C. De Boor, "On calculating with b-splines," *Journal of Approximation theory*, vol. 6, no. 1, pp. 50–62, 1972.